SPECTRAL MEASUREMENTS OF THE SUNYAEV-ZEL'DOVICH EFFECT

A DISSERTATION
SUBMITTED TO THE DEPARTMENT OF PHYSICS
AND THE COMMITTEE ON GRADUATE STUDIES
OF STANFORD UNIVERSITY
IN PARTIAL FULFILLMENT OF THE REQUIREMENTS
FOR THE DEGREE OF
DOCTOR OF PHILOSOPHY

Bradford Adam Benson
July 2004

I certify that I have read this dissertation and that, in my opinion, it is fully adequate in scope and quality as a dissertation for the degree of Doctor of Philosophy.

Sarah Church
(Principal Adviser)

I certify that I have read this dissertation and that, in my opinion, it is fully adequate in scope and quality as a dissertation for the degree of Doctor of Philosophy.

Robert Wagoner

I certify that I have read this dissertation and that, in my opinion, it is fully adequate in scope and quality as a dissertation for the degree of Doctor of Philosophy.

Steve Kahn

Approved for the University Committee on Graduate Studies.

Abstract

This thesis describes spectral measurements of the Sunyaev-Zel'dovich (SZ) effect from clusters of galaxies using the Sunyaev-Zel'dovich Infrared Experiment (SuZIE II). SuZIE II is a 12 element 300 mK bolometer array which observes in three frequency bands between 150 and 350 GHz. Simultaneous multi-frequency measurements have been used to distinguish between thermal and kinematic components of the SZ effect, and to significantly reduce the effects of variations in atmospheric emission which can otherwise dominate the noise. We report significant detections of the SZ effect in 15 clusters of galaxies.

For a sub-sample of these clusters we have set limits to their peculiar velocities with respect to the Hubble flow, and have used the cluster sample to set a 95% confidence limit of $< 1260\,\mathrm{km\,s^{-1}}$ to the bulk flow of the intermediate-redshift universe in the direction of the CMB dipole. This is the first time that SZ measurements have been used to constrain bulk flows. We show that systematic uncertainties in peculiar velocity determinations from the SZ effect are likely to be dominated by sub-millimeter point sources and we discuss the level of this contamination.

We also calculate the central Comptonization, y_0, the integrated SZ flux decrement, S, and the gas mass, $M_{\rm gas}$, of each cluster. We find that the calculated central Comptonization is much more sensitive to the assumed spatial model for the intra-cluster gas than either the calculated integrated SZ flux or the gas mass. Comparing our central Comptonization results with values calculated from measurements using the BIMA and OVRO interferometers yields significantly discrepant results. On average, the SuZIE calculated central Comptonizations are $\sim 60\%$ higher in the cooling flow clusters than the interferometric values, compared to only $\sim 12\%$ higher in the

non-cooling flow clusters. We believe this discrepancy to be in large part due to the spatial modelling of the intra-cluster gas which is typically derived from X-ray observations.

We use our entire cluster sample to construct y_0–T, S–T, and $M_{\rm gas}$–T scaling relations, where T is the X-ray temperature of the intra-cluster (IC) gas. The y_0–T scaling relation is inconsistent with what we would expect for self-similar clusters; however this result is questionable because of the large systematic uncertainty in y_0. In general, this relation is difficult to measure because it relies more sensitively on the spatial modelling of the IC gas. The S–T scaling relation has a slope and redshift evolution consistent with what we expect for self-similar clusters with a characteristic density that scales with the mean density of the universe. We rule out zero redshift evolution of the S–T relation at $\sim$ 90% confidence. The $M_{\rm gas}$–T scaling relation is consistent with the expected self-similar relation and the corresponding relation calculated from X-ray observations. This marks the first time that the S–T and $M_{\rm gas}$–T scaling relations have been derived from SZ observations.

Acknowledgements

There are many people to thank who made this thesis possible. Of course it starts with my advisor Sarah Church, who gave me an opportunity to work on this project and always had sympathy for the plight of the graduate student, which made my time in graduate school far less stressful than it should have been. I would like to thank Brian Keating for convincing Sarah to hire me, and fulfilling the promise he made to me in my first year of graduate school of offering me a post-doc when I graduated. Jamie Hinderks and I were Sarah's only two graduate students during our time at Stanford, he is really a wizard in lab who loves building things, I learned so much from him. Keith Thompson was a jack-of-all-trades who kept the night shift going on many an observing run. Byron Philhour was literally "the man". He is one of the most likeable people I have ever met and is the embodiment of all that is good in this world. He taught me how to drive a stick shift, and was always there for me when I needed him most. Ben Rusholme, thank you for introducing me to AsiaSF, convincing Jamie and I to go to Kauai, and for being such a positive force in lab.

I have to thank all the people that came before me on SuZIE and who built many of the components which I relied on. It is impossible for me to know or comprehend all the work that was done before me, but I am sure that Phil Mauskopf, Marcus Runyan, Byron Philhour, and Bill Holzapfel did their fair share to make the SuZIE receiver what it is today.

I have to thank the string of undergraduates who made their way through Sarah's lab, and made work so much more enjoyable. Starting with the original, Seebany Datta-Barua, who amazingly could sleep on the very hard floors in our office. Judy Lau made summers at Stanford so much more fun. I have so many great memories of time spent with her, from Yosemite, to miniature golf, to the nickel arcade, she always had the right idea for fun. I tried not to hold her smelly hands against her. Evan Kirby always put up with my older-brother-like teasing of him. Alison Brizius was a great source of undergraduate goings-on, and has always remained an amazingly well-balanced individual. Cara Henson was not quite an undergraduate, but she turned into a pretty good friend who introduced me to countless bands and has been a trusted confidant. There is also the army of undergraduates who Sarah employed, Kroodsma, Elizabeth, Sim, Justin, and Tess, who I never got to work as closely with, but was very glad to get to know.

I had so much fun during my time in Hawaii, it was such a great opportunity to go on six different observing runs with SuZIE. Contrasting how miserable I was during my first observing run, with how nostalgic I feel about it now really highlights the extremes which are possible trying to get an instrument to work on an isolated mountain top while oxygen deprived. The Caltech Sub-millimeter Observatory is such a unique operation and I am thankful to the people behind it who allowed me to control a 10 meter world-class telescope unsupervised. The CSO telescope staff, Pat, Allen, Ed, and Steve, were always very helpful and fun to be around, which is not surprising considering their overwhelmingly Midwestern heritage. The Big Island itself is such an amazing island, and I am fortunate to have spent so much time there exploring it with so many different people. I have tried to pass on the SuZIE-Hawaii experience to as many people as possible, and have so many great memories of trolling around the island, from the Green Sand Beach, to the musical stylings of Bosco, to Pololu Valley, to the Aloha Cafe, to the hike to the Pu'uO'o vent. I will always consider the Big Island the ultimate vacation spot.

There is also the host of other Stanford people that I have met and become friends with during my time here. They are too numerous to mention in full, but have made my time here so much more memorable. The AMO crowd: Adam, Igor, Hilton, Nate, and Edina. Other Astro folk: Phil, Paul, DSE, and Tim. Fellow Grad Students: Tj, Altman, Lindsay, the true founder of physics beer, Libby and Tim, Moon, Paul S., Burney, Jon, Anne, Joon, Chad, Alex, Jason, and Sam. Block Lab: Kristina, Ravi, Elio, and Josh. I apologize to those that I forgot to mention. Thank you all.

These acknowledgements are already too long, but I have to thank my family for always being there for me during this long time in graduate school. My Dad has provided a great vacation spot for me in Wisconsin, all the while taking great care of my cat, Pookie. My Brother was kind enough to follow me out to the West Coast three years ago, and has always welcomed me to visit him in Portland. My Aunt Barbara and Uncle Richard have both done a great job following up on me these last few years, I am very thankful for their support. And of course I have to thank my Mom. She was always in my thoughts throughout graduate school. It made me so very happy to know how tremendously proud she was of me, and this has always been a great source of strength for me. Thank you.

Contents

List of Tables

List of Figures

Chapter 1

Introduction

The subject of cosmology seeks to explain and understand the structure, evolution, and origin of the Universe. Arguably, the three pillars of evidence supporting our theories of modern cosmology are:

1. The discovery of Hubble's law in 1929 [54].

2. The light element abundances predicted by Big Bang Nucleosynthesis (BBN) [107].

3. The discovery of the Cosmic Microwave Background (CMB) by Penzias and Wilson in 1965 [81].

The CMB is unique amongst the three because it is not only a prediction but a real tangible entity which interacts with other matter in the Universe. So while the mere existence of the CMB is considered to be a fundamental piece of evidence supporting our theories of modern cosmology, the unique properties of the CMB have allowed it to be an important cosmological probe in its own right.

The CMB was originally predicted in 1946 by Gamow [40] as a consequence of the Hot Big Bang model. This model assumes that the Universe began in a hot dense state and then underwent a period of expansion. As the Universe expanded the matter within it cooled. When the Universe reached a temperature of $\sim$3500 K neutral Hydrogen began to form in significant proportions. This caused the Universe to transition from being an ionized optically thick plasma, where matter and radiation were in thermal equilibrium, to a state where matter and light decoupled and the Universe became optically thin. The left-over radiation from the earlier time would then be free to travel the Universe unfettered and should still be visible today. Because the Universe continued to expand after the decoupling, the left-over light would be redshifted to a temperature cooler than its thermodynamic temperature at de-coupling. In 1948 Alpher, Bethe, and Gamow [4] predicted the radiation field would have a characteristic temperature of $\sim$5 K.

Seventeen years later in 1965 an isotropic radiation field with a characteristic temperature of $T \sim 3.5$ K was discovered by Penzias and Wilson. Later that year, Dicke, Peebles, Roll, and Wilkinson [28] suggested that this radiation field was in fact the CMB predicted from the Hot Big Bang model. Since that time, the CMB has been measured with much greater sensitivity than the measurements of Penzias and Wilson over a range of frequencies and spatial scales. Currently, it is well-accepted that the CMB is in fact the left-over radiation field predicted from the Hot Big Bang model.

We now know much more about the CMB, particularly from two all-sky maps made by the COBE and WMAP satellites [7, 8]. The CMB is the most perfect black-body known of in the Universe, with a characteristic temperature of T=2.728$\pm$0.004 K [39]. If we consider the CMB's temperature pattern on the sky, the most significant spatial feature is a dipole moment of 3.346$\pm$0.017 mK [8] which is due to our relative motion with respect to the CMB rest frame. However, not including the CMB dipole, the COBE and WMAP maps are uniform at a level of $\Delta T/T < 10^{-5}$. This suggests that the CMB is remarkably uniform and isotropic. This property makes the CMB an ideal back-light for the rest of the observable Universe. By searching for spectral distortions in the CMB we can probe the intervening matter between us and the time of de-coupling 14 billion light years away.

1.1 The Sunyaev-Zel'dovich Effect

The spectral distortion to the Cosmic Microwave Background radiation (CMB) caused by the Compton scattering of CMB photons by the hot gas in the potential wells of galaxy clusters, known as the Sunyaev-Zel'dovich (SZ) effect, is now relatively straightforward to detect and has now been measured in more than 50 sources [see 13, for a review]. Single-frequency observations of the SZ effect can be used to determine the Hubble constant [76, 51, 84, 87, 85, 58, 27, 88] and to measure the baryon fraction in clusters [76, 46].

The spectrum of the SZ effect is also an important source of information. It can be approximated by the sum of two components (see Figure 1.1) with the strongest being the thermal SZ effect that is caused by the random thermal motions of the scattering electrons [102]. The kinematic SZ effect, due to the peculiar velocity of the intracluster (IC) gas with respect to the CMB rest frame [103], is expected to be much weaker if peculiar velocities are less than $1000\,\mathrm{km\,s^{-1}}$, as favored by current models [45, 96, 101]. The thermal SZ effect has a distinct spectral signature, appearing as a decrement in the intensity of the CMB below a frequency of $\sim$ 217 GHz, and an increment at higher frequencies (the exact frequency at which the thermal effect is zero depends on the temperature of the IC gas, as discussed by Rephaeli [91]). The kinematic effect appears as a decrement at all frequencies for a cluster that is receding with respect to the Hubble flow, and an increment at all frequencies for a cluster that is approaching. Measurements that span the null of the thermal effect are able to separate the two effects, allowing the determination of the cluster peculiar velocity [52, 71, 63]. Additionally, SZ spectral measurements can, in principle, be used to determine the cluster gas temperature independently of X-ray measurements [83, 49], the CMB temperature as a function of redshift [90, 6] and also to search for populations of non-thermal electrons [97].

1.2 Applications of the SZ Effect to Cosmology

1.2.1 Cluster Peculiar Velocities

Peculiar velocities probe large-scale density fluctuations and allow the distribution of matter to be determined directly without assumptions about the relationship between light and mass. Measurements of a large sample of peculiar velocities can be used to

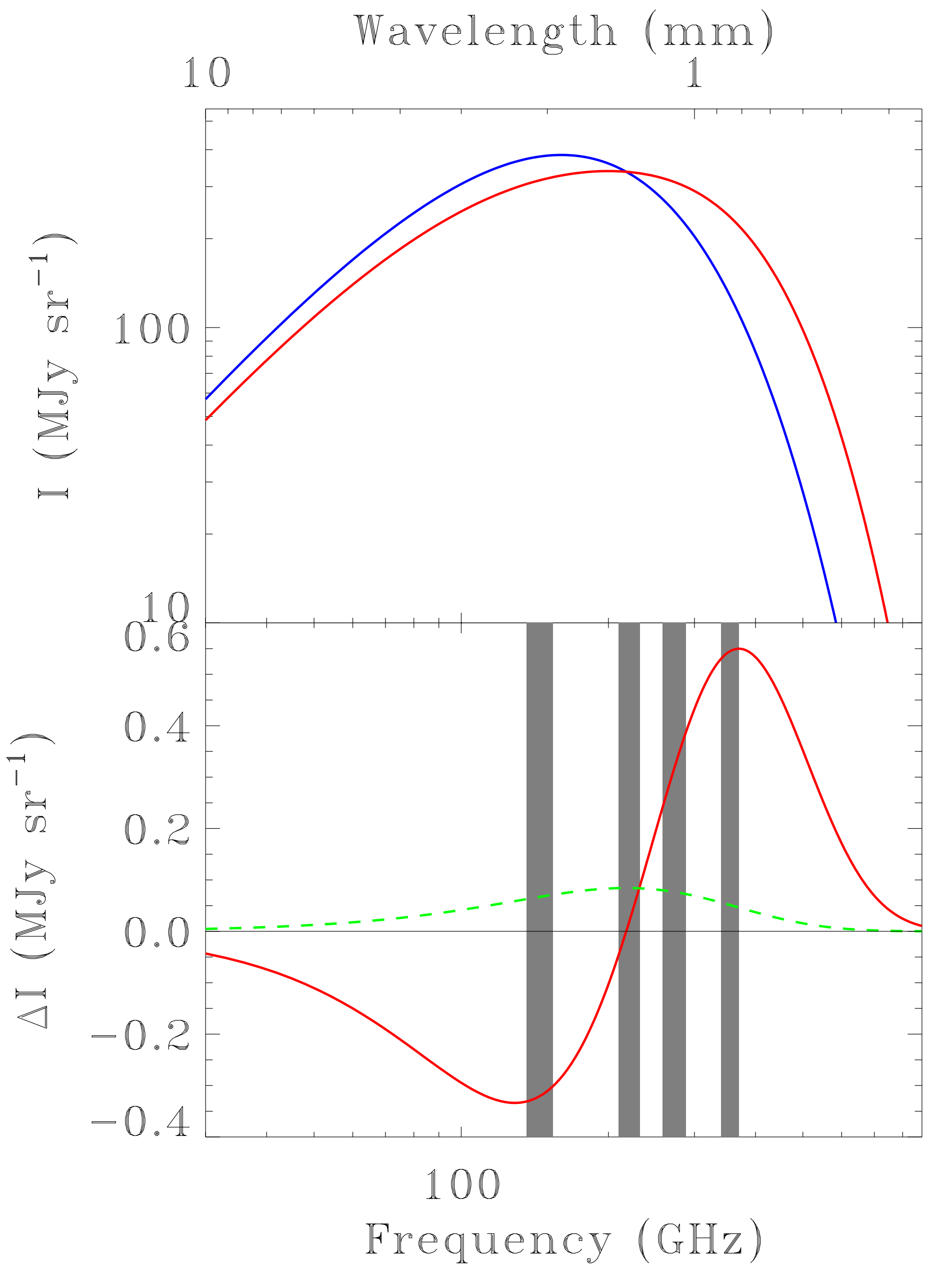

Fig. 1.1.— (Top) The CMB spectrum before (blue) and after (red) looking towards a cluster with a central Comptonization of 600×10^{-4}. (Bottom) The difference spectrum of the Sunyaev-Zel'dovich effect towards a cluster with a more typical central Comptonization of 3×10^{-4} and a peculiar velocity of 1000 km s^{-1}. The red curve is the SZ thermal effect, and the dashed green curve is the SZ kinematic effect. The shaded regions indicate the frequency bands in which SuZIE II observes.

probe Ω_m independently of the properties of dark energy [80], and can, in principle, be used to reconstruct modes of the gravitational potential [31]. The local ($z \lesssim 0.05$) peculiar velocity field has already been measured and has been used to place tight constraints on Ω_m [11, 22, 21, 12]. However, the techniques used at low redshift cannot be easily extended to higher redshifts. These techniques usually determine radial peculiar velocities by taking the difference of the velocity implied by the redshift of the cluster with the expected Hubble flow at that distance. The distance measurements are usually determined using standard candles, which, in general, have measurement errors that increase linearly with distance. SZ spectral measurements allow peculiar velocities to be determined completely independent of the extragalactic distance ladder.

1.2.2 SZ Cluster Surveys

Clusters of galaxies are the largest gravitationally bound objects in the Universe, and formed at relatively early times over a critical redshift range ($0 < z \lesssim 3$) during which the dark energy came to dominate the total energy density of the Universe. A measurement of the evolution of the cluster number density with redshift is sensitive to various cosmological parameters, including σ_8, Ω_M, Ω_Λ, and the dark energy equation of state [108, 50]. A direct measurement of the cluster number density can be made through a survey utilizing the Sunyaev-Zel'dovich (SZ) effect. The SZ effect is particularly well-suited for cluster surveys because an SZ survey will detect every cluster above a mass limit that is independent of redshift [see 13, for example]. Active and planned SZ surveys should result in the discovery of tens of thousands of clusters over the next several years, [see 95, for a review].

The cosmological constraints from any SZ survey may ultimately be limited by how closely clusters behave as standard candles. Haiman et al. [48] showed that future SZ surveys are likely to be limited by systematic uncertainties due to the assumption that clusters are virialized objects whose density scales with the mean background density. Observations of relatively nearby clusters ($z \lesssim 0.1$) in X-rays have shown that clusters are at least remarkably regular objects whose observable properties seem to obey well-behaved scaling relations. These include the mass-temperature [e.g., 38], size-temperature [e.g., 75], and luminosity-temperature [e.g., 67] scaling relations. Verde et al. [104] have argued that an integrated SZ flux versus X-ray temperature scaling relation should have an exceptionally small scatter, compared to other cluster scaling relations, and should be especially useful in testing possible deviations from virialization.

Investigations of SZ scaling relations have been limited so far due to a scarcity of measurements. Cooray [20] and McCarthy et al. [74] have compiled SZ measurements drawn from the literature and constructed SZ scaling relations; however these studies suffered from several drawbacks. Firstly, both papers drew upon measurements from several different instruments. While no systematic differences across instruments were known of at the time, this thesis offers the first evidence that a significant systematic discrepancy does exist. Secondly, both papers concentrated on scaling relations that use the central decrement of the cluster. The calculated central decrement often relies on an assumed spatial distribution of the intra-cluster (IC) gas, whose density is still best constrained by higher resolution X-ray data. The traditional parameterization of the IC gas distribution with the single Beta model [14, 15] causes a large systematic uncertainty in the central decrement calculated from SZ measurements. This thesis addresses both these issues by constructing scaling relations using SZ measurements from only one instrument, and instead focusing on the integrated SZ flux scaling relation.

Chapter 2

The Sunyaev-Zel'dovich Effect

2.1 The Thermal Effect

We express the CMB intensity difference caused by a distribution of high energy electrons, n_e, along the line of sight as [91]:

$$\Delta I_T = I_0 \frac{x^3}{e^x - 1}[\Phi(x, T_e) - 1]\tau \tag{2.1}$$

where $x = h\nu/kT_0$, $I_0 = 2(kT_0)^3/(hc)^2$, T_0 is the temperature of the CMB, $\tau = \int n_e \sigma_T dl$ is the optical depth of the cluster to Thomson scattering, and $\Phi(x, T_e)$ is an integral over electron velocities and scattering directions that is specified in [91], calculated assuming $\tau \ll 1$. In the limit of non-relativistic electrons, this reduces to the familiar non-relativistic form for the thermal SZ effect:

$$[\Phi(x, T_e) - 1] = \frac{xe^x}{e^x - 1}\left[x\frac{e^x + 1}{e^x - 1} - 4\right]\frac{kT_e}{m_e c^2} \tag{2.2}$$

Following [52], we define:

$$\Psi(x, T_e) = \frac{x^3}{e^x - 1}[\Phi(x, T_e) - 1] \tag{2.3}$$

There also exist other analytic and numerical expressions for equation (2.1) [see 16, 57, 29] based on a relativistic extension of the Kompaneets equation [60]. These expressions are in excellent agreement with equation (2.1).

We define Comptonization as $y = \tau \times (kT_e/m_e c^2)$. It is a useful quantity because it represents a frequency independent measure of the magnitude of the SZ effect in a cluster that, unlike ΔI_T, allows direct comparisons with other experiments.

2.2 Kinematic SZ Effect

The change in intensity of the CMB due to the non-relativistic kinematic SZ effect is:

$$\Delta I_K = -I_0 \times \frac{x^4 e^x}{(e^x - 1)^2} \times \int n_e \sigma_T \frac{\mathbf{v}_p}{c} \cdot \mathbf{dl} \tag{2.4}$$

where $\mathbf{v}_p$ is the bulk velocity of the IC gas relative to the CMB rest frame, and c is the speed of light. This functional form for the kinematic SZ effect has the same spectral shape as a primary CMB anisotropy, which represent a source of confusion to measurements of the kinematic effect.

An analytic expression for the relativistic kinematic SZ effect has been calculated by [78] as a power series expansion of $\theta_e = kT_e/mc^2$ and $\beta = v_p/c$, where $v_p = \mathbf{v}_p \cdot \hat{\mathbf{l}}$ is the radial component to the peculiar velocity. They found the relativistic corrections to the intensity to be on the order of +8% for a cluster with electron temperature $kT_e = 10$ keV and $v_p = 1000$ km s^{-1}. Although this is a relatively small correction to our final results, we use their calculation in this paper. We express the spectral shift due to the kinematic SZ effect as:

$$\Delta I_K = -I_0 \times \tau \times \frac{\mathbf{v}_p \cdot \hat{\mathbf{l}}}{c} \times h(x, T_e) \tag{2.5}$$

where $h(x, T_e)$ is given by:

$$h(x, T_e) = \frac{x^4 e^x}{(e^x - 1)^2} \times \left[1 + \theta_e C_1(x) + \theta_e^2 C_2(x)\right] \tag{2.6}$$

and $\theta_e = kT_e/m_ec^2$. This expression includes terms up to $O(\beta\theta_e^2)$. The quantities $C_1(x)$ and $C_2(x)$ are fully specified in [78], who have also calculated corrections to equation (2.6) up to $O(\beta^2)$. They find the correction from these higher order terms to be +0.2% for a cluster with $kT_e = 10$ keV and $v_p = 1000$ km s^{-1}, at a level far below the sensitivity of our observations. Therefore it can be safely ignored.

Chapter 3

SuZIE II

In this thesis I report measurements of the Sunyaev-Zeldovich effect made with the second generation Sunyaev-Zeldovich Infrared Experiment receiver (SuZIE II). SuZIE II is a bolometric array which measures the SZ effect simultaneously in three mm-wave atmospheric windows situated around the null of the thermal SZ effect. The instrument was designed to separate the thermal and kinematic components of the SZ spectrum towards clusters at intermediate redshift ($0.15 \lesssim z \lesssim 1.0$). In this chapter I describe the experimental details of the SuZIE II instrument.

3.1 The Cryostat

The SuZIE II cryostat was manufactured by Infrared Laboratories Inc[1]. The cryostat is a modification of their HDL-8 dewar, where the dewar has been lengthened to accommodate the SuZIE II focal plane and to increase the capacity of the nitrogen and helium vessels, to 4.5 and 3.0 liters respectively. During observation, the liquid helium bath is pumped on to reduce the helium cold plate temperature to $\sim$1.6 K. The hold time of the pumped helium bath is $\sim$16 hours and the hold time of the nitrogen bath is $\sim$12 hours. Because we pump on the helium bath, it was essential to design this stage so that it could hold over an entire night. The focal plane is

[1]Infrared Laboratories Inc., 1808 East 17th Street, Tucson, AZ 85719

attached to the helium cold plate by Vespel[2] legs, which thermally insulate the focal plane from the helium stage. The focal plane is cooled to 300 mK by a ^{3}He sorption pump refrigerator. During observation the focal plane's temperature is regulated to $\sim$315 mK using a custom built temperature controller which is described in Holzapfel [53]. This system reduces fluctuations in the focal plane temperature to < 150nK Hz$^{-1/2}$ on time-scales of 100 seconds.

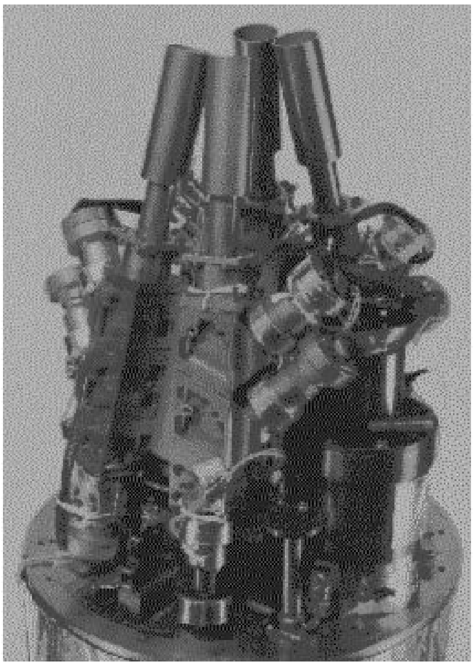

Fig. 3.1.— A photograph of the SuZIE II focal plane.

3.2 Optics

The SuZIE II receiver makes observations using the Caltech Submillimeter Observatory (CSO) located on Mauna Kea. The CSO consists of a 10.4 m primary mirror in a hexagonally-segmented design with a surface accuracy sufficient for sub-millimeter

[2]DuPont

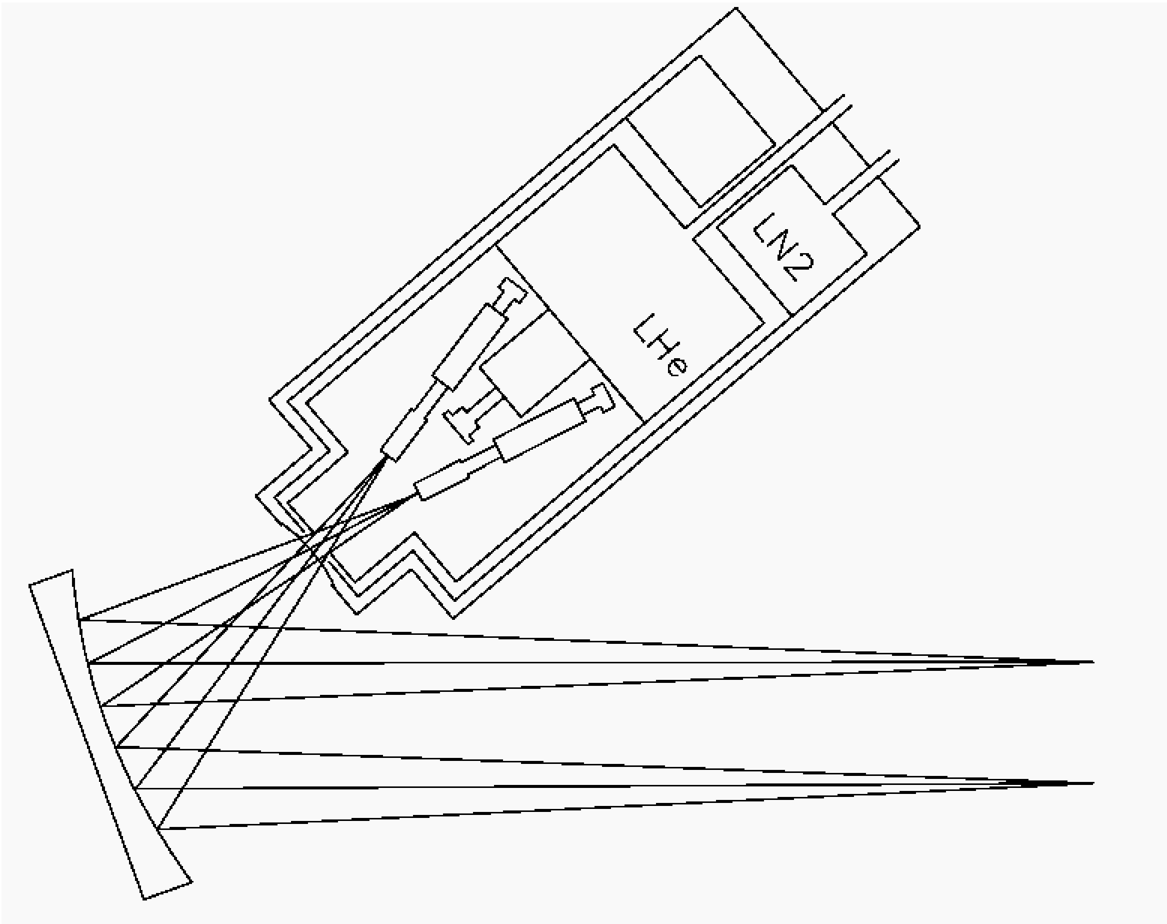

Fig. 3.2.— The optical configuration for the SuZIE II instrument. Light from the CSO Cassegrain focus is coupled into the SuZIE II cryostat by an aluminum tertiary mirror. Figure courtesy of P.D. Mauskopf.

wavelength observations. Mauna Kea is historically known as one of the premier locations in the world for sub-millimeter astronomy due to the low amount of perceptible water vapor at the site, which is typically less than 2mm for >60% of the nights.

The SuZIE II focal plane consists of a 2 × 2 arrangement of 3-color photometers that observe the sky simultaneously in each frequency band. A picture of the SuZIE II focal plane can be seen in Figure 3.1. Light is coupled to the photometers through Winston horns which over-illuminate a 1.6K Lyot stop placed at the image of the primary mirror formed by a warm tertiary mirror. Each photometer defines a $\sim 1\overset{'}{.}5$ FWHM beam, with each row separated by $\sim 2\overset{'}{.}3$ and each column by $\sim 5'$ on the sky. The beam size was chosen to correspond to typical cluster sizes at intermediate redshift ($0.15 \lesssim z \lesssim 1.0$).

Light from the CSO secondary is coupled to the SuZIE II receiver through an off-axis ellipsoidal tertiary mirror, see Figure 3.2. The CSO secondary feeds the Cassegrain focus with a f/10 beam which is converted to a f/4 beam into the cryostat through an off-axis ellipsoidal tertiary mirror. The tertiary and two flat mirrors are housed in an optics box to which the SuZIE II cryostat attaches directly. The inside of the optics box is covered with Eccosorb LS-30[3] foam to minimize reflections. Between November 1996 and November 1997, the SuZIE II optics were changed slightly, altering both the beam size and chop throw. Most of the observations in this thesis were taken in the later configuration, described above. For a description of the previous optics configuration see Mauskopf [73].

3.3 Definition of the Data Set

We now define some notation to aid in our discussion of the data channels. Each photometer contains three bolometers each observing at a different frequency. Details of the bolometers can be found in section 3.5, and details of the filters can be found in section 3.4. During an observation, the six difference signals that correspond to the spatially chopped intensity on the sky at three frequencies, and in two rows, are

[3]http://www.eccosorb.com

recorded. The differenced signal is defined as:

$$D_k = S_k^+ - S_k^- \tag{3.1}$$

where $S_k^{\pm}$ is the signal from each bolometer in the differenced pair. Because of the spacing of the photometers, this difference corresponds to a $5'$ chop on the sky. The subscripts $k = 1, 2, 3$ refer to the frequency bands of 355 GHz (or 273 GHz), 221 GHz and 145 GHz respectively in the row that is on the source. The subscripts $k = 4, 5, 6$ refer to the same frequency set but in the row that is off-source (see Figure 4.1 in Chapter 4). In addition to the differenced signal, one bolometer signal from each pair is also recorded, to allow monitoring of common-mode atmospheric signals. These six "single-channel" signals are referred to as S_k, where k is the frequency subscript previously described. For example, the difference and single channel at 145 GHz of the on-source row will be referenced as D_3 and S_3. For historical reasons, sometimes the "single-channel" signals will be referred to as C_k instead of S_k, however they are equivalent. Both the differences and the single channels are sampled at 7 Hz.

3.4 Filters

There are two levels of filters in the SuZIE II instrument. The first set is meant to minimize the radiation load on the L^4He and 300 mK stages, while the second set are band defining filters, which select the frequency of light reaching the detectors. Both sets of filters were constructed by the Astronomy Instrumentation group at Cardiff University lead by Peter Ade.

A schematic of the first set of filters in SuZIE II can be seen in Figure 3.3. Light enters the cryostat through a 0.002" polypropylene window. Immediately following the window mounted on the LN_2 stage is a 540 GHz low pass filter constructed from layers of metallized polyethylene hot-pressed together. Mounted on the L^4He stage are three filters; a thin dielectric absorber consisting of a Thallium Bromide high frequency absorber with a cutoff frequency of 1600 GHz, a layer of black polyethylene for higher frequency blockage, and another low pass filter with a cutoff frequency of

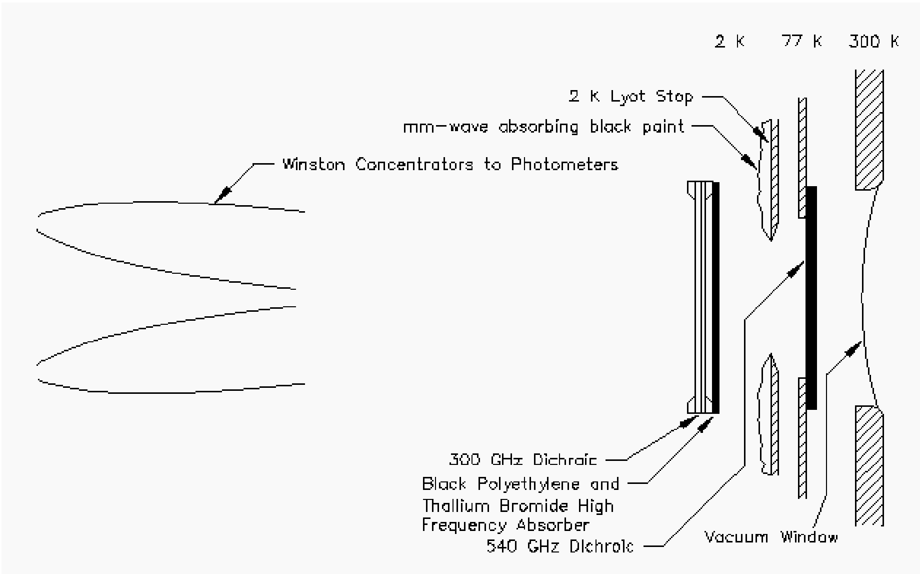

Fig. 3.3.— The first level of filters in the SuZIE II receiver. These filters reduce the heat load on inside of the cryostat and are designed to prevent high frequency radiation (>500 GHz) from reaching the Winston horns on the photometers. Figure courtesy of P.D. Mauskopf.

450 GHz. This set of filters provides ∼60% transmission in band while reducing the radiation load on the 300 mK state to a few μW under typical loading conditions at the CSO.

A second set of filters, which define the observed frequency bands, are located inside photometers on the focal plane. A schematic of an individual photometer can be seen in Figure 3.4. Contained in each photometer are two dichroic beamsplitters, with cutoff frequencies of 250 and 200 GHz respectively. The beamsplitters reflect light above and transmit light below their cutoff frequency. In this way the beamsplitters separate the incoming light into three frequency bands towards three different detector ports. Attached to each port is a bandpass filter followed by a reconcentrating horn which leads to a bolometer. The three bandpass filters transmit light at ∼145, 221, and 355 GHz respectively. These bands were chosen to overlap with atmospheric transmission windows at Mauna Kea, see Figure 3.5.

The transmission of the frequency bands were measured using a Michelson Fourier

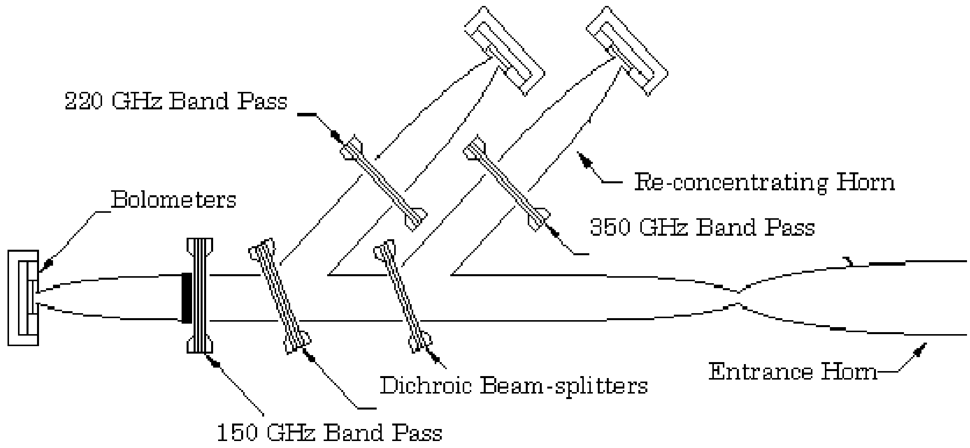

Fig. 3.4.— A schematic of a photometer in the SuZIE II focal plane.

Transform Spectrometer (FTS). The Michelson FTS uses a chopped load as its source which alternates between 300 K and 77 K eccosorb sheets. The chopper wheel is placed near the focus of an off-axis parabolic mirror, which collimates the light and re-directs it towards a mylar beamsplitter. From the beamsplitter light is either transmitted towards a movable flat mirror, or reflected towards a stationary flat mirror. Both flat mirrors reflect the light back to the beamsplitter, where approximately half the light is re-directed towards a second off-axis parabolic mirror which focuses the light into the SuZIE II instrument. An interferogram is taken by moving the movable flat mirror around zero path length difference. The transmission of the passband can be recovered by taking a fourier transform of the interferogram, which we correct for the transmission of the beamsplitter and the blackbody spectrum of the source. Figure 3.6 is a plot of the transmission spectra for all 12 of the SuZIE II detectors.

From the transmission spectra a band centroid and band width are calculated in order to quantify the band shape. I define $f_{kr}^{+/-}(\nu)$ as the transmission spectrum of the positive, or negative, channel of the difference channel in frequency band k and photometer row r. From a generic transmission spectrum, $f(\nu)$, its band centroid is

Table 3.1. SuZIE Bandpasses

Channel[a]	1996 ν_0 [GHz]	1996 $\Delta\nu$ [GHz]	1997-present ν_0 [GHz]	1997-present $\Delta\nu$ [GHz]
273/355 GHz				
S_{10}^{+}	274.0	32.6	355.1	30.3
S_{10}^{-}	272.8	28.8	354.2	31.1
S_{11}^{+}	272.9	30.3	356.7	30.8
S_{11}^{-}	272.3	30.6	354.5	31.5
221 GHz				
S_{20}^{+}	222.2	22.4	221.4	21.8
S_{20}^{-}	220.0	23.1	220.5	23.8
S_{21}^{+}	220.7	24.8	221.7	22.9
S_{21}^{-}	220.0	24.1	220.8	21.7
145 GHz				
S_{30}^{+}	146.1	19.9	145.2	18.1
S_{30}^{-}	146.4	21.3	144.6	18.6
S_{31}^{+}	145.0	20.7	145.5	18.2
S_{31}^{-}	144.4	19.5	144.9	17.4

[a]The notation is of the form $S_{\mathrm{freq,row}}$ and the $\pm$ sign refers to the sign of the channel in the differenced data.

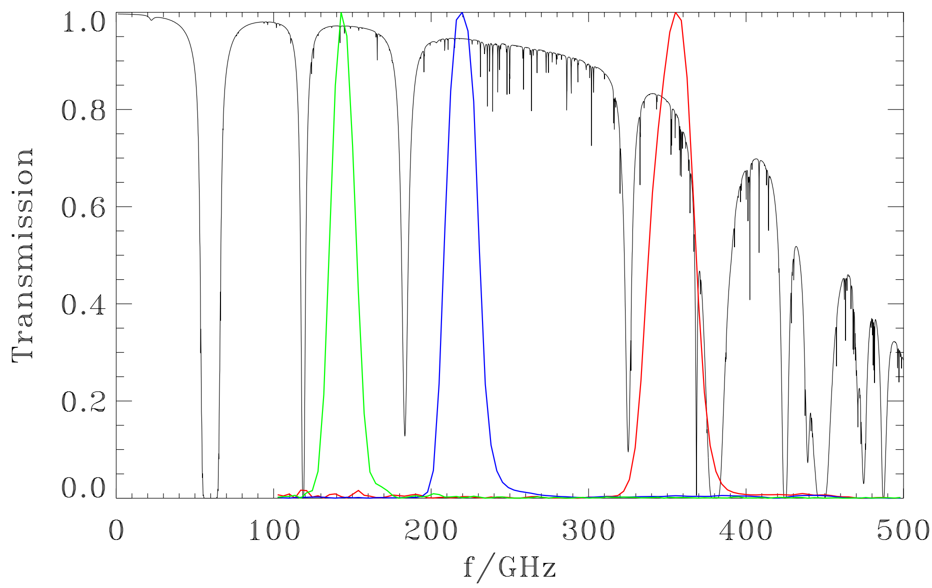

Fig. 3.5.— The atmospheric transmission at Mauna Kea assuming 1mm of perceptible water vapor, calculated by the atmospheric transmission program of Darek Lis found at http://www.submm.caltech.edu/cso/weather/atplot.html. Over-plotted are the SuZIE II frequency bands at 145, 221, and 355 GHz which are normalized to unity transmission.

defined as

$$\nu_0 = \frac{\int \nu f(\nu) d\nu}{\int f(\nu) d\nu} \tag{3.2}$$

and the band width is defined as

$$\Delta\nu = \int f(\nu) d\nu \tag{3.3}$$

where $f(\nu)$ has been normalized to unity at its peak in transmission. The values for the band centroid and band width for each of the 12 detectors are given in Table 3.1.

As was mentioned in section 3.2, between November 1996 and November 1997, the SuZIE II optics were changed slightly, altering both the beam size and chop throw. During this time the high frequency band in the SuZIE II receiver was moved to 355 GHz from 273 GHz to improve the degree to which correlated atmospheric noise can be removed from the data [71]. The band centroid and band width measured in both

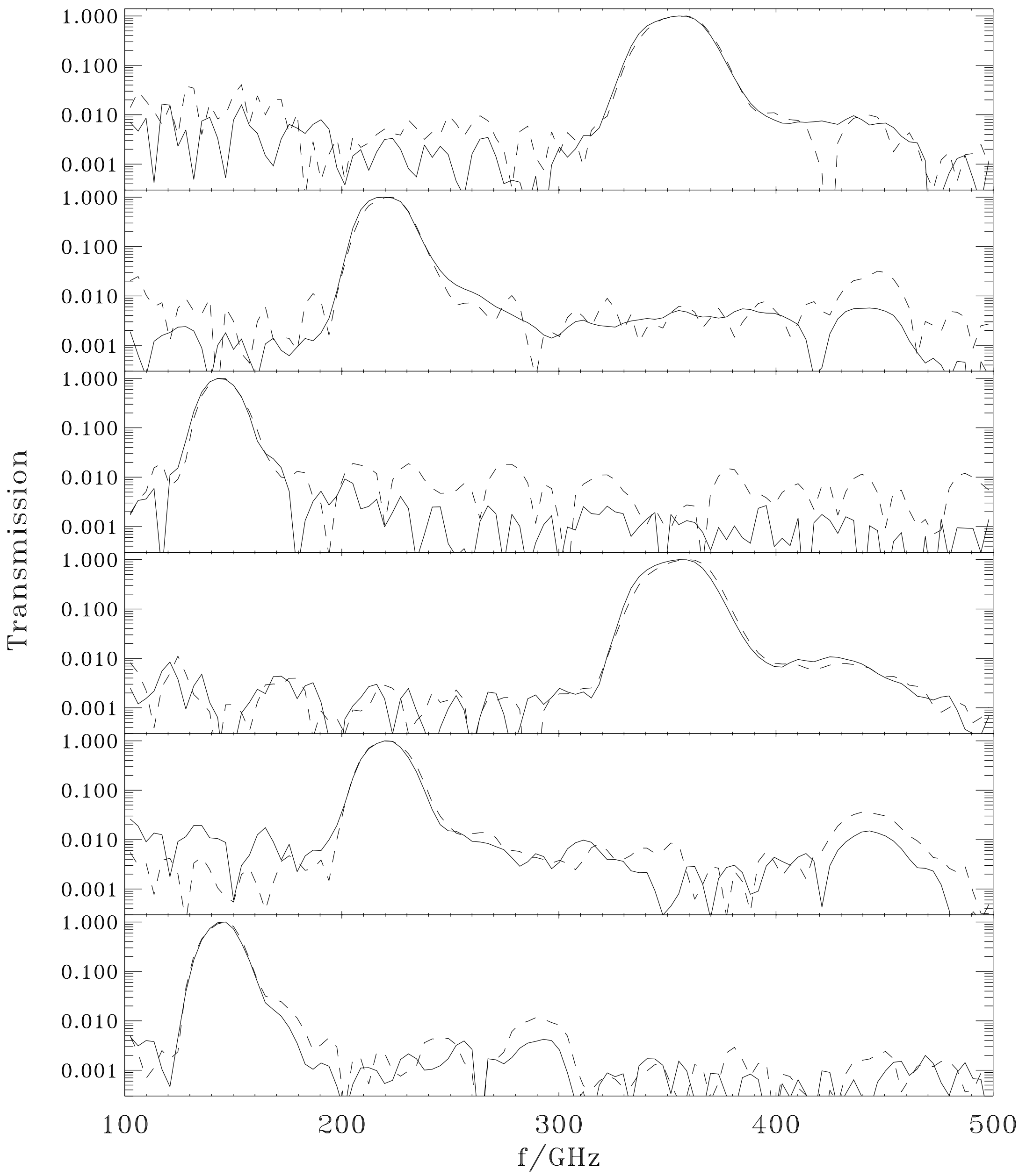

Fig. 3.6.— Transmission spectra for all 12 bolometers in SuZIE II. From top to bottom are channels C1, C2, C3, C4, C5, and C6. The solid lines are the negative channels and the dashed lines are the positive channels.

filter configurations is given in Table 3.1.

Out-of-band leaks are tested for with the transmission spectra and by performing photometric tests using a thick grill filter. No noticeable leaks appear in the transmission spectra for any of the channels out to ~ 3500 GHz. However, the total out-of-band power can be directly measured by comparing the signal from a chopped liquid nitrogen load with and without a thick grill high pass filter. This method gives an upper limit to the out-of-band power in each channel. The upper limit to the ratio of out-of-band to in-band power for a Rayleigh-Jeans source of arbitrary temperature is given in Table 3.2 for each frequency band. This ratio is measured to be $< 0.4\%$ for all channels.

The end-to-end optical efficiency of the instrument is measured by comparing the measured optical power to the expected optical power looking into blackbody loads at 77 and 300 K. The operating temperature of a bolometer is determined by the power balance equation

$$Q + P_e = \int_{T_{\mathrm{bath}}}^{T_{\mathrm{bolo}}} G(T)dT \tag{3.4}$$

where Q is the incident optical power, P_e is the electrical power, T_{bath} is the temperature of the thermal bath, T_{bolo} is the bolometer temperature, and $G(T)$ is the thermal conductivity of the thermal link between the two. The right hand side of equation 3.4 only depends on the temperature of the bolometer, or equivalently its resistance. Therefore by comparing bolometer load curves taken under different loading conditions at points of equal resistance, the difference in electrical power must be equal to

Table 3.2. The Ratio of Out-of-Band to In-Band Power for a RJ source

Channel [GHz]	Ratio
145	< 0.003
221	< 0.004
273	< 0.003
355	< 0.004

the difference in optical power. I have taken load curves with the receiver looking at sheets of unpainted cones of Eccosorb CV-3[4] at room temperature and immersed in LN^2. From these measurements, I define an optical efficiency, η, as

$$\eta = \frac{P_e^{300} - P_e^{77}}{A\Omega \int 2k(300-77)(\nu/c)^2 f(\nu) d\nu} \tag{3.5}$$

where $f(\nu)$ is the filter response, $A\Omega$ is the throughput of the receiver, and P_e^{300} and P_e^{77} are the electrical power at a given resistance while the receiver is looking at 300 K and 77 K loads, respectively. It is noted that $f(\nu)$ is normalized to unity transmission at its maximum. By assuming uniform illumination of the Lyot stop by the concentrating horns, we calculate $A\Omega = 0.07$ cm^2 str. In Table 3.3, I give the end-to-end optical efficiency of each channel calculated using equation 3.5.

3.5 Detectors

The detectors in SuZIE II are spider-web micromesh bolometers developed by the Micro-devices Laboratory at JPL [72], see Figure 3.7. The bolometer absorber consists of a thin film of metal evaporated on a silicon nitride substrate. A Neutron Transmutation Doped (NTD) Germanium thermistor with Nb-Ti wire for its electrical leads is attached to the absorber with epoxy. This type of bolometer has been deployed in several successful CMB experiments, including the ACBAR [93] and BOOMERanG [23] experiments.

The resistance, R, of the thermistor is well fit as a function of temperature, T, where

$$R(T) = R_0 \exp\left(\sqrt{\frac{\Delta}{T}}\right) \tag{3.6}$$

where R_0 and Δ are characteristic parameters for each bolometer. Usually for a bolometer $R(T)$ is measured by blanking off the detector to light and applying a small bias current to measure its resistance at several different temperatures. The bias current should be small enough so that electrical self heating in the bolometer

[4]http://www.eccosorb.com

Table 3.3. Optical Efficiency

Channel[a]	Frequency Band [145 GHz]	[221 GHz]	[271 GHz][c]	[355 GHz]
S^{+}_{k0}	0.130	0.179	0.176	0.315
S^{-}_{k0}	0.138	0.181	0.181	0.304
S^{+}_{k1}	0.125	< 0.175[b]	0.177	0.288
S^{-}_{k1}	0.135	< 0.188[b]	0.183	0.312
Mean	0.132	0.180[d]	0.178	0.305
RMS	0.006	0.002[d]	0.004	0.012

[a]The notation is of the form $S_{\mathrm{freq,row}}$ and the $\pm$ sign refers to the sign of the channel in the differenced data.

[b]The electrical power across the bolometer could not be increased enough during the 77K load curve to lower the resistance to a level matching the resistance during the 300 K load curve. Therefore we were only able to derive lower limits to the optical efficiency in this case.

[c]Results taken from Mauskopf [73].

[d]These results are only calculated from the two S^{+}_{20} and S^{-}_{20}.

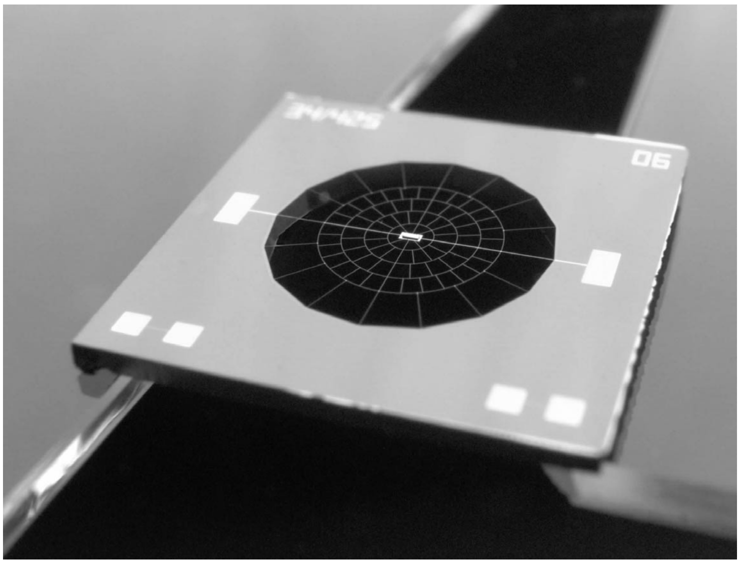

Fig. 3.7.— A picture of a spider-web bolometer similar to the type of bolometers used in SuZIE II. How the spider-web bolometer got its name is evident in the picture, as the layout of the silicon nitride substrate is visibly reminiscent of a spider-web. Image credit: J.J. Bock (JPL)

does not raise its temperature substantially above the focal plane temperature. By controlling the temperature of the focal plane with a heater and repeating the resistance measurement at several different temperatures, one directly measures $R(T)$. These results can then be fit to equation 3.6 to give R_0 and Δ. In Table 3.4, we give R_0 and Δ for the 12 bolometers in SuZIE II.

3.6 Calibration and Beamshapes

We use Mars, Uranus and Saturn for absolute calibration and to measure the beam shape of our instrument. The brightness temperature of each planet is well-studied in the millimeter wavelength regime which makes them ideal calibrators.

The expected intensity of a planetary calibrator is:

$$I_{\rm plan} = \frac{\int 2k\,(\frac{\nu}{c})^2\, T_{\rm plan}(\nu)\, f_k(\nu) d\nu}{\int f_k(\nu) d\nu} \tag{3.7}$$

Table 3.4. Bolometer Parameters

Channel[a]	R_0 [Ω]	Δ [K]
273/355 GHz		
S_{10}^{+}	56.8	49.45
S_{10}^{-}	58.0	46.69
S_{11}^{+}	42.4	52.14
S_{11}^{-}	41.5	52.42
221 GHz		
S_{20}^{+}	40.5	50.7
S_{20}^{-}	36.6	50.8
S_{21}^{+}	27.9	50.70
S_{21}^{-}	26.1	50.75
145 GHz		
S_{30}^{+}	18.3	53.2
S_{30}^{-}	20.0	52.6
S_{31}^{+}	21.9	52.1
S_{31}^{-}	22.4	52.2

[a]The notation is of the form $S_{\mathrm{freq,row}}$ and the $\pm$ sign refers to the sign of the channel in the differenced data.

with $T_{\rm plan}(\nu)$ being the Rayleigh-Jeans (RJ) temperature of the planet, and $f_k(\nu)$ the transmission function of channel k, whose measurement is described later in this section. The transmission of the atmosphere is corrected for by measuring the opacity using a 225 GHz tipping tau-meter located at the CSO. This value is converted to the opacity in each of our frequency bands by calculating a scaling factor α_k which is measured from sky dips during stable atmospheric conditions. For the frequency bands at 145, 221, 273, and 355 GHz we find $\alpha = 0.8, 1.0, 2.7$, and 5.8. From drift scans of the planet I measure the voltage, $V_{\rm peak}$ that is proportional to the intensity of the source. One then finds that the responsivity to a celestial source is:

$$R = \frac{I_{\rm plan}\Omega_{\rm plan} \times e^{-\alpha<\tau/\cos\theta_{\rm Cal}>}}{V_{peak}}\left[\frac{Jy}{V}\right] \tag{3.8}$$

where $\Omega_{\rm plan}$ is the angular size of the planet, and $<\tau/\cos\theta_{\rm Cal}>$ is averaged over the length of the observation, typically less than 20 minutes. Generally, at least one calibration source is observed per night.

The data are then calibrated by multiplying the signals by a factor of $R \times e^{\alpha<\tau/\cos\theta_{\rm SZ}>}$. The transmission of the atmosphere is corrected for during each cluster observation using the same method as for the calibrator observations. Each cluster scan is multiplied by $e^{\alpha<\tau/\cos\theta_{\rm SZ}>}$, where $<\tau/\cos\theta_{\rm SZ}>$ is averaged over the length of that night's observation of the cluster, typically less than three hours. The atmospheric transmission is averaged over the observation period to reduce the noise associated with the CSO tau-meter measurement system [5]. To determine whether real changes in τ over this time period could affect our results, we use the maximum variation in $<\tau/\cos\theta_{\rm SZ}>$ over a single observation, and estimate that ignoring this change contributes a $\pm 2\%$ uncertainty in our overall calibration.

The uncertainty of $I_{\rm plan}$ is dominated by uncertainty in the measurement of $T_{\rm plan}(\nu)$. Measurements of RJ temperatures at millimeter wavelengths exist for Uranus [47], Mars and Saturn [44]. Griffin & Orton model their measured Uranian temperature spectrum, $T_{\rm Uranus}(\nu)$, with a third order polynomial fit to the logarithm of wavelength. They report a 6% uncertainty in the brightness of Uranus. We determine the Martian temperature spectrum over our bands from the FLUXES software

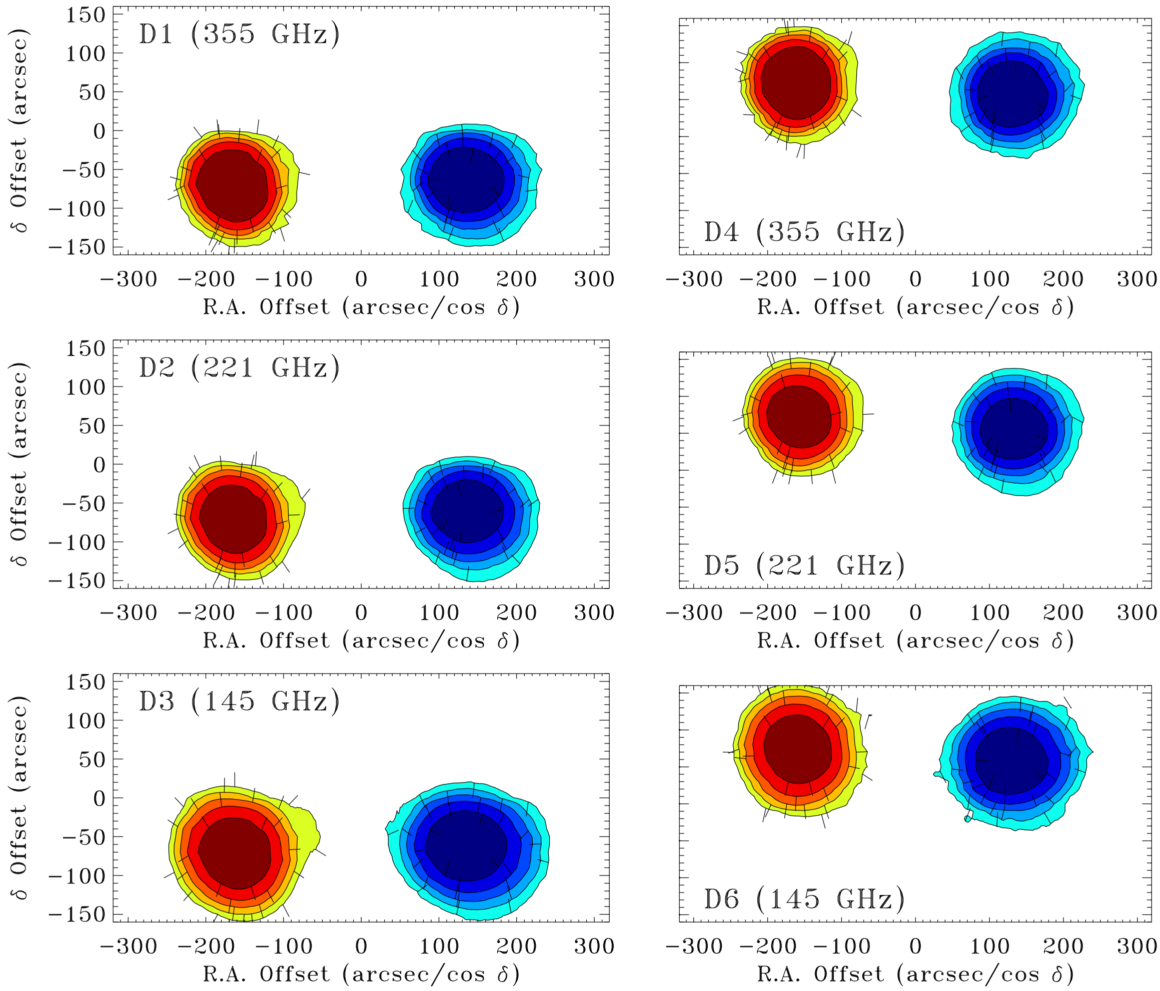

Fig. 3.8.— A beam map of the six differential channels in SuZIE II made from a raster scan over Saturn. Contours are separated in 3 dB intervals.

package developed for the JCMT telescope on Mauna Kea. [5] We fit the temperature spectrum given by FLUXES with a second order polynomial fit to the logarithm of wavelength in order to allow us to interpolate over our frequency range. The reported uncertainty on the Martian brightness temperature is 5%. Goldin et al. report RJ temperatures of Mars and Saturn in four frequency bands centered between 172 and 675 GHz. From these measurements we fit a second order polynomial in frequency to model $T_{\rm Saturn}(\nu)$. Goldin et al. report a $\pm$10K uncertainty to the RJ temperature of Mars due to uncertainty from their Martian atmospheric model, which translates to a 5% uncertainty in the brightness. They then use their Martian calibration to cross-calibrate their measurements of Saturn. Not including their Martian calibration error, they report a $\sim$2% uncertainty to Saturn's RJ temperature. Adding the Martian calibration error in quadrature yields a total 5% uncertainty to the brightness of Saturn. Since we use a combination of all three planets to calibrate our data, we estimate an overall $\pm 6\%$ uncertainty to $T_{\rm planet}$.

The rings of Saturn have an unknown effect on its millimeter wavelength emission. During our November 1997 observing run, while Saturn was at a ring angle of $-8.8°$, Saturn and Uranus were observed over several nights. Comparing the calibration factors derived from the observations of the two planets, there was no systematic difference above their known level of calibration uncertainty. Therefore for Saturn ring angles between $\pm 9°$ we have occasionally used Saturn for primary calibration. However due to the lack of any other visible planets, Saturn was the primary calibrator during the January 2002 run when Saturn was at a ring angle of $\sim -25.8°$. Fortuitously, during the December 2002 run calibration scans were taken of Uranus and Saturn over several nights with Saturn at a ring angle of $\sim -26.6°$. Comparing the scans of the two planets, Saturn was observed to have excess emission by $\sim 72, 43$, and 37% in our 355, 221, and 145 GHz frequency bands. Saturn was not used as a primary calibrator during this run, but because the ring angle of Saturn changed by less than a degree between January 2002 and December 2002, we use the cross-calibration of Saturn from Uranus measured in December 2002 to correct the calibration from Saturn for the January 2002 run. For the data presented in this

[5] http://www.jach.hawaii.edu/JACpublic/JCMT/software/bin/fluxes.pl

thesis, this correction only affects the measurements of MS1054, see Table 4.1.

Raster scans over Saturn and Mars were used to measure the beam shape during each observing run. In Table 3.5, we give a summary of the SuZIE II beam sizes for both the 1996 and 1997-present optical configurations of SuZIE II. During the observing runs described in this thesis, the angular diameter of Mars ranged between $4-12$ arcsec and the angular diameter of Saturn ranged between $14-20$ arcsec. Compared to our typical beam size of $\sim 90''$, both Mars and Saturn are sufficiently small to be well approximated as point sources.

[71] has found that the SuZIE II beam shapes have a systematic dependence on the rotation angle of the dewar, which affects the overall calibration of the instrument. Based on these measurements we assign a $\pm 5\%$ calibration uncertainty from this effect. Further uncertainty to the calibration arises from our measurement of the spectral response, $f_k(\nu)$, which affects both the intensity that we measure from the planetary calibrators and the SZ intensity. The spectral response of each SuZIE II channel was measured with a Michelson Fourier Transform Spectrometer (FTS). We then use the scatter of the measurements of the four bolometers that measure the same frequency to estimate the uncertainty in the spectral calibration at that frequency. We estimate this uncertainty to be $<1\%$ of the overall calibration.

Bolometers have a responsivity that can change with the amount of power loading on the detector; such non-linearities can potentially affect the results of calibration on a bright planet and the response of the detectors during the course of a night. We have used laboratory measurements to determine the dependence of responsivity on optical power loading. We estimate the variation in our loading from analysis of sky-dips taken at the telescope, and the calculated power received from Saturn, which is the brightest calibrator that we use. Over this range of loading conditions the maximum change in detector response is $\sim 7.0\%, 8.0\%$, and 3.5% in our 145, 221, and 355 GHz frequency bands respectively. Since the responsivity change will be smaller for the majority of our observations, we assign a 6% uncertainty in the calibration error budget for this effect.

The calibration uncertainties are summarized in Table 3.6. Adding all of these sources in quadrature, we estimate the total calibration uncertainty of SuZIE II in

Table 3.5. SuZIE Beamsizes

	1996		1997-present	
Channel[a]	FWHM [arcmin]	Ω [arcmin^2]	FWHM [arcmin]	Ω [arcmin^2]
273/355 GHz				
S_{10}^{+}	1.35	1.85	1.50	2.17
S_{10}^{-}	1.30	1.79	1.54	2.42
S_{11}^{+}	1.25	1.65	1.57	2.24
S_{11}^{-}	1.30	1.76	1.60	2.58
221 GHz				
S_{20}^{+}	1.30	1.64	1.36	1.90
S_{20}^{-}	1.25	1.67	1.40	2.08
S_{21}^{+}	1.15	1.53	1.47	2.02
S_{21}^{-}	1.20	1.54	1.40	2.18
145 GHz				
S_{30}^{+}	1.45	2.14	1.50	2.35
S_{30}^{-}	1.40	2.16	1.64	2.73
S_{31}^{+}	1.30	1.86	1.60	2.51
S_{31}^{-}	1.35	1.91	1.60	2.73

[a]The notation is of the form $S_{\mathrm{freq,row}}$ and the ± sign refers to the sign of the channel in the differenced data.

Table 3.6. Break down of the calibration uncertainties

Source	Uncertainty (%)
Detector non-linearities	6
Planetary temperature	6
Atmospheric τ	2
Spectral response	1
Beam uncertainties	5
Total	10

each of its spectral bands to be ±10%.

3.7 Atmospheric Loading

At the telescope we take measurements of the loading on the detectors as a function of zenith angle. This type of measurement is generically called a skydip. It can be used to separate the different contributions to the loading on the detectors and to measure the opacity of the atmosphere.

Figure 3.9 shows a skydip for the 6 frequency channels in SuZIE taken on 2000 November 17. We calibrate the optical power during the skydip from dark load curves taken in the laboratory. This is done in an analogous way as to the method used to calculate the optical efficiency in section 3.4, where we compare the electrical power at points of equal resistance to calculate the optical power incident on the detectors. To the measurements of optical power as a function of zenith angle, θ, for a frequency channel k, we fit the following equation

$$P_k(\theta) = P_{k,\mathrm{tel}} + P_{k,\mathrm{atm}}(\theta) \tag{3.9}$$

where

$$P_{k,\mathrm{atm}}(\theta) = P^{\mathrm{total}}_{k,\mathrm{atm}} \left(1 - \exp(-\alpha_k \tau_{225\mathrm{GHz}}/\cos\theta)\right) \tag{3.10}$$

where $P_{k,\mathrm{tel}}$ is the loading from the telescope, $P_{k,\mathrm{atm}}(\theta)$ is the loading from the atmosphere, $\tau_{225\mathrm{GHz}}$ is the opacity measured by the CSO tau-meter, and α_k scales the atmospheric opacity measured at 225 GHz to the SuZIE II frequency bands and is defined in section 3.6. During the skydip in Figure 3.9 the CSO tau-meter measured an atmospheric opacity of $\tau_{225\mathrm{GHz}} = 0.036$. In Table 3.7 we give the power and brightness temperature of the telescope and the atmosphere calculated from the fit to equation 3.9 for the measurements shown in Figure 3.9.

To check for any spurious sources of loading, we compare the calculated brightness temperatures in Table 3.7 with previous measurements by Holzapfel [53] with the SuZIE I instrument. The telescope power given in Table 3.7 is not necessarily only from the telescope, but could originate from other sources of loading which do not

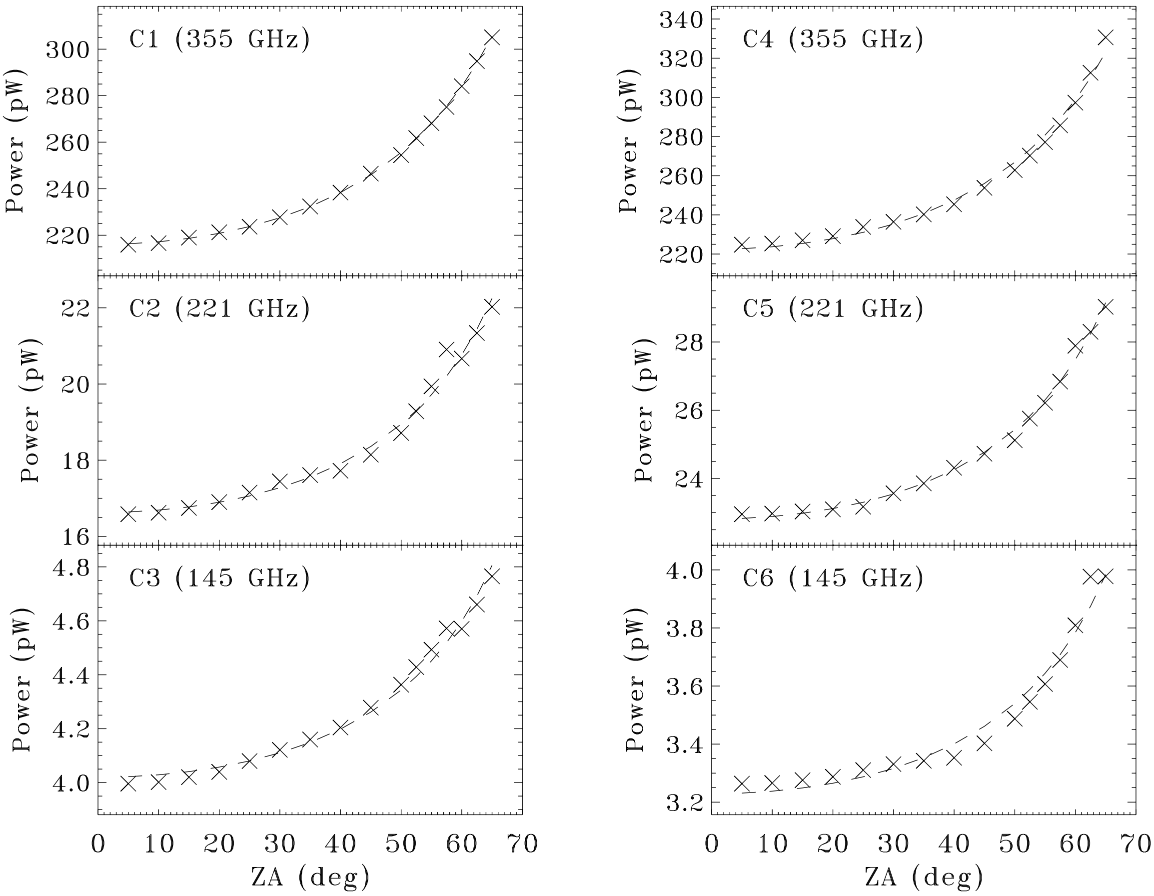

Fig. 3.9.— The optical power on each negative channel bolometer during a skydip taken at the CSO in November 2000. The dashed line is the best-fit curve fitting for the power from the telescope and the power from the atmosphere according to equation 3.9.

depend on zenith angle, such as loading from within the cryostat. The SuZIE I instrument measured a telescope brightness temperature of 29.6±4.0 and 26.1±2.2 K in its 142 and 217 GHz frequency channels. While these bands are not identical to the SuZIE II frequency bands, the SuZIE I measurements appear consistent with the results in the comparable frequency bands in SuZIE II. A telescope temperature of ∼30 K is also consistent with measurements from other instruments on the CSO. This brightness temperature is larger than most typical millimeter wavelength telescopes and is generally attributed to the scattering of light from the support structure for the secondary mirror. We have no measurements to compare to for the 355 GHz channels in SuZIE II, however there appears to be a significantly higher loading at 355 GHz than at either 145 or 221 GHz.

3.8 Sensitivity

The sources of noise in a bolometric system have been discussed in detail by other authors [see 70, 92, for example]. Typically the three types of noise relevant in bolometer systems are photon noise, detector noise, and electronics noise. The goal in building any instrument is to have the total instrument noise nearly equal to the photon noise limit, the noise due to the random arrival times of the photons, which fundamentally limits the sensitivity of all bolometric systems.

Photon noise originates in a bolometer system from random fluctuations in the arrival time of the individual photons. There are two mechanisms from which photon noise arises; standard shot noise, and the tendency of photons to arrive together due to bose statistics. The noise equivalent power (NEP) due to fluctuations in the number of photons absorbed by the bolometer is

$$NEP_\gamma^2 = \frac{2\int f(\nu)P(\nu)h\nu d\nu + \int f(\nu)P^2(\nu)/N d\nu}{\int f(\nu)d\nu} \tag{3.11}$$

where $f(\nu)$ is the frequency response of the system, $P(\nu)$ is the spectrum of the incident power, and N is the number of spatial modes. For a source whose power

Table 3.7. Background Power Contributions

Channel	Telescope [pW]	[K]	Atmosphere[a] [pW]	[K]
1−	132.8	52.4	95.1	37.5
2−	12.4	28.9	4.89	11.4
3−	3.46	31.6	0.67	6.1
4−	129.3	50.0	106.6	41.2
5−	18.1	42.7	5.54	13.1
6−	2.69	25.3	0.69	6.0

[a]The atmospheric contribution is calculated at a zenith angle of 30 degrees.

Table 3.8. Detector Information

Channel[a]	Q[b] [pW]	R_{bolo} [MΩ]	T_{bolo} [mK]	G [pW/K]	S [10^8 V/W]
145	6.2	2.15	391	285	-1.67
221	22.1	2.06	424	402	-1.27
355	430.0	1.22	499	3601	-0.28

[a]This refers to the negative channel in the on-source row.

[b]The total power incident on the detectors at a zenith angle of 30 degrees during a skydip when $\tau_{225\mathrm{GHz}} = 0.088$ at zenith.

does not vary much over the spectral band, this equation can be approximated by

$$NEP_{\gamma}^{2} \approx 2Qh\nu_0 + \frac{Q^2}{\Delta\nu} \tag{3.12}$$

where Q is the absorbed power by the bolometer. In Table 3.8 we give the incident optical power at a zenith angle of 30 degrees measured at the CSO during a skydip when $\tau_{225\mathrm{GHz}} = 0.088$ at zenith. This $\tau_{225\mathrm{GHz}}$ value is very close to the median year round value for Mauna Kea, and should therefore be a reasonable approximation of the typical optical power incident on the detectors while at the telescope. In Table 3.9 we give the calculated NEP_{γ} assuming the loading numbers in Table 3.8 and the spectral band information in Table 3.1.

Detector noise in a bolometer system arises from phonon shot noise and the Johnson noise of the thermistor. The first type of detector noise we consider is phonon shot noise due to the random transfer of energy between the bolometer and the thermal bath through their thermal link. The NEP from phonon shot noise is

$$NEP_{\mathrm{G}}^{2} = 4kT^2G \tag{3.13}$$

where T is the temperature of the bolometer and G is the thermal conductance between the bolometer and the thermal bath. The second type of detector noise is Johnson noise due to fluctuations in the resistance from the random thermal motions of the electrons in the resistor. The NEP from Johnson noise is

$$NEP_{\mathrm{J}}^{2} = \frac{4kTR}{S^2} \tag{3.14}$$

where R is the resistance of the thermistor, and S is the electrical responsivity of the detectors given in units of V/W. In Table 3.8 we give values for T, G, R, and S under typical loading conditions at the CSO. In Table 3.9 we give the calculated NEP_{G} and NEP_{J} assuming the detector parameters given in Table 3.8.

Electronics noise contributes to the total noise of the system through the cold JFET source followers and the warm readout electronics. The JFET source followers were measured to have a noise equivalent voltage (NEV) of $\sim$2 nV Hz$^{-1/2}$ [53]. Adding the JFET noise in quadrature with the specified noise from the pre-amplifier in the warm electronics, we expect the total NEV of the electronics to be $\sim$4 nV Hz$^{-1/2}$. The NEV can be converted into a NEP by dividing by the absolute value of the detector responsivity, S. The calculated NEP from the electronics is given in Table 3.9

In Table 3.9 we give the total NEP of SuZIE II, which is defined as the quadrature sum of the other sources of noise given in Table 3.9. The NEP can be converted into a noise equivalent flux density (NEFD) using the relation

$$NEFD = NEP\frac{\Omega_{\rm beam}}{A\Omega\eta\Delta\nu} \tag{3.15}$$

where $\Omega_{\rm beam}$ is the beamsize given in Table 3.5, $\Delta\nu$ is the band width given in Table 3.1, η is the optical efficiency and $A\Omega$ is the throughput, which are both given in section 3.4. The NEP can also be converted to a noise equivalent temperature (NET) using the relation

$$NET = \frac{T_{\rm CMB}}{I_0}\frac{(e^{x_0}-1)^2}{x_0^4 e^{x_0}}\frac{NEP}{A\Omega\eta\Delta\nu} \tag{3.16}$$

where $I_0 = 2(kT_{\rm CMB})^3/(hc)^2$, $x_0 = h\nu_0/kT$, where ν_0 is the band centroid given in Table 3.1. The $NEP_{\rm total}$ in Table 3.9 is also quoted as a NEFD and NET according to the above equations.

In Figure 3.10 we show the noise power spectral density (PSD) for the three on-source difference channels measured during observations of A2204 on 2003 March

Table 3.9. Sensitivity

Channel [GHz]	NEP_γ	NEP_G	NEP_J	NEP_E	$NEP_{\rm total}$	$NEFD_{\rm total}$ [mJy/$\sqrt{Hz}$]	$NET_{\rm total}$ [mK/$\sqrt{Hz}$]
		[10^{-17} W/$\sqrt{Hz}$]					
145	5.8	4.9	4.1	2.4	8.9	98	1.390
221	16.8	6.3	5.5	3.1	19.0	94	1.385
355	248.3	22.2	20.7	14.2	250.6	577	12.880

25. The Figure shows the PSD before and after the atmospheric subtraction which is performed in software and later described in Chapter 5. After atmospheric subtraction there is a significant improvement in the noise properties of the PSD for all frequency channels, with the 145 GHz channel near the NEFD calculated in Table 3.9 at signal frequencies above $\sim$ 80 mHz. This is important as drift scans of a source through our beams would appear at signal frequencies of $\sim$ 80 mHz. SuZIE I found that below 300 mHz excess noise from differential atmospheric emission dominated the overall noise of the instrument in all frequency channels [53]. The multi-frequency capability of SuZIE II allows an additional level of atmospheric subtraction which removes much of the residual atmospheric noise measured in SuZIE I. Figure 3.10 suggests that instrumental noise limits the sensitivity of the 145 GHz frequency band in SuZIE II, with detector noise contributing a significant amount to the overall noise.

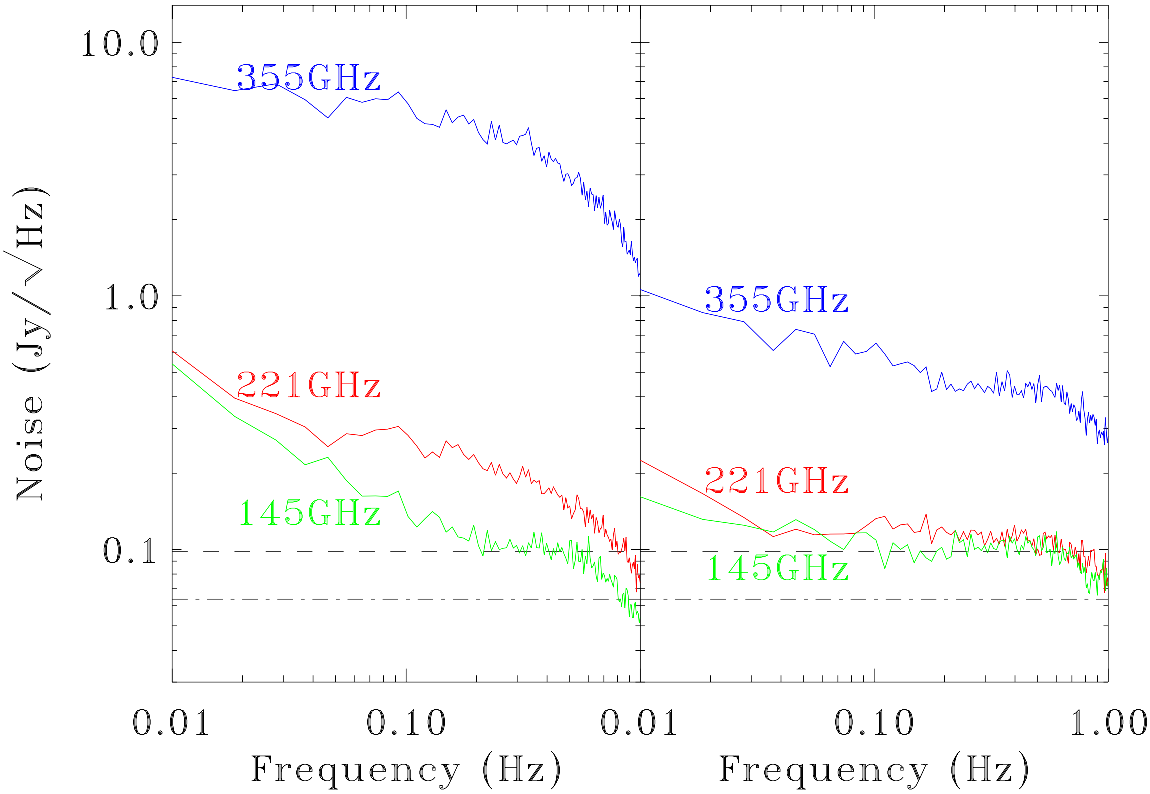

Fig. 3.10.— A noise power spectral density from observations of A2204 taken on 2003 March 25. The optical depth of the atmosphere at 225 GHz averaged over zenith angle during this observation was 0.075. The dot-dashed line is the photon noise limit of the 145 GHz channel and the dashed line represents the total noise limit of the 145 GHz channel calculated in section 3.8. (Left) The measured power spectral density for the three on-source differential frequency channels before the atmospheric subtraction outlined in Chapter 5. (Right) The measured power spectral density for the three on-source differential frequency channels after atmospheric subtraction.

Chapter 4

Observations

4.1 Scan Strategy

SuZIE II operates in a drift scanning mode, where the telescope is pointed ahead of the source and then parked. The Earth's rotation then causes the source to drift through the array of pixels. Before each scan the cryostat is rotated so that the rows of the array lie along lines of constant declination. Each scan lasts two minutes, or $30'$ in right ascension, during which time the telescope maintains a fixed altitude and azimuth. After a scan is complete, the telescope reacquires the source and the scan is then repeated. From scan to scan the initial offset of the telescope from the source is alternated between $12'$ and $18'$, allowing a systematic check for an instrumental baseline and a check for any time dependent signals. During the observations presented here, the array was positioned so that one row passed over the center of each cluster, as specified in Table 4.1.

There are two main reasons for drift scanning with SuZIE II. Firstly, drift scanning eliminates any time-dependent signal due to side-lobe pick-up from the telescope. The thermal background on the detectors is several orders of magnitude greater than the signal we are trying to measure, therefore any small variation in the background could still have a significant noise contribution. Secondly, bolometers are high-impedance devices which are inherently susceptible to micro-phonic noise from vibrations. Drift scanning eliminates this problem by keeping the cryostat and the telescope fixed

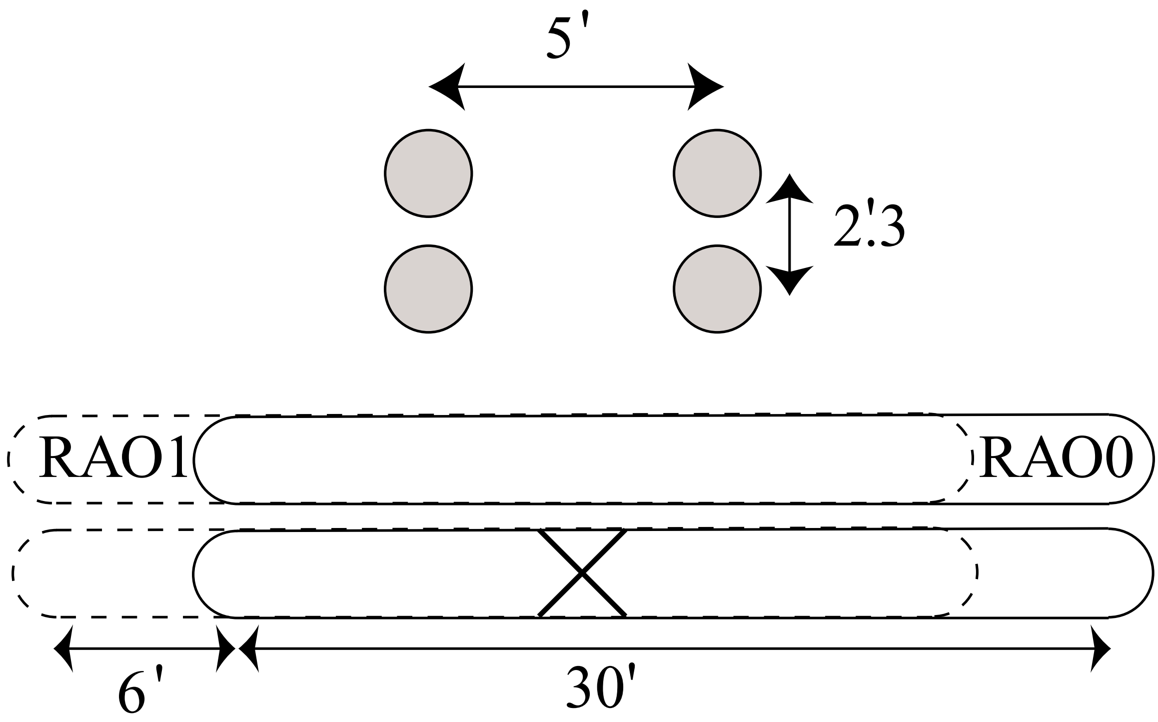

Fig. 4.1.— The upper panel shows the layout of pixels in the SuZIE II focal plane. The lower panel shows the pattern traced out on the sky by a single column of the array. The cross indicates the nominal pointing center of the observation.

during the observation.

Conversely, there are disadvantages to drift scanning. A significant amount of time is spent off-source for a $30'$ scan using only four $1.5'$ beams. The problem of observing efficiency is common to many millimeter wavelength measurements, as often times some sort of chopping or nodding scheme is required to subtract any position dependent offset. However, for the case of SuZIE II, any telescope movement during an observation causes enough micro-phonic noise to counter any advantage gained by observing efficiency. A second disadvantage of drift scanning is that the signal frequencies of a source are generally very low, because we rely on the rotation of the Earth to modulate the signal, and usually in a region of significant $1/f$ noise. An astronomical source moving across the sky at $0.25' \cos(\delta)/s$ measured by a $\sim 1.5'$ gaussian beam, would appear at a signal frequency of $\sim 83 \cos(\delta)$ mHz. From Figure 3.10, however, it appears that at these signal frequencies SuZIE II is not limited by $1/f$ noise, but instead operates near the noise limit of the instrument. For the above reasons, drift scanning is the logical choice as a scan strategy for SuZIE II.

4.2 Clusters

SuZIE II has detected a total of 13 clusters over the course of 13 observing runs between April 1996 and December 2003. These detections are summarized in Table 4.1. We selected bright, known X-ray clusters from the *ROSAT* X-Ray Brightest Abell Clusters [33, 34] and Brightest Cluster Samples [35]. We restrict ourselves to clusters at $z \gtrsim 0.15$ because clusters above this redshift tend not to be larger than the $5'$ separation between the differenced beams. In particular we selected clusters with published intra-cluster (IC) gas density models and electron temperatures that were previously unobserved with SuZIE, or that had weak peculiar velocity constraints from previous observations. We also aimed to maintain a somewhat uniform sky coverage in our search for a local dipole flow [see 9, 18].

Table 4.1. Summary of SuZIE observations

Source	z	R.A.[a] (J2000)	Decl.[a] (J2000)	Date	Scans[b] [N]	Time [hours]	Ref.
Cl0016	0.55	00 21 08.5	+16 43 02.4	Nov 96	277	9.2	1
A520	0.199	04 54 07.4	+02 55 12.1	Dec 02	435	14.5	2
MS0451	0.55	04 54 10.8	−03 00 56.8	Nov 96	348	11.6	1
″				Nov 97	211	7.0	
″				Nov 00	306	10.2	
MS0451				Totals	865	28.8	
A545	0.153	05 32 23.3	−11 32 09.6	Dec 98	266	8.9	3
A697	0.282	08 42 57.8	+36 21 54.0	Mar 03	254	8.5	2
A773	0.217	09 17 52.1	+51 43 48.0	Mar 03	83	2.8	2
ZW3146	0.29	10 23 38.8	+04 11 20.4	Nov 00	131	4.4	2
MS1054	0.823	10 56 58.6	−03 37 36.0	Jan 02	219	7.0	1
RXJ1347	0.451	13 47 31.0	−11 45 11.0	Mar 03	202	6.7	4
A1835	0.25	14 01 02.2	+02 52 43.0	Apr 96	577	19.2	2
A2204	0.152	16 32 47.0	+05 34 33.0	Mar 03	449	15.0	2
A2261	0.22	17 22 27.6	+32 07 37.1	Mar 99	133	4.4	2
A2390	0.23	21 53 36.7	+17 41 43.7	Nov 00	128	4.3	2
″				Dec 02	195	6.5	1
A2390				Totals	323	10.8	

References. — (1) Gioia & Luppino [43]; (2) Ebeling et al. [35]; (3) Ebeling et al. [33]; (4) Schindler et al. [94]

[a]Units of RA are hours, minutes and seconds and units of declination are degrees, arcminutes and arcseconds

[b]The total number of two minute scans used in the data analysis of this cluster.

Chapter 5

Data Reduction and Analysis

Each cluster data set typically comprises several hundred drift scans, as summarized in Table 4.1. Once the data have been despiked, binned and calibrated, we need to extract the SZ signal from the data, and at the same time, obtain an accurate estimate of the uncertainty. For most observing conditions atmospheric emission dominates the emission from our source. Under typical conditions the Noise Equivalent Flux Density (NEFD) for the 145 GHz channel, which is least affected by the atmosphere, is ~ 70 mJy s$^{1/2}$ at the signal frequencies of interest, while the signals we are trying to measure are ~ 40 mJy. The higher frequency channels are progressively worse. In order to improve our signal/noise, we make use of our ability to simultaneously measure the sum of the SZ signal and the atmosphere at three different frequencies. The different temporal and spectral behavior of the atmosphere, compared to the SZ signal of interest, allows us to clean the data and significantly improve the sensitivity of our measurements. This method is based on that of [71], but here we have expanded the explanation contained in his paper with particular emphasis put on understanding the statistics.

5.1 Raw Data Processing

The first step in the data analysis is to remove cosmic ray spikes by carrying out a point by point differentiation of data from a single scan and looking for large ($> 4\sigma$)

deviations from the noise. With a knowledge of the time constant of the bolometer and the height of the spike, we can make a conservative estimate of how much data is contaminated and exclude that data from our analysis. To account for the effect of the bolometer time-constant, which is ≤ 100 ms, we flag a region 100 ms $\times \ln(V_m/\sigma)$ before, and 250 ms $\times \ln(V_m/\sigma)$ after the spike's maximum where V_m is the height of the spike. The data are then combined into 3 second bins each containing 21 samples and covering a region equal to $0\overset{\prime}{.}75 \cos\delta$ on the sky. Bins with 11 or more contaminated samples are excluded from further analysis. Less than 1% of the data are discarded due to cosmic ray contamination.

5.2 SZ Model

A model for the expected spatial distribution of the SZ signal in each scan is obtained by convolving a beam map of a planetary calibrator with the modelled opacity of the cluster. Beam shapes are measured by performing raster scans of a planetary calibrator and recording the voltage response of the detectors, $V_k(\theta, \phi)$ where θ is measured in the direction of RA and ϕ in the direction of declination. We approximate the electron density of the cluster with a spherically-symmetric isothermal β model [14, 15]:

$$n_e(r) = n_{e0}\left[1 + \frac{r^2}{r_c^2}\right]^{-3\beta/2} \tag{5.1}$$

where r is distance from the cluster center, and β and r_c are parameters of the model. By integrating n_e along the line of sight, the cluster optical depth:

$$\tau(\theta, \phi) = \tau_0\left[1 + \frac{(\theta^2 + \phi^2)}{\theta_c^2}\right]^{(1-3\beta)/2} \tag{5.2}$$

is obtained, where linear distance r has been replaced with angles on the sky, θ and ϕ. The model parameters of the intra-cluster gas, β and θ_c, for each cluster are taken from the literature and are listed in Table 5.1 with associated references. We can now calculate a spatial model, $m_k(\theta)$, for each cluster:

$$m_k(\theta) = \int\int \frac{V_k(\theta', \phi')}{V_{peak}} \frac{\tau(\theta' - \theta, \phi')}{\tau_0} d\theta' d\phi' \tag{5.3}$$

that has units of steradians, and is calculated at $0'.05 \times cos\delta$ intervals for a given offset, θ, in right ascension from the cluster center. We calculate our SZ model by multiplying the source model by thermal and kinematic band-averaged spectral factors given by:

$$T_k = I_0 \times \frac{m_e c^2}{kT_e} \times \frac{\int \Psi(x, T_e) \times f_k(x) dx}{\int f_k(x) dx} \tag{5.4}$$

and

$$K_k = -I_0 \times \frac{m_e c^2}{kT_e} \times \frac{\hat{\mathbf{n}}_v \cdot \hat{\mathbf{l}}}{c} \times \frac{\int h(x, T_e) \times f_k(x) dx}{\int f_k(x) dx} \tag{5.5}$$

where the spectral functions $\Psi(x, T_e)$ and $h(x, T_e)$ were previously defined in Chapter 2, and $f_k(x)$ is the spectral response of channel k. The vector $\hat{\mathbf{n}}_v$ is a unit vector in the direction of the cluster peculiar velocity. The quantities $T_k \times m_k(\theta)$ and $K_k \times m_k(\theta)$ are then the SZ models for the expected responses of frequency band k to a scan across a cluster of unity central Comptonization, y_0, with a radial component to the peculiar velocity, v_p, of $1\,\mathrm{km\,s^{-1}}$. The calculated SZ model is then combined into $0'.75 \times \cos\delta$ bins to match the binned SuZIE II data, so that we define $T_k \times m_k(\theta_i)$ as the thermal SZ model in channel k for the right ascension offset θ of bin number i.

5.3 Removal of Residual Atmospheric Signal

There are two sources of residual atmospheric noise in our data, with different temporal spectra. The first is incomplete subtraction of the signal that is common to each beam because of the finite common mode rejection ratio (CMRR) of the electronic differencing. This effect is minimized by slightly altering the bias, and thus the responsivity, of one of the two detectors that form a difference. This trimming process is carried out at the beginning of an observing campaign and is usually left unchanged throughout the observations. The second is a fundamental limitation introduced by the fact that the two beams being differenced pass through slightly different columns

Table 5.1. IC gas temperatures and β model parameters

Cluster	kT_e[a] (keV)	kT_e[b] (keV)	β	θ_c (arcsec)	CF or NCF	Ref.
A520	$8.33^{+0.46}_{-0.40}$	···	$0.844^{+0.040}_{-0.040}$	$123.3^{+8.0}_{-8.0}$	NCF	1;2;2
A545	$5.50^{+6.2}_{-1.1}$	···	0.82[c]	115.5[c]	NCF	3;4;4
A697	$9.8^{+0.7}_{-0.7}$	···	$0.540^{+0.045}_{-0.035}$	$37.8^{+5.6}_{-4.0}$	NCF	2;2;2
A773	$9.29^{+0.41}_{-0.36}$	···	$0.597^{+0.064}_{-0.032}$	$45.0^{+7.0}_{-5.0}$	NCF	1;2;2
MS1054	$7.8^{+0.6}_{-0.6}$	···	$1.39^{+0.14}_{-0.14}$	67.7[c]	NCF	5;5;5
RXJ1347	$9.3^{+0.7}_{-0.6}$	$14.1^{+0.9}_{-0.9}$	$0.604^{+0.011}_{-0.012}$	$9.0^{+0.5}_{-0.5}$	CF	6;5;2;2
A2204	$7.4^{+0.30}_{-0.28}$	$9.2^{+2.5}_{-1.1}$	0.66[c]	34.7[c]	CF	1;1;4;4
A2390	$10.13^{+1.22}_{-0.99}$	$11.5^{+1.5}_{-1.6}$	0.67[c]	52.0[c]	CF	1;7;4;4
A2261	$8.82^{+0.37}_{-0.32}$	$10.9^{+5.9}_{-2.2}$	$0.516^{+0.014}_{-0.013}$	$15.7^{+1.2}_{-1.1}$	CF	1;1;2;2
Zw3146	$6.41^{+0.26}_{-0.25}$	$11.3^{+5.8}_{-2.7}$	0.74[c]	13.0[c]	CF	1;1;4;4
A1835	$8.21^{0.19}_{-0.17}$	$8.2^{+0.4}_{-0.4}$	$0.595^{+0.007}_{-0.005}$	$12.2^{+0.6}_{-0.5}$	CF	1;8;2;2
Cl0016	$7.55^{+0.72}_{-0.58}$	···	$0.749^{+0.024}_{-0.018}$	$42.3^{+2.4}_{-2.0}$	NCF	9;2;2
MS0451	$10.4^{+1.0}_{-0.8}$	···	$0.806^{+0.052}_{-0.043}$	$34.7^{+3.9}_{-3.5}$	NCF	10;2;2
A1689	$9.66^{+0.22}_{-0.20}$	$10.0^{+1.2}_{-0.8}$	$0.609^{+0.005}_{-0.005}$	$26.6^{+0.7}_{-0.7}$	CF	1;1;2;2
A2163	$12.2^{+1.1}_{-0.7}$	···	$0.674^{+0.011}_{-0.008}$	$87.5^{+2.5}_{-2.0}$	NCF	11;2;2

References. — (1) [1], (2) [88], (3) [26], (4) [36], (5) [105], (6) [94], (7) [3], (8) [82], (9) [55], (10) [30], (11) [66]

[a]The X-ray emission weighted temperature.

[b]The cooling flow corrected X-ray emission weighted temperature.

[c]No confidence intervals were given for these parameters. It is assumed their uncertainty is comparable to the other clusters in our sample.

of atmosphere; consequently there is a percentage of atmospheric emission that cannot be removed by differencing. While both signals originate from the atmosphere, their temporal properties are quite different and are accordingly removed differently in our analysis. In what follows we denote each frequency channel with the subscript k, each scan with the subscript j and each bin within a scan with a subscript i. In this way the difference and single channel signals at 145 GHz from scan j and bin i are D_{3ji} and S_{3ji}.

The residual common mode signal from the atmosphere in the difference channel D_{kji} is modelled as proportional to the signal from the corresponding single channel. We define our common mode atmospheric template, C_{kji}, as $C_{kji} \equiv S_{kji}$. Because the single channels contain a small proportion of SZ signal, there is potential to introduce a systematic error by removing true SZ signal. However, the effect is estimated at less than 2% (see section 6.3.2).

To model the residual differential signal from the atmosphere we construct a linear combination of the three differential channels in a single row which contains no thermal or kinematic SZ signal. For the on-source row we define our differential atmospheric template, A_{ji} as:

$$A_{ji} = \alpha D_{1ji} + \gamma D_{2ji} + D_{3ji} \tag{5.6}$$

with a similar definition for the off-source row. The coefficients α and γ are chosen to minimize the residual SZ flux in A_{ji}. We describe the construction of this template in detail in appendix A and list the values of α and γ used for the on-source row observation of each cluster in Table 5.2. Removing atmospheric signal in this way significantly increases our sensitivity; however it has the disadvantage of introducing a correlation between different frequency channels which must be accounted for. Also this model is dependant on the cluster parameters used, and is subject to uncertainties in the temperature, and spatial distribution of, the cluster gas. We quantify the uncertainty in the final result that this produces in section 6.3.2.

In addition to the atmospheric signals, we also remove a slope, b_{kj}, and a constant,

Table 5.2. Differential Atmospheric Template Factors

Cluster	α	γ
A697[a]	0.6848	-1.4374
A773[a]	0.6861	-1.4380
RXJ1347[a]	0.6703	-1.3773
A2204[a]	0.6819	-1.4103
A520[a]	0.6785	-1.4426
A2390[a](Nov00)	0.6563	-1.4721
A2390[a](Dec02)	0.6676	-1.4191
Zw3146[a]	0.6428	-1.3808
A2261[a]	0.6366	-1.4490
A545[a]	0.6612	-1.4493
MS1054[a]	0.7464	-1.5391
MS0451[a](Nov97)	0.6770	-1.3933
MS0451[a](Nov00)	0.6449	-1.4286
...	...	...
A1835[b]	1.2133	-2.1745
Cl0016[b]	1.2353	-2.2331
MS0451[b](Nov96)	1.2246	-2.2076

[a]High frequency channel was 355 GHz

[b]High frequency channel was 273 GHz

a_{kj}, such that our "cleaned" signal is then:

$$X_{kji} = D_{kji} - a_{kj} - ib_{kj} - (e_{kj} \times C_{kji}) - (f_{kj} \times A_{ji}) \tag{5.7}$$

where we calculate the best-fit parameters by minimizing $\sum_i X_{kji}^2$. We note that since we remove a best-fit constant offset this implies $\sum_i X_{kji} \approx 0$.

5.4 Determination of the Cluster Location in the Scan

Variations in the location of the cluster center with respect to the nominal pointing center defined in Figure 4.1 can be caused by differences in the location of the X-ray and SZ peaks, and by CSO pointing uncertainties. The latter are expected to be less than $10''$. To determine the true cluster location we first co-add all of the scans for a single cluster, as described below, then fit the data with the SZ model described above, allowing the source position to vary. Note we are only able to constrain the location in right ascension; the effects of pointing uncertainties are discussed further in section 6.3.3.

Following [51], we define X_{ki}, the coadded signal at each location, i, as:

$$X_{ki} = \frac{\sum_{j=1}^{N_s} X_{kji}/\mathrm{RMS}_{kj}^2}{\sum_{j=1}^{N_s} 1/\mathrm{RMS}_{kj}^2} \tag{5.8}$$

where N_s is the number of scans, and each scan is weighted according to its root-mean-square (RMS) residual defined as:

$$\mathrm{RMS}_{kj}^2 = \frac{\sum_{i=1}^{N_b} X_{kji}^2}{N_b - 1} \tag{5.9}$$

where N_b is the number of bins in a single scan. The uncertainty of each bin in the co-added scan, is estimated from the dispersion about the mean value weighted by the RMS_{kj} of each scan,

$$\sigma_{ki} = \sqrt{\frac{\sum_{j=1}^{N_s} (X_{ki} - X_{kji})^2/\mathrm{RMS}_{kj}^2}{(N_s - 1)\sum_{j=1}^{N_s} 1/\mathrm{RMS}_{kj}^2}} \tag{5.10}$$

This expression provides an unbiased estimate of the uncertainty associated with each bin.

The on-source row at $\nu \sim 145\,\mathrm{GHz}$ ($k = 3$) provides the highest sensitivity measurement of the cluster intensity, and so it alone is used to fix the cluster location. The co-added data are fit to a model that includes an offset, a, a slope, b, and the SZ model, where the cluster location, $\mathrm{RA}_{\mathrm{offset}}$ and the central comptonization, y_0, are allowed to vary. For each set of parameters, we can define χ^2 as:

$$\chi^2 = \sum_{i=1}^{N_b} \frac{[X_{3i} - \{y_0 \times T_3 \times m_3(\theta_i - \mathrm{RA}_{\mathrm{offset}})\} - a - ib]^2}{\sigma_{3i}^2} \tag{5.11}$$

To determine the best-fit model all four parameters (a, b, y_0, and the $\mathrm{RA}_{\mathrm{offset}}$) are allowed to vary while the χ^2 is minimized. The linear baseline is allowed to vary to ensure that the removal of a linear baseline in equation 5.7 does not remove any SZ signal. Here we are making the assumption that the measured SZ emission in the 145 GHz band is entirely thermal. We are not yet concerned with distinguishing thermal from kinematic SZ emission because at this stage our goal is only to fit the location of the cluster. The cluster locations determined in this way are listed in Table 5.3. Most of the clusters lie within $30''$ of the nominal pointing center, and in most cases the cluster is located at the pointing center, within our experimental uncertainty. However both clusters observed during December 2002, A520 and A2390, are significantly off center. The measured right ascension offset for A520 was 103^{+51}_{-53}" and for A2390 was -60^{+28}_{-29}". Because the offsets have a different sign it is unlikely there was a systematic offset in our pointing consistent across the sky. We now discuss the apparent discrepancy of the cluster location of A520 and A2390 individually.

In Table 5.4 we give the location of A520 from two different X-ray measurements and from our SuZIE observation. The X-ray measurements are described in Ebeling

Table 5.3. Right Ascension Offset

Cluster	Date	Δ RA (arcsec)
A697	Mar03	-25^{+16}_{-17}
A773	Mar03	7^{+25}_{-27}
RXJ1347	Mar03	15^{+12}_{-12}
A2204	Mar03	3^{+21}_{-20}
A520	Dec02	103^{+51}_{-53}
Zw3146	Nov00	11^{+31}_{-31}
A2261	Mar99	6^{+19}_{-20}
Cl0016	Nov96	6^{+35}_{-37}
A1835	Apr96	28^{+16}_{-15}
A2390	Nov00	-5^{+18}_{-19}
···	Dec02	-60^{+28}_{-29}
MS0451	Nov96	-16^{+26}_{-24}
···	Nov97	12^{+10}_{-11}
···	Nov00	-21^{+21}_{-19}

et al. [35] and Allen [2], with the respective locations calculated from the X-ray centroid. No uncertainties were given for either X-ray measurement, however the typical pointing uncertainties of the PSPC is $\sim 25''$ and for the HRI is $\sim 10''$. The pointing center for the SuZIE observation of A520 was defined as the X-ray centroid for the PSPC. It can be seen in Table 5.4 that the X-ray centroid from the HRI is more consistent with the location measured by SuZIE than the PSPC observation which had defined our pointing center. In addition, an observation of A520 by the OVRO interferometer measured a cluster location consistent with the location measured by SuZIE [89]. This could suggest that the X-ray and SZ centroid may not be equivalent for this cluster. For these reasons, we believe the pointing offset observed by the SuZIE observation of A520 is a real effect and consistent with the true SZ center.

In Table 5.4 we give the location of A2390 based on two different X-ray measurements and two different SuZIE observations. The X-ray references for A2390 are the same as for A520, and determine the cluster location from the position of the X-ray centroid. The X-ray centroid measured from the PSPC and from the HRI agree very well. Because the HRI has a much smaller pointing uncertainty than the PSPC, see the preceding paragraph, we will only consider the more certain HRI coordinates. The SuZIE observation from November 2000 measured a best-fit location nearly coincident with the HRI X-ray centroid, while the SuZIE observation from December 2002 measured a best-fit location $\sim$ 60" west. The 68% confidence intervals do not overlap between the measurements, however they are only separated by $\sim$ 9". Because we had not previously observed any pointing offset and A2390 had been successfully observed with SuZIE before in November 2000, we analyze the A2390 measurements from December 2002 assuming zero offset from the nominal pointing center. This adjustment changes the calculated central Comptonization of A2390 by only $\sim$3% when considering the combined results of the November 2000 and December 2002 observing runs which is calculated in section 5.5.

For several reasons we use the coadded method *only* to determine the cluster location, not to determine y_0 and v_p. These reasons include one pointed out in [51], which is that if the source contributes significantly to the variance of each scan, then the RMS given by equation (5.9) will be biased. This does not affect the determination

Table 5.4. Cluster Positions

Cluster	Instrument	R.A.[a] (J2000)	Decl.[a] (J2000)	Ref.
A520	PSPC	04 54 07.4	+02 55 12.1	1
⋯	HRI	04 54 10.1	+02 55 27.0	2
⋯	BIMA	04 54 09.3	+02 54 42.5	3
⋯	OVRO	04 54 12.7	+02 55 24.0	3
⋯	SuZIE	04 54 $14.3^{+3.4}_{-3.6}$	⋯	4
⋯	⋯	⋯	⋯	⋯
A2390	PSPC	21 53 36.7	+17 41 31.2	1
⋯	HRI	21 53 36.5	+17 41 45.0	2
⋯	SuZIE	21 53 $36.4^{+1.1}_{-1.2}$	⋯	5
⋯	SuZIE	21 53 $32.9^{+1.7}_{-1.9}$	⋯	4

References. — (1) Ebeling et al. [35](2) Allen [2] (3)Reese [89] (4) Measured in 2002 December by SuZIE II (5) Measured in 2000 November by SuZIE II

[a]Units of RA are hours, minutes and seconds and units of declination are degrees, arcminutes and arcseconds

of the cluster location. Although we could correct this bias by subtracting the best-fit model from the data prior to estimating the RMS, in an iterative fashion, there is another more serious complication to the coadded data – that of correlations between the bins in the co-added scan produced by the presence of residual atmospheric noise in the data, and by the atmospheric removal process itself. Neither the bias of the RMS or the correlations in the coadded scan affect the determination of the cluster center, but they do need to be correctly accounted for in the determination of the SZ parameters.

5.5 Individual Scan Fits for Comptonization and Peculiar Velocity

To generate an unbiased estimate of the SZ parameters we fit for comptonization and peculiar velocity in all three frequency channels simultaneously, using the cluster central position determined from the coadded data. Following [51, 52] and [71], we fit the data on a scan-by-scan basis to estimate the uncertainty in the fitted parameters, because we expect no scan-to-scan correlation in the noise. While unbiased and producing satisfactory results, this method is not formally optimal. An alternative would be to calculate, and then invert, the noise covariance matrix for the data set. However, because of the high degree of correlation in the raw data, this technique has not been found to yield stable solutions.

We begin again with the de-spiked, binned, calibrated data defined in section 5.1. We fit the data vector from each scan with a slope, a constant, the model for residual common-mode and differential atmospheric signals and an SZ model with thermal and kinematic components. Within each scan we allow the slope, constant, and atmospheric coefficients to vary between frequency channels, but we fix the comptonization and peculiar velocity to be the same at each frequency. The residual signal left after removal of all modelled sources of signal is then:

$$R_{kji} \;=\; D_{kji} - a_{kj} - ib_{kj} - (e_{kj} \times C_{kji}) - (f_{kj} \times A_{ji}) - y_{0j} T_k m_k(\theta_i - \mathrm{RA}_{\mathrm{offset}})$$

$$-(y_0 v_p)_j K_k m_k(\theta_i - \mathrm{RA}_{\mathrm{offset}}) \tag{5.12}$$

where a_{kj} are the offset terms, b_{kj} are the slope terms, and e_{kj} (f_{kj}) are the coefficients that are proportional to the common-mode (differential-mode) atmospheric signal in frequency channels $k = 1, 2, 3$. The SZ-model parameters y_{0j} and $(y_0 v_p)_j$ are proportional to the magnitude of the thermal and kinematic components in each frequency channel. The common-mode and differential atmospheric templates, C_{kji} and A_{ji}, are constructed using the method described in section 5.3. The thermal and kinematic SZ model templates, $T_k m_k(\theta_i - \mathrm{RA}_{\mathrm{offset}})$ and $K_k m_k(\theta_i - \mathrm{RA}_{\mathrm{offset}})$, are described in section 5.2.

The best-fit model of scan j is then determined by minimizing the χ^2, which is defined as:

$$\chi_j^2 = \sum_{k=1}^{3} \frac{\sum_{i=1}^{N_b} R_{kji}^2}{\mathrm{RMS}_{kj}^2} \tag{5.13}$$

where

$$\mathrm{RMS}_{kj}^2 = \frac{1}{N_b - 1} \sum_{i}^{N_b} (R_{kji}^{best})^2 \tag{5.14}$$

is the mean squared of the residual signal after removal of the best-fit model. This has to be an iterative process because we cannot correctly calculate the best fit model and its associated uncertainty until we know the RMS of the residual signal with the best-fit model removed. As a first guess we use the RMS of the raw data, and upon each iteration afterwards calculate the RMS with the best-fit model removed from the previous minimization. This process is continued until the best-fit values for y_{0j} and $(y_0 v_p)_j$ vary by less than one part in a million, a condition usually met by the third iteration. We determine the uncertainty of y_{0j} and $(y_0 v_p)_j$, σ_{yj} and $\sigma_{(yv_p)j}$, using the standard definition from a general linear least squares fit [see 86, for example].

5.6 Likelihood Analysis of Individual Scan Fits

From the individual scan fits for comptonization and peculiar velocity we next define a symmetric 2 by 2 covariance matrix, $\mathbf{\Sigma}$, defined by

Table 5.5. Summary of SuZIE Multi-frequency Results

Cluster	Date	$y_0 \times 10^4$	v_{pec} (km s^{-1})
A697	Mar03	$4.46^{+0.98}_{-0.98}$	-1625^{+1075}_{-825}
A773	Mar03	$3.93^{+1.88}_{-2.15}$	-1175^{+2875}_{-1625}
RXJ1347	Mar03	$9.92^{+2.62}_{-2.65}$	0.0^{+1225}_{-850}
A2204	Mar03	$2.29^{+0.70}_{-0.72}$	-1100^{+1100}_{-775}
A520	Dec02	$2.00^{+0.70}_{-0.73}$	-1700^{+1450}_{-1375}
A2390	Nov00/Dec02	$3.56^{+0.52}_{-0.51}$	-175^{+1050}_{-900}
Zw3146	Nov00	$3.62^{+1.83}_{-2.52}$	-400^{+3700}_{-1925}
A2261	Mar99	$7.41^{+1.95}_{-1.98}$	-1575^{+1500}_{-975}
MS0451	Nov96/97/00	$2.84^{+0.52}_{-0.52}$	$+800^{+1525}_{-1125}$
Cl0016	Nov96	$3.27^{+1.45}_{-2.86}$	-4100^{+2650}_{-1625}
A1835	Apr96	$7.66^{+1.64}_{-1.66}$	-175^{+1675}_{-1275}
A1689[a]	Apr94/May94	$3.43^{+0.59}_{-0.59}$	$+170^{+805}_{-600}$
A2163[a]	Apr93/May93	$3.62^{+0.49}_{-0.49}$	$+490^{+1310}_{-790}$

[a]These clusters results are taken from Holzapfel et al. [52], and were not re-analyzed using the method described in section 5.6. However, we include them to give a complete listing of clusters with multi-frequency SuZIE results and therefore constrained peculiar velocities.

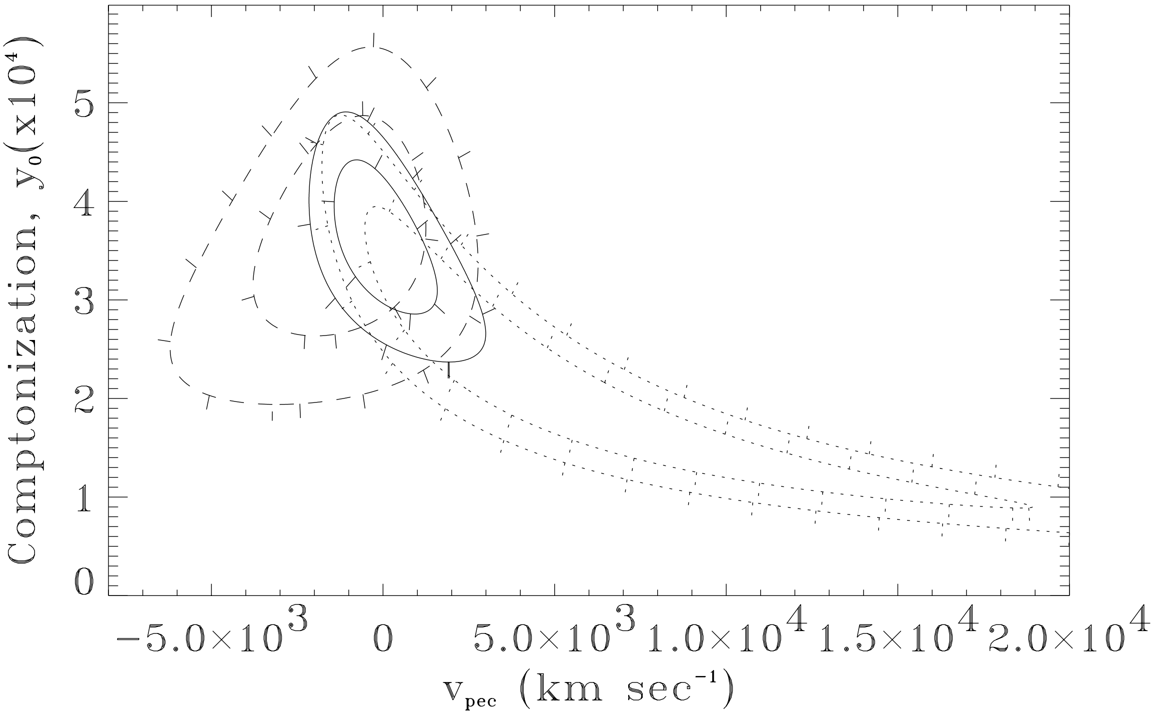

Fig. 5.1.— The two-dimensional likelihood of the measurements of A2390 in November 2000, December 2002, and then the combined likelihood from both observations. For each set of data the 68.3% and 95.4% confidence regions are shown for peak Comptonization and peculiar velocity. The dotted contours are from the November 2000 data, the dashed contours are from the December 2002 data, and the solid contours are from the combined likelihoods.

$$\mathbf{\Sigma}_{11} = \frac{1}{N_s - 1} \frac{\sum_j^{N_s} (y_{0j} - < y_0 >)^2 / \sigma_{yj}^4}{\sum_j^{N_s} 1/\sigma_{yj}^4} \tag{5.15}$$

$$\mathbf{\Sigma}_{22} = \frac{1}{N_s - 1} \frac{\sum_j^{N_s} ((y_0 v_p)_j - < y_0 v_p >)^2 / \sigma_{(y_0 v_p)j}^4}{\sum_j^{N_s} 1/\sigma_{(y_0 v_p)j}^4} \tag{5.16}$$

$$\mathbf{\Sigma}_{mn} = \frac{1}{N_s - 1} \frac{\sum_j^{N_s} [(y_0 v_p)_j - < y_0 v_p >][y_{0j} - < y_0 >]/[\sigma_{yj}^2 \sigma_{(yv_p)j}^2]}{\sum_j^{N_s} 1/[\sigma_{yj}^2 \sigma_{(yv_p)j}^2]} \quad \text{for } m \neq n \tag{5.17}$$

where y_{0j}, $(y_0 v_p)_j$, σ_{yj} and $\sigma_{(yv_p)j}$ are determined for scan j from the minimization of the χ_j^2 defined in equation (5.13). The quantities $< y_0 >$ and $< y_0 v_p >$ are weighted averages of the individual scan fits for the thermal and kinematic SZ components, and are defined as:

$$< y_0 > = \frac{\sum_j^{N_s} y_{0j}/\sigma_{yj}^2}{\sum_j^{N_s} 1/\sigma_{yj}^2} \tag{5.18}$$

$$< y_0 v_p > = \frac{\sum_j^{N_s} (y_0 v_p)_j / \sigma_{(y_0 v_p)j}^2}{\sum_j^{N_s} 1/\sigma_{(yv_p)j}^2} \tag{5.19}$$

These weighted averages are unbiased estimators of the optical depth and peculiar velocity. Having calculated the covariance matrix we define the likelihood function for our model parameters v_p and y_0 as:

$$L(v_p, y_0) = \frac{1}{(2\pi)|\mathbf{\Sigma}|^{1/2}} \exp\left[-\frac{1}{2} \begin{pmatrix} < y_0 > - y_0 \\ < y_0 v_p > - y_0 \times v_p \end{pmatrix}^T \mathbf{\Sigma}^{-1} \begin{pmatrix} < y_0 > - y_0 \\ < y_0 v_p > - y_0 \times v_p \end{pmatrix} \right] \tag{5.20}$$

The likelihood is calculated over a large grid in parameter space with a resolution of $\Delta v_p = 25\,\mathrm{km\,s^{-1}}$ and $\Delta y = 10^{-6}$. The 1-σ uncertainty on each parameter is then determined using the standard method of marginalizing the likelihood function over the other parameter. The results for each cluster are shown in Table 5.5.

Of the measurements presented in this thesis, only MS0451 and A2390 had been observed on different observing runs with SuZIE. It is worthwhile to compare the December 2002 results for A2390 to the previous observation from November 2000 for a systematic check of any time-dependent or observing-dependent errors. In Figure 5.1 we plot the 2-d likelihoods from both observing runs, and their product. It is evident that the overall constraints from the November 2000 data are much weaker. Due to the low sensitivity of this data, there is a very weak constraint on the peculiar velocity and a large degeneracy towards an increasing peculiar velocity and a decreasing Comptonization. The degeneracy between a decreasing Comptonization and an increasing peculiar velocity is a general characteristic of the likelihood function of each cluster. The 68% confidence regions do overlap between the two data sets, and we consider them in good agreement. The combined likelihood for A2390 is the product of the likelihoods from the November 2000 and December 2002 observing runs, $L(v_p, y_0) = L(v_p, y_0)_{\mathrm{Nov00}} \times L(v_p, y_0)_{\mathrm{Dec02}}$. For A2390, the value of y_0 given in Table 5.5 is calculated from marginalizing the combined likelihood function over peculiar velocity.

5.7 Spectral Plots for Each Cluster

Figure 5.2 plots the best-fit SZ spectrum for each cluster with the SuZIE II-determined intensities at each of our three frequencies overlaid. Note, *these plots are for display purposes only to verify visually that we do indeed measure an SZ-type spectrum.* Although the values of the intensity at each frequency are correct, the uncertainties are strongly correlated. Consequently these intensity measurements cannot be directly fitted to determine SZ, and other, parameters. This is why we use the full scan-by-scan analysis described in the previous section.

In order to calculate the points shown in Figure 5.2 we calculate a new coadd of the data at each frequency after cleaning atmospheric noise from the data. We define the cleaned data set, Y_{kji}, as:

$$Y_{kji} = D_{kji} - a_{kj} - ib_{kj} - (e_{kj} \times C_{kji}) - (f_{kj} \times A_{ji}) \tag{5.21}$$

with the best-fit parameters for a_{kj}, b_{kj}, e_{kj}, and f_{kj} determined from equation (5.13).

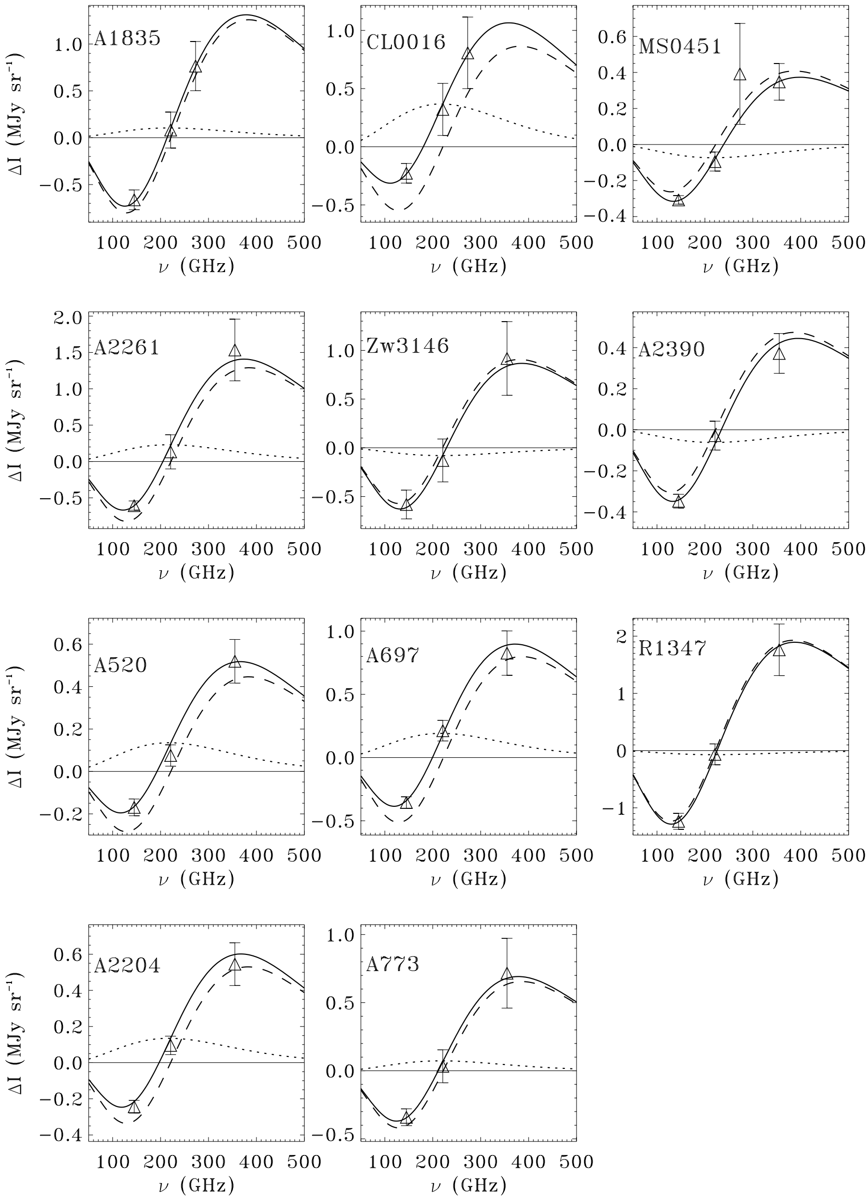

Fig. 5.2.— The measured SZ spectrum for each cluster detected by SuZIE II. In each plot the solid line is the best-fit SZ model, the dashed line is the thermal component of the SZ effect and the dotted line is the kinematic component of the SZ effect.

This cleaned data set can now be co-added using the residual RMS defined in equation (5.14) as a weight, such that:

$$Y_{ki} = \frac{\sum_{j=1}^{N_s} Y_{kji}/\mathrm{RMS}_{kj}^2}{\sum_{j=1}^{N_s} 1/\mathrm{RMS}_{kj}^2} \tag{5.22}$$

Unlike equation (5.9) used in section 5.4, this calculation of the RMS is not biased by any contribution from the SZ source. The uncertainty of each co-added bin, σ_{ki}, is determined from the dispersion about the mean value, Y_{ki}, weighted by the RMS_{kj}^2 of each scan,

$$\sigma_{ki} = \sqrt{\frac{\sum_{j=1}^{N_s} (Y_{ki} - Y_{kji})^2/\mathrm{RMS}_{kj}^2}{(N_s - 1)\sum_{j=1}^{N_s} 1/\mathrm{RMS}_{kj}^2}} \tag{5.23}$$

The best-fit central intensity, I_k, for each frequency band is then found by minimizing the χ_k^2 of the fit to the co-added data, where χ_k^2 is defined as follows:

$$\chi_k^2 = \sum_{i=1}^{N_b} \frac{\left[Y_{ki} - I_k \times m_k(\theta_i - \mathrm{RA_{offset}})\right]^2}{\sigma_{ki}^2} \tag{5.24}$$

We calculate confidence intervals for I_k using a maximum likelihood estimator, $L(I_k) \propto \exp(-\chi_k^2/2)$. In Figure 5.3, we show co-added data scans for the March 2003 observations of RXJ1347 for all three on-source frequency bands. The best fit intensity at each frequency, and the 1-σ error bars are also shown.

In Figure 5.4, we show the spectrum of MS0451 measured during each of the three observing runs, and the averaged spectrum. This figure, and the best fit parameters (determined from the scan-by-scan fitting method) shown in Table 5.5 indicate that there is good consistency between data sets taken many months apart.

In order to demonstrate the value of our atmospheric subtraction procedure, we have repeated our analysis for the MS0451 November 2000 data both with and without atmospheric subtraction. The derived fluxes from the coadded data are shown in Table 5.6. The improvement in the sensitivity, especially at 220 and 355 GHz, is substantial.

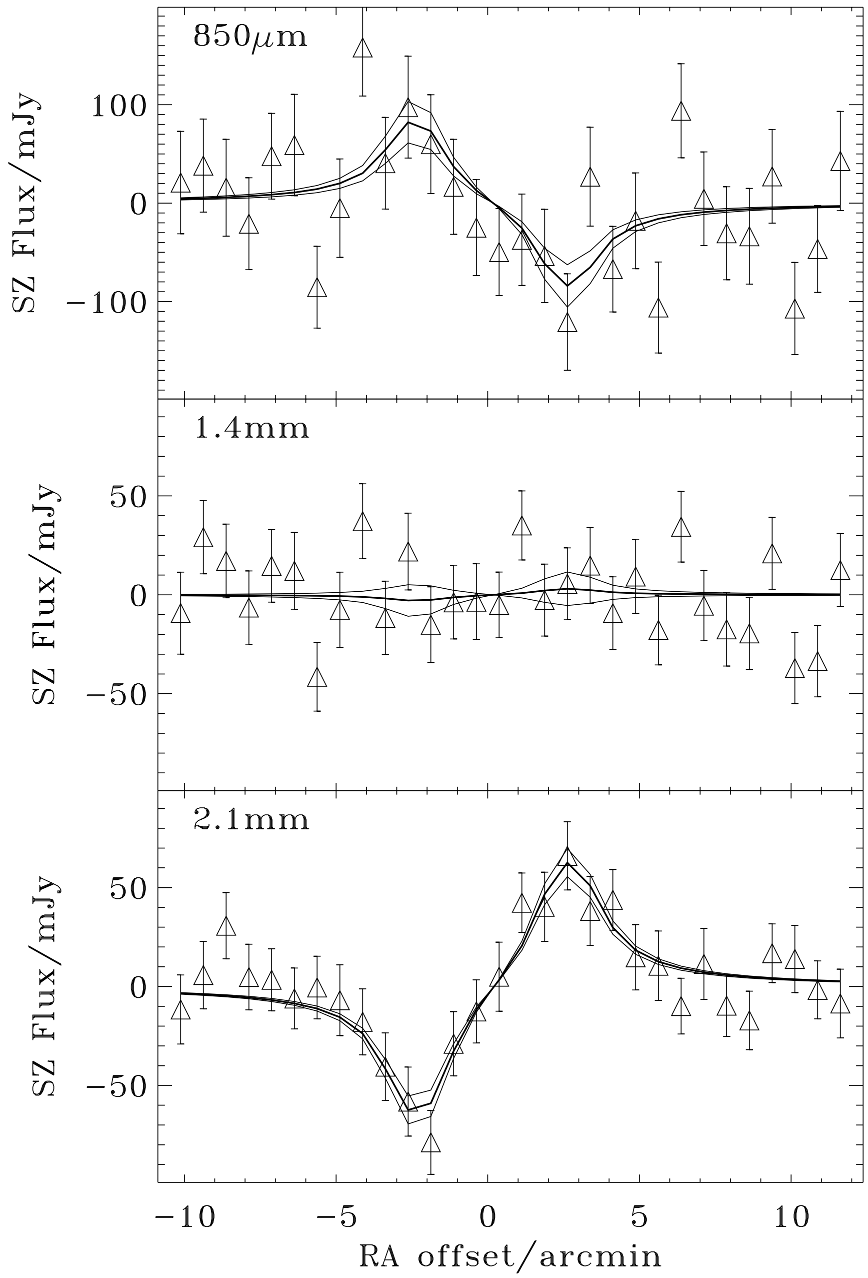

Fig. 5.3.— Co-added scans of RXJ1347 from March 2003 for the on-source row for each of the three SuZIE frequency bands. The heavy line is the best-fit model to the co-added scan, while the lighter lines represent the 1-σ uncertainty to those fits.

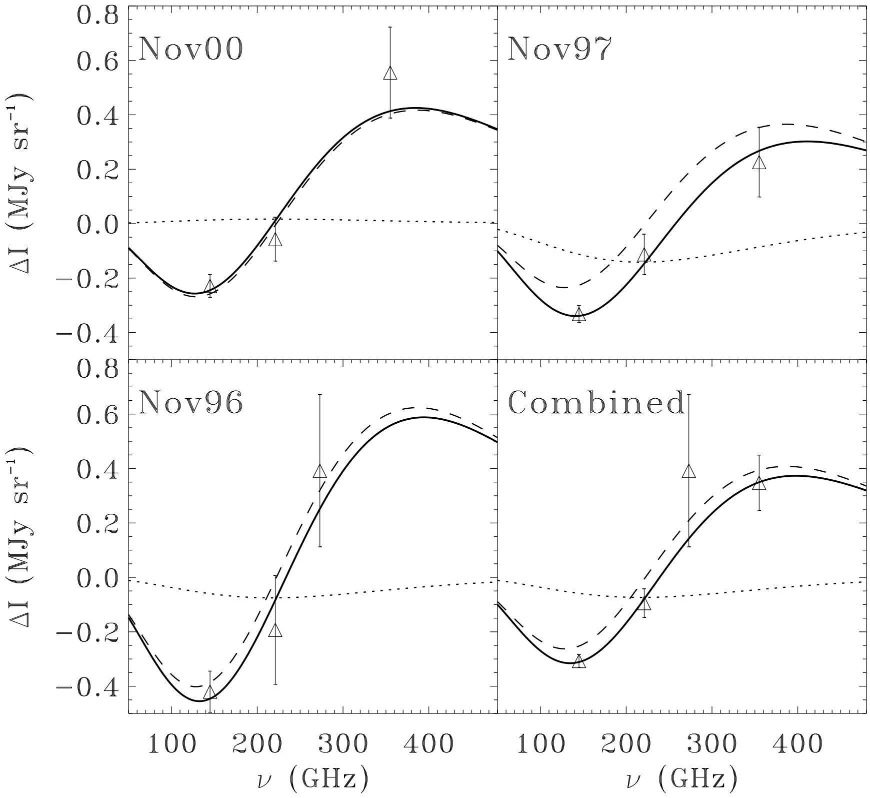

Fig. 5.4.— The measured spectra of MS0451 from each of the three observing runs as well as the combined spectra using the weighted mean of each spectral point. In each plot the solid line is the best-fit SZ model, the dashed line is the thermal component of the SZ effect and the dotted line is the kinematic component of the SZ effect.

Table 5.6. The Effects of Atmospheric Subtraction on Derived Fluxes for MS0451 Nov 2000 Data

Frequency (GHz)	Flux ($\mathrm{MJy\ sr^{-1}}$) With Atm. Subtraction	Without Atm. Subtraction
355	$0.555^{+0.167}_{-0.167}$	$-1.303^{+1.148}_{-1.148}$
221	$-0.057^{+0.081}_{-0.080}$	$-0.389^{+0.171}_{-0.171}$
145	$-0.229^{+0.042}_{-0.042}$	$-0.234^{+0.064}_{-0.064}$

5.8 145 GHz Analysis

Ultimately we wish to compare our results for the central Comptonization to independent single frequency SZ measurements, which by themselves cannot constrain the peculiar velocity. In principle, our multi-frequency results should be an appropriate comparison because they take full account of the shape of the SZ spectrum and should therefore accurately measure Comptonization. However, there are some advantages in considering the 145 GHz data on its own. The 145 GHz channel is the most sensitive of the frequency channels to the SZ thermal effect. Including the higher frequency channels allows one to constrain the peculiar velocity as well as the central Comptonization. However, due to the lower sensitivity of the higher frequency channels and the addition of the peculiar velocity as a free paramater, the overall constraints on the calculated central Comptonization actually decreases with the addition of the higher frequency channels. In addition, the higher frequency channels suffer more confusion from sub-millimeter point sources. We showed in Benson et al. [9] that typical sub-millimeter point sources in our cluster fields have a tendency to bias our peculiar velocity results towards negative values by a factor of several hundred kilometers per second and our central Comptonization results higher by several times 10^{-4}. This effect can be minimized by only analyzing the 145 GHz data because sub-millimeter point sources have spectral energy densities which decrease with frequency. Another concern is that clusters with low sensitivity in the higher frequency channels are often biased to a lower Comptonization due to a degeneracy in the 2-dimensional likelihood, $L(v_p, y_0)$, which biases the marginalized results towards a lower Comptonization and an increasing peculiar velocity. This effect is evident in the likelihood for A2390 from the November 2000 data, see Figure 5.1. For these reasons, it is useful to analyze the cleaned co-added 145 GHz data alone, which will be the subject of this section. For this analysis we include previous SuZIE I measurements given in Holzapfel et al. [52].

5.8.1 Fitting for a Central Comptonization

We calculate a central Comptonization from the co-added 145 GHz data using a method similar to the one used to calculate the intensity points in section 5.7 except

Table 5.7. SuZIE 145 GHz Central Comptonization Results

Cluster	$y_0 \times 10^4$
A697	$3.55^{+0.57}_{-0.53}$
A773	$3.37^{+0.73}_{-0.66}$
RXJ1347	$12.31^{+1.89}_{-1.72}$
A2204	$2.44^{+0.43}_{-0.39}$
A520	$1.65^{+0.45}_{-0.41}$
A2390	$3.57^{+0.42}_{-0.42}$
Zw3146	$5.65^{+1.78}_{-1.58}$
A2261	$6.01^{+0.93}_{-0.81}$
MS0451	$3.12^{+0.30}_{-0.29}$
Cl0016	$2.31^{+0.93}_{-0.90}$
A1835	$6.70^{+1.40}_{-1.24}$
A1689	$5.20^{+0.58}_{-0.52}$
A2163	$3.25^{+0.40}_{-0.39}$
A545[a]	$1.26^{+0.39}_{-0.30}$
MS1054[a]	$3.87^{+1.19}_{-1.12}$

[a]These clusters were observed by SuZIE and detected at 145 GHz but lacked the sensitivity at 221 and 355 GHz to constrain their peculiar velocities.

here we are solving for a central Comptonization instead. For our data, we use the co-added scan from the on-source row at 145 GHz, Y_{3i}, which was defined in equation 5.22. From Y_{3i} we subtract a SZ model which includes a peculiar velocity, v_p, and a central Comptonization, y_0, to calculate a χ^2 which we define as

$$\chi^2(v_p, y_0) = \sum_{i=1}^{N_b} \frac{[Y_{3i} - y_0 m_3(\theta_i - \mathrm{RA}_{\mathrm{offset}})(T_3 + v_p K_3)]^2}{\sigma_{3i}^2} \tag{5.25}$$

where T_3, K_3, and $m_3(\theta)$ are defined in section 5.2. Under the assumption of Gaussian errors on Y_{3i}, this χ^2 is related to the likelihood via $L(v_p, y_0) \propto \exp(-\chi^2(v_p, y_0)/2)$. In this work we are interested only in the central Comptonization, and so marginalize over the peculiar velocity. We assume a Gaussian prior on v_p whose likelihood we take to be $\propto \exp(-v_p^2/2\sigma_v^2)$. For these measurements we assume a most-likely peculiar velocity of $v_p = 0$ km s^{-1} and a Gaussian width $\sigma_v = 500$ km s^{-1}. Because the clusters peculiar velocities are expected to be randomly distributed around $v_p = 0$ km s^{-1}, this assumption should not bias these results. We marginalize over peculiar velocity such that our formal probability distribution for the central Comptonization, $P(y_0)$, is defined as

$$P(y_0) = \frac{1}{\sqrt{2\pi\sigma_v^2}} \int L(v_p, y_0) \exp\left(\frac{-v_p^2}{2\sigma_v^2}\right) dv_p \tag{5.26}$$

From $P(y_0)$ we calculate our best-fit central Comptonization and associated 68% confidence region for the thirteen clusters presented in this thesis, and the two clusters from Holzapfel et al. [52]. For a summary of these results see Table 5.7.

If we compare the central Comptonizations calculated from the 145 GHz data, given in Table 5.7, to those calculated from the multi-frequency data, given in Table 5.5, it is clear that the 145 GHz results give better constraints for the central Comptonization. While it may seem counterintuitive that the exclusion of two frequency channels actually increases the constraints on the central Comptonization, this gain occurs because of the way we handle the cluster peculiar velocity in both calculations. For the 145 GHz analysis we placed a Gaussian prior of width 500 km s^{-1} on the peculiar velocity. However, for the multi-frequency analysis in section 5.5, we placed no prior on the peculiar velocity, adding a degree of freedom to the analysis. In fact, the multi-frequency constraints on peculiar velocity are $\sim 1000 - 2000$ km s^{-1} [9, 18], which is less constraining than the prior we used in the 145 GHz analysis. Because the higher frequency channels are also less sensitive to the SZ thermal effect than the 145 GHz channel, the overall effect is that the 145 GHz results more tightly constrain the central Comptonization than the multi-frequency results.

With currently favored cosmological models it is expected that the peculiar velocities of clusters be less than $1000\,\mathrm{km\,s^{-1}}$ [45, 96, 101]. However recent observations show evidence for internal flows as large as $4000\,\mathrm{km\,s^{-1}}$ [32, 68]. Therefore it is expected that the $\sigma_v = 500\,\mathrm{km\,s^{-1}}$ prior is a reasonable estimate of the true width, however larger velocities have not been observationally ruled out. Because the multi-frequency results from SuZIE constrain the peculiar velocity through the measurement of the SZ spectrum, we will consider a broader range of priors on the peculiar velocity when we re-analyze these results in section 7.2. There we will show that broadening this prior to include high peculiar velocities with greater probability does not greatly affect the results. However for the 145 GHz data analysis we only consider the case where $\sigma_v = 500\,\mathrm{km\,s^{-1}}$.

It should be noted that for the clusters from Holzapfel et al. [52], A1689 and A2163, the IC gas model used by Holzapfel et al. [52] differed from those used in Reese et al. [88]. In Table 5.8 we give a summary of the beta models and electron temperatures used in both references. We also give the calculated central Comptonization derived from the SuZIE measurements using the two sets of IC gas models. For the case of A1689 the difference in beta model parameters was significant. This is not surprising considering the gas model used by Holzapfel et al. [52] for A1689 was calculated from an unpublished analysis of a PSPC observation, while the model used by Reese et al. [88] was calculated from a more recent HRI observation. For the A1689 SuZIE results, the model assumed significantly changes the calculated central Comptonization, by $\sim 40\%$. This difference is largely because A1689 is unresolved by SuZIE, and therefore the central Comptonization calculated depends entirely on the assumed IC gas model. To maintain consistency with Reese et al. [88], the central Comptonizations of A1689 and A2163 given in Table 5.7 assume the IC gas model parameters used in Reese et al. [88]. Because all of the clusters observed by SuZIE are unresolved the calculated

Table 5.8. Re-Analysis of SuZIE I Observations

Cluster	kT_e (keV)	β	θ_c (arcsec)	$y_0 \times 10^4$	IC Gas Ref
A1689	9.66	0.609	26.6	$5.20^{+0.58}_{-0.52}$	1
···	8.2	0.78	67.8	$3.67^{+0.40}_{-0.38}$	2
A2163	12.2	0.674	87.5	$3.25^{+0.40}_{-0.39}$	1
···	12.4	0.616	72.0	$3.48^{+0.42}_{-0.42}$	2

References. — (1) Reese et al. [88] (2) Holzapfel et al. [52]

central Comptonization depends sensitively on the assumed IC gas model. This uncertainty will be discussed further in section 6.3.4.

5.8.2 Fitting for the Integrated SZ Flux

In the last section, it was shown that the inferred central Comptonization for A1689 changes significantly depending on the IC gas model assumed. It would be preferable to express our SZ measurements in a way that depends less sensitively on the assumed IC gas model. An alternative observable is the SZ flux integrated over some well-defined area on the sky. In the literature, this area is usually defined by the radius at which the mean over-density of the cluster is equal to some factor, Δ, times the critical density of the universe at that redshift, $\rho_{\rm clust}(r_\Delta) = \rho_{\rm crit}(r_\Delta)\Delta$. For X-ray measurements the value of Δ is usually chosen in a range between 500 and 2500 because the intra-cluster gas is expected to be virialized within this range of radii [37]. We adopt $\Delta = 2500$ with the r_{2500} calculated for each cluster given in Table 5.9. For this choice of Δ, r_{2500} is less than the SuZIE 5' difference chop, assuming a standard ΛCDM cosmology, for each cluster. In this section we will detail our calculation of the integrated SZ flux within r_{2500}, $S(r_{2500})$.

The total mass of a cluster whose gas distribution is described by an isothermal β model can be calculated, under the assumption of hydrostatic equilibrium and spherical symmetry, such that the total mass within a radius, r, is

$$M_{\rm clust}(r) = \frac{3kT_e\beta}{G\mu m_p}\frac{r^3}{r_c^2 + r^2} \tag{5.27}$$

where T_e is the cluster's electron temperature, μm_p is the mean molecular weight of the gas where we assume $\mu = 0.6$, with β and r_c corresponding to the β model parameters for the cluster. The cluster mass can be related to the critical density of the universe, $\rho_{\rm crit}$, by

$$M_{\rm clust}(r_\Delta) = \rho_{\rm crit}(z)\frac{4\pi r_\Delta^3}{3}\Delta \tag{5.28}$$

where $\rho_{\rm crit}(z) = 3H(z)^2/(8\pi G)$, $H(z)$ is the Hubble expansion rate at a redshift z, G is the gravitational constant, r_Δ is some radius of the cluster, and Δ is the constant which makes this expression true. For reasons given at the beginning of this section we adopt $\Delta = 2500$. Equation 5.28 can be re-arranged to solve for r_{2500} with

$$r_{2500} = \left[\frac{6}{2500} \frac{kT_e\beta}{\mu m_p} \frac{c^2}{H_0^2 E(z)^2} - r_c^2 \right]^{1/2} \tag{5.29}$$

where the variables are previously defined and where we have replaced $H(z)^2 = E(z)^2 H_0^2$ with $E(z)^2 \equiv \Omega_M(1+z)^3 + (1-\Omega_M-\Omega_\Lambda)(1+z)^2 + \Omega_\Lambda$. We can then define the integrated flux as

$$S(r_{2500}) = y_0 T_k \int_0^{r_{2500}/d_A} 2\pi \left(1 + \frac{\theta^2}{\theta_c^2}\right)^{1/2-3\beta/2} d\theta \tag{5.30}$$

where y_0 is the central Comptonization, T_k is the thermal SZ band-averaged spectral factor used in equation 5.12 and fully specified in section 5.2, θ_c and β are the IC gas model parameters, and d_A is the angular diameter distance to the cluster. We note that T_k depends on the cluster electron temperature due to relativistic corrections to the SZ spectrum. For the current SuZIE II 145 GHz (k=3) bandpass $T_3 = A \times 2(kT_{\rm CMB})^3/(hc)^2$ where $A = -3.93$ in the non-relativistic limit and varies between -3.6 and -3.8 over our typical range of electron temperatures.

We assume the following in our calculation of $S(r_{2500})$ from equation 5.30. For all the clusters in our sample, we have assumed the 145 GHz (k=3) band for the current SuZIE instrument, and we use the central Comptonization results which were calculated in section 5.8.1, whose values are given in Table 5.7. For all clusters we assume the IC gas model parameters given in Table 5.1. More precisely, for the non-cooling flow clusters we use the X-ray emission weighted temperatures, and for the cooling flow clusters we use the X-ray temperatures which account for the presence of the cooling flows. It is well-known from X-ray measurements, that cooling flows bias X-ray measured temperatures low compared to the virial temperature of the IC gas [see 1, for example]. The central Comptonization results given in section 5.8.1 assume the standard X-ray emission weighted temperature, even for the cooling flow clusters. However we will show in section 6.3.4 that this correction is negligible compared to the statistical uncertainty in our results. Making the above assumptions we calculate

Table 5.9. Integrated SZ Flux Results

Cluster	z	$E(z)$[b]	d_A (MPc)	r_{2500} (kPc)	r_{2500} (arcsec)	$S(r_{2500})$[a] (mJy)
A697	0.282	1.154	616	373	125	-245^{+45}_{-48}
A773	0.217	1.114	508	399	162	-326^{+71}_{-78}
R1347	0.451	1.271	833	448	111	-229^{+35}_{-38}
A2204	0.152	1.076	382	443	240	-266^{+50}_{-62}
A520	0.199	1.103	475	375	163	-212^{+55}_{-60}
A2390	0.232	1.123	534	465	179	-360^{+56}_{-55}
Zw3146	0.291	1.160	630	486	159	-109^{+37}_{-43}
A2261	0.224	1.118	520	413	164	-437^{+92}_{-167}
MS0451	0.550	1.348	926	390	86.9	$-73.9^{+8.6}_{-8.6}$
Cl0016	0.546	1.345	923	290	64.8	$-47.2^{+19.3}_{-20.0}$
A1835	0.252	1.135	568	379	138	-221^{+42}_{-48}
A1689	0.183	1.094	444	438	203	-459^{+50}_{-60}
A2163	0.202	1.105	480	465	200	-533^{+68}_{-74}
A545	0.153	1.077	384	321	172	-174^{+58}_{-146}
MS1054	0.823	1.587	1095	189	35.6	$-30.3^{+12.8}_{-12.5}$

[a]The integrated SZ flux, $S(r_{2500})$, is calculated assuming the SuZIE II 145 GHz band.

[b]$E(z)^2 \equiv \Omega_M(1+z)^3 + (1-\Omega_M-\Omega_\Lambda)(1+z)^2 + \Omega_\Lambda$

[c]For all calculations where cosmology is relevant, we assume a standard ΛCDM cosmology in a flat universe with $\Omega_M = 0.3$, $\Omega_\Lambda = 0.7$, and $h = 1$.

$S(r_{2500})$ for each cluster. These results are given in Table 5.9.

The error bars for $S(r_{2500})$ given in Table 5.9 are calculated from the statistical uncertainty in y_0 and T_e added in quadrature according to equation 5.30. In general, the statistical uncertainty in y_0 dominates the total uncertainty in $S(r_{2500})$. For example, in the case of RXJ1347, the overall uncertainty in $S(r_{2500})$ is $\sim$ 35mJy with the temperature uncertainty contributing an uncertainty of $\sim$ 8mJy in $S(r_{2500})$, which when added in quadrature is negligible. However, several clusters have significantly less constrained electron temperatures, particularly those clusters with cooling flow corrected temperatures based on ASCA data, for which the temperature uncertainty is a significant contribution to the overall uncertainty in $S(r_{2500})$.

5.8.3 Calculating the Gas Mass of a Cluster

From our SZ measurements we can also calculate the gas mass of the cluster. By integrating the the electron density over some given volume and multiplying by the nucleon to electron ratio, one recovers the gas mass within that volume. Precisely the gas mass of a cluster within a radius r_Δ, is

$$M_{\rm gas}(r_\Delta) = \int_0^{r_\Delta} \mu m_p n_e(r) dV \tag{5.31}$$

where μ is the nucleon to electron ratio, m_p is the proton mass, and $n_e(r)$ is the electron density as a function of radius. For our calculation we assume $\mu = 1.15$. This value corresponds to a cosmic mixture of hydrogen and helium. Generally higher values are inferred from X-ray measurements, however we have chosen this value to be consistent with Voevodkin et al. [106] for comparison in section 8.4. If we assume the gas density is well fit by a spherical Beta model then equation 5.31 becomes

$$M_{\rm gas}(r_\Delta) = 4\pi \mu m_p n_{e0} \int_0^{r_\Delta} r^2 \left(1 + \frac{r^2}{r_c^2}\right)^{-3\beta/2} dr \tag{5.32}$$

where n_{e0} is the central electron density, $r_c = \theta_c D_A$, D_A is the angular diameter distance to the cluster, and θ_c and β are the Beta model parameters. The central electron density can be calculated from the central Comptonization using

$$n_{e0} = \frac{y_0}{\sigma_T r_c} \frac{m_e c^2}{kT_e} \frac{1}{B(1/2, 3\beta/2 - 1/2)} \tag{5.33}$$

where σ_T is the Thompson cross-section, and $B(1/2, 3\beta/2 - 1/2)$ is the Beta function.

We calculate $M(r_{2500})$ from equation 5.32 for each cluster using the same cluster parameters assumed in our calculation of $S(r_{2500})$ in the previous section. We assume the central Comptonizations calculated in section 5.8.1, which uses only the SuZIE 145 GHz results, and the IC gas model parameters in Table 5.1. We give the results of these calculations in Table 5.10, where the error bars for the gas mass are calculated from the statistical uncertainty in y_0 and T_e added in quadrature according to equation 5.32. We include the gas mass calculated out to r_{500} for comparison to the X-ray measurements of Voevodkin et al. [106] in section 8.4.

Table 5.10. Gas Mass Results

Cluster	$M(r_{2500})$ (10^{13}M$_\odot$)	$M(r_{500})$
A697	$2.67^{+0.50}_{-0.46}$	$10.3^{+1.9}_{-1.8}$
A773	$3.05^{+0.73}_{-0.66}$	$10.3^{+2.5}_{-2.2}$
R1347	$4.41^{+0.73}_{-0.66}$	$12.1^{+2.0}_{-1.8}$
A2204	$1.76^{+0.34}_{-0.34}$	$4.6^{+0.9}_{-0.9}$
A520	$2.16^{+0.60}_{-0.54}$	$9.0^{+2.5}_{-2.3}$
A2390	$3.56^{+0.46}_{-0.46}$	$10.6^{+1.5}_{-1.4}$
Zw3146	$1.91^{+0.76}_{-0.73}$	$4.0^{+1.6}_{-1.5}$
A2261	$3.17^{+0.57}_{-0.57}$	$10.7^{+2.0}_{-2.0}$
MS0451	$2.74^{+0.28}_{-0.27}$	$7.4^{+0.8}_{-0.8}$
Cl0016	$1.87^{+0.78}_{-0.75}$	$7.8^{+3.2}_{-3.1}$
A1835	$3.23^{+0.69}_{-0.61}$	$9.1^{+1.9}_{-1.7}$
A1689	$3.45^{+0.40}_{-0.37}$	$9.8^{+1.1}_{-1.1}$
A2163	$3.68^{+0.45}_{-0.44}$	$13.0^{+1.6}_{-1.6}$
A545	$1.77^{+0.62}_{-0.46}$	$6.8^{+2.4}_{-2.7}$
MS1054	$1.67^{+0.73}_{-0.70}$	$14.1^{+4.4}_{-4.1}$

[a]For all calculations where cosmology is relevant, we assume a standard ΛCDM cosmology in a flat universe with $\Omega_M = 0.3$, $\Omega_\Lambda = 0.7$, and $h = 1$.

Chapter 6

Sources of Uncertainty

The results given in Table 5.5 do not include other potential sources of uncertainty in the data, such as calibration errors, uncertainties in the X-ray data, and systematic effects associated with our data acquisition and analysis techniques. We now show that these uncertainties and systematics are negligible compared to the statistical uncertainty associated with our SZ measurements. Astrophysical confusion is considered separately in section 6.4.

6.1 Calibration Uncertainty

To include the calibration uncertainty, we use a variant of the method described in Ganga et al. [41]. A flux calibration error can be accounted for by defining a variable, G_k, such that the correctly calibrated data is $D'_{kji} = G_k \times D_{kji}$. We further assume that the calibration error can be broken down into the product of an absolute uncertainty that is common to all frequency bands, and a relative uncertainty that differs between frequency bands. In this way we define $G_k = G^{abs} \times G_k^{rel}$ with the assumption that both G^{abs} and G_k^{rel} can be well-described by Gaussian distributions that are centered on a value of 1. The likelihood, marginalized over both calibration uncertainties, is then

$$L(y_0, v_p) = \int_0^\infty dG^{abs} P(G^{abs}) \int_0^\infty L(y_0, v_p, G^{abs}, G_1^{rel}, G_2^{rel}, G_3^{rel}) \prod_{k=1}^{3} dG_k^{rel} P(G_k^{rel}) \tag{6.1}$$

We evaluate these integrals by performing a 3 point Gauss-Hermite integration [see 86, for example] using the likelihoods calculated at the most-likely values, and the 1-σ confidence intervals, for G^{abs} and G_k^{rel}, which we will now discuss. While the main source of absolute calibration error in our data is the $\pm 6\%$ uncertainty in the RJ temperature of Mars and Saturn (see Section 3.6), it is not straightforward to label other calibration uncertainties as either absolute or relative. Instead we calculate equation (6.1) assuming two different calibration scenarios: one where our calibration uncertainty is entirely absolute such that $G^{abs} = [0.9, 1.00, 1.1]$ and $G_k^{rel} = [1.0, 1.0, 1.0]$ for all k, and the other which has a equal combination of the two with $G^{abs} = [0.93, 1.00, 1.07]$ and $G_k^{rel} = [0.93, 1.00, 1.07]$ for all values of k. This allows us to assess whether the assignment of the error is important.

We have recalculated the best fit y_0 and v_p using the MS0451 data taken in November 2000. We choose this data set because it has some of the lowest uncertainties of any of our data sets and consequently we would expect it to be the most susceptible to calibration uncertainties. Ignoring the calibration uncertainty, we calculate $y_0 = 3.17^{+0.86}_{-0.88} \times 10^{-4}$ and $v_p = -300^{+1950}_{-1275}$ km s^{-1} from marginalizing the likelihood as described in section 5.6. We then let G^{abs} and G_k^{rel} vary over their allowed range to calculate $L(y_0, v_p, G^{abs}, G_k^{rel})$ with a parameter space resolution of $\Delta y_0 = 10^{-6}$ and $\Delta v_p = 25\,\mathrm{km\,s^{-1}}$ in our two different calibration scenarios. Assuming only absolute calibration uncertainty we marginalize this likelihood over $G^{abs} = [0.9, 1.00, 1.1]$ and $G_k^{rel} = [1.0, 1.0, 1.0]$ and find that $y_0 = 3.14^{+0.88}_{-0.87} \times 10^{-4}$ and $v_p = -300^{+1925}_{-1250}$ km s^{-1}, values which are virtually unchanged from the best fit values assuming no calibration uncertainty. Assuming a combination of absolute and relative calibration uncertainty we marginalize this likelihood over $G^{abs} = [0.93, 1.00, 1.07]$ and $G_k^{rel} = [0.93, 1.00, 1.07]$. We find new best fit values of $y_0 = 3.15^{+0.87}_{-0.89} \times 10^{-4}$ and $v_p = -300^{+1925}_{-1275}$ km s^{-1}, again virtually identical to the values obtained assuming no calibration uncertainty. Therefore we conclude that for all our clusters the error introduced from calibration uncertainty, regardless of source, is negligible compared to the statistical error of the measurement. The effects of calibration uncertainties are summarized in Table 6.1.

6.2 Gas Density and Temperature Model Uncertainties

We now account for the effect of uncertainties in the β model parameters for the intra-cluster gas by fitting our SZ data with the allowed range of gas models based on the 1-σ uncertainties quoted for β and θ_c in Table 5.1. Ideally one would fit the X-ray and SZ data simultaneously to determine the best-fit gas model parameters. For several of our clusters this has been done using 30 GHz SZ maps by [88], and we use the values for the β model derived in this way. SuZIE II lacks sufficient spatial resolution to significantly improve on constraints from X-ray data, and so for clusters that are not in the Reese et al. [88] sample, we use the uncertainties derived from X-ray measurements alone.

Using a similar method to the calibration error analysis in the previous section, we assume that the range of allowable gas models can be well-approximated by a Gaussian distribution centered around the most-likely value and marginalize the resulting likelihood integrals over β and θ_{core} individually using 3 point Gauss-Hermite integration. In reality, the gas model parameters β and θ_{core} are degenerate and their joint probability distribution is not well-approximated by two independent Gaussians. However, this crude assumption allows us to show below that this source of error is relatively negligible compared to the statistical error of our results.

To estimate the effects of density model uncertainties in our sample we study the effect on MS0451 because it has one of the least well constrained density models from our sample. We find that when the allowable range of uncertainty on β and θ_c is included, the best fit SZ parameters are $y_0 = 3.16^{+0.87}_{-0.88} \times 10^{-4}$ and $v_p = -300^{+1900}_{-1275}$ km s^{-1}, virtually unchanged from the values in table 5.5. Therefore we conclude that the error from density model uncertainties is negligible compared to the statistical error

Table 6.1. Effects of Calibration and IC Gas Model Uncertainties on MS0451 (Nov 2000)

Uncertainty	$y_0 \times 10^4$	v_p (km s^{-1})
Statistical Uncertainty	$3.17^{+0.86}_{-0.88}$	-300^{+1950}_{-1275}
Calibration[a](Absolute Only)	$3.14^{+0.88}_{-0.87}$	-300^{+1925}_{-1250}
Calibration[a](Equal Absolute and Relative)	$3.15^{+0.87}_{-0.89}$	-300^{+1925}_{-1275}
IC Density Model	$3.16^{+0.87}_{-0.88}$	-300^{+1900}_{-1275}
IC Gas Temperature	$3.17^{+0.85}_{-0.87}$	-300^{+1925}_{-1275}

[a]See text for details

of the measurement.

To estimate the effects of temperature model uncertainties in our sample we again use MS0451 because it has one of the least constrained electron temperatures from our sample. We again assume that the range of allowable temperatures is well approximated by a Gaussian distribution centered around the most-likely value and marginalize the resulting likelihood integrals over T_e using 3 point Gauss-Hermite integration. We find $y_0 = 3.17^{+0.85}_{-0.87} \times 10^{-4}$ and $v_p = -300^{+1925}_{-1275}$ km s^{-1}, unchanged from the best fit values that assume no temperature uncertainty. Therefore we conclude that the error from temperature uncertainties is negligible compared to the statistical error of the measurement. The effects of gas model uncertainties are summarized in Table 6.1.

6.3 Systematic Uncertainties

We now consider effects that could cause systematic errors in our estimates of y_0 and v_p. These include instrumental baseline drifts that could mimic an SZ source in our drifts scan, and systematics introduced by our atmospheric subtraction technique.

6.3.1 Baseline Drifts

Previous observations using SuZIE II, and the single-frequency SuZIE I receiver, have found no significant instrumental baseline signal [71, 51, 52]. Baseline checks are performed using observations in patches of sky free of known sources or clusters. For the data presented in this paper we also use measurements with SuZIE II on regions of blank sky. In February 1998 we observed a region of blank sky at 07h40m0^s;+9°30′0″ (J2000) for a total of $\sim$ 18 hours of integration in exceptional weather conditions. The sky strip was 60′ in length and was observed in exactly the same way as the cluster observations presented in this paper. This data represents the most sensitive measurements ever made with SuZIE II and consequently should be very sensitive to any residual baseline signal (the data itself will be the subject of a separate paper). We have repeated exactly the analysis procedure used to analyze our cluster data with one exception, that we restrict the test source position in the blank sky field to be within $0\overset{\prime}{.}1$ of the pointing center. The source positions derived from the cluster data are consistently $\leq 30''$ from the pointing center indicating that there is no significant off-center instrumental baseline signal. For the fit, we use a generic SZ source model with $\beta = 2/3$ and $\theta_c = 20''$ and find the best-fit flux to the co-added data in each on-source frequency band. In our 145 GHz channel we find a best fit flux of $\Delta I = -1.05 \pm 2.12$ mJy, in our 221 GHz channel we find a best fit flux of $\Delta I = -3.56 \pm 3.79$ mJy, and in our 355 GHz channel we find a best-fit flux of $\Delta I = -1.91 \pm 6.94$ mJy. Using the November 2000 data from MS0451 as an example, if the blank sky flux measured at 145 GHz was purely thermal SZ in origin this would correspond to a central comptonization of $y_0 = 0.10 \pm 0.20 \times 10^{-4}$, while the blank sky flux measured at 221 GHz, assuming $\tau = 0.015$, corresponds to a peculiar velocity of $v_p = 635 \pm 676\,\mathrm{km\,s^{-1}}$. Therefore we conclude that there is no significant systematic due to baseline drifts in any of our three spectral bands.

6.3.2 Systematics Introduced by Atmospheric Subtraction

The model that was fitted to each data set, D_{kji}, as defined in equation (5.12), included common-mode atmospheric signal, C_{kji}, that was defined to be proportional to the average of our single channel signals, S_{kji}. While the single channel signal is dominated by atmospheric emission variations, it will also include some of the SZ signal we are trying to detect. This can potentially cause us to underestimate the SZ signal in our beam because part of it will be correlated with the single channel template. We estimate this effect from the correlation coefficients e_{kj} calculated during the minimization of χ^2_j in equation (5.13). We estimate that the SZ signal subtracted out from our common-mode atmospheric removal is $\sim 2\%$ of the total SZ signal, at a level that is negligible compared to the statistical error of our results.

The construction of a differential atmospheric template can potentially introduce residual SZ signal through our atmospheric subtraction routine. We discuss our method to construct a differential atmospheric template in appendix A and follow the notation defined therein. Residual SZ signal in this template can be introduced through the simplifying assumption that the α and γ used in its construction are spatially independent. In addition, uncertainties in the electron temperature and density model of the cluster affect how accurately α and γ are defined. Below we examine the effects of these two sources of uncertainty for the November 2000 observations of MS0451.

To model the effect of a residual SZ signal in our atmospheric template, A_{ji}, we re-define it by subtracting out the expected residual thermal and kinematic signals, Z_{ki}^{T} and Z_{ki}^{K} (defined in appendix A), binned to match the data set. To calculate Z_{ki}^{T} and Z_{ki}^{K} we use the values of α and γ given in Table 5.2 and assume the comptonization and peculiar velocity values given in Table 5.5. For all the clusters in our set we find $|Z_k^T(\theta)| < 5.7\,\mathrm{mJy}$ and $|Z_k^K(\theta)| < 1.7\,\mathrm{mJy}$ across a scan of the cluster. Using the re-defined atmospheric template we then repeat the analysis of the data set and recalculate comptonization and peculiar velocity. Using the November 2000 data of MS0451 as an example, we calculate $y_0 = 3.17^{+0.86}_{-0.88} \times 10^{-4}$ and $v_p = -300^{+1950}_{-1275}$ km s^{-1} using the method described in section 5.6. Using these values for comptonization and peculiar velocity, we re-define our atmospheric template as described above. We then repeat our analysis routine exactly, and calculate $y_0 = 3.14^{+0.85}_{-0.88} \times 10^{-4}$ and $v_p = -225^{+2000}_{-1300}$ km s^{-1}.

The accuracy of the construction of our differential atmospheric template, parameterized by the variables α and γ, is limited by our knowledge of each cluster's density model and electron temperature. We have calculated α and γ for each cluster using the best-fit spherical beta model parameters (β, θ_c), and electron temperature (T_e). We recalculate α and γ using the 1σ range of T_e, β and θ_c. For the November 2000 observations of MS0451, variations in the model parameters of the cluster cause $\lesssim 1\%$ changes in α and γ. Using the most extreme cases of α and γ we find changes of $\pm 0.01 \times 10^{-4}$ in y_0 and ± 25 km s^{-1} in v_p. Adding the two sources of error of differential atmospheric subtraction, discussed in the above paragraphs, in quadrature we find an overall uncertainty of $^{+0.01}_{-0.03} \times 10^{-4}$ in y_0 and $^{+75}_{-25}$ km s^{-1} in v_p. We therefore conclude that uncertainty from differential atmospheric subtraction adds negligible error compared to the statistical error of our results.

6.3.3 Position Offset

In section 5.4 we allow the position of our SZ model to vary in right ascension and determine confidence intervals for this positional offset. However, we do not have the necessary spatial coverage to constrain our clusters' position in declination, δ. If a cluster's position was offset from our pointing center in declination, we would expect the measured peak comptonization to be underestimated from the true value. From observations of several calibration sources over different nights, we estimate the uncertainty in pointing SuZIE to be $\lesssim 15''$. The cluster positions that we use are determined from ROSAT astrometry, which is typically uncertain by $\sim 10 - 15''$. Adding these uncertainties in quadrature we assign an overall pointing uncertainty of $\Delta\delta \sim 20''$.

To estimate the effects of pointing uncertainty in our sample we study the effect on observations of MS0451 in November 2000. Using the method described in section 5.6, which assumed no pointing offset, we calculated $y_0 = 3.17^{+0.86}_{-0.88} \times 10^{-4}$ and $v_p = -300^{+1950}_{-1275}$ km s^{-1}. We re-calculate the SZ model of MS0451 with a declination offset of $20''$ from our pointing center. Using this SZ model we repeat our analysis routine exactly and calculate $y_0 = 3.31^{+0.91}_{-0.91} \times 10^{-4}$ and $v_p = -300^{+1950}_{-1275}$ km s^{-1}. This corresponds to a $\sim 4\%$ underestimate of the peak comptonization, however there is no effect on peculiar velocity.

6.3.4 Systematic Uncertainties in the IC Gas Model

Here we will consider systematic uncertainties in the IC gas model. In particular, this discussion is meant to contrast how the calculated central Comptonization and integrated SZ flux depend on the IC gas model assumed. However, we will include a discussion of the gas model's effect on the calculated gas mass of the cluster. We will therefore only consider the effect of a systematic uncertainty in the IC gas model on the 145 GHz results.

Uncertain Beta Model

In order to examine the effect of an uncertain Beta model on our 145 GHz results, we have calculated the central Comptonization, and the integrated SZ flux out to r_{2500} for a range of Beta models for two of our clusters, A1689 and A1835. We have chosen these clusters because they are cooling flow clusters, whose X-ray emission, in general, is not as well characterized by a spherical isothermal Beta model. In addition, both clusters have at least two published Beta gas models derived from different X-ray instruments sensitive to different spatial scales. One of the systematic effects that we are primarily concerned about in using X-ray models to fit SZ observations is that the X-ray Beta models might over-fit to the cooling core for cooling flow clusters. This is a result of X-ray observations being more sensitive to over-densities in the core of a cluster than SZ observations, because $L_X \propto n_e^2$ while $I_{SZ} \propto n_e$. By choosing models derived from X-ray data which either do not resolve the cooling core, or exclude it entirely in the spatial fit, we can get some idea of the range of derivable Beta models from X-ray data for both clusters.

Figure 6.1 shows the calculated central Comptonization, y_0, integrated SZ flux, $S(r_{2500})$, and gas mass, $M(r_{2500})$, for A1835, assuming a suitable range of Beta models. In the figure the asterisk denotes the Beta model given in Reese et al. [88], derived from ROSAT-HRI data, and the plus sign denotes the Beta model given in Majerowicz et al. [65], which was derived from observations with XMM and excluded the central region of the cluster out to a radius of 42 arcsec. The choice of Beta model causes nearly a factor of 2 difference in the calculated central Comptonization between the two IC gas models. However, $S(r_{2500})$ varies by $\lesssim 3\%$ between the same models, with the line which connects the two models nearly lying along a line of constant integrated flux, while $M(r_{2500})$ varies by $\lesssim 10\%$.

Figure 6.2 shows the calculated central Comptonization, y_0, integrated SZ flux, $S(r_{2500})$, and gas mass, $M(r_{2500})$, for A1689, assuming a suitable range of Beta models. In the figure the asterisk denotes the Beta model given in Reese et al. [88], derived from ROSAT-HRI data, and the plus sign denotes the Beta model given in Holzapfel et al. [52], derived from ROSAT-PSPC data. Which IC gas model is assumed significantly changes the calculated central Comptonization, by $\sim 40\%$, and $M(r_{2500})$, by $\lesssim 25\%$.

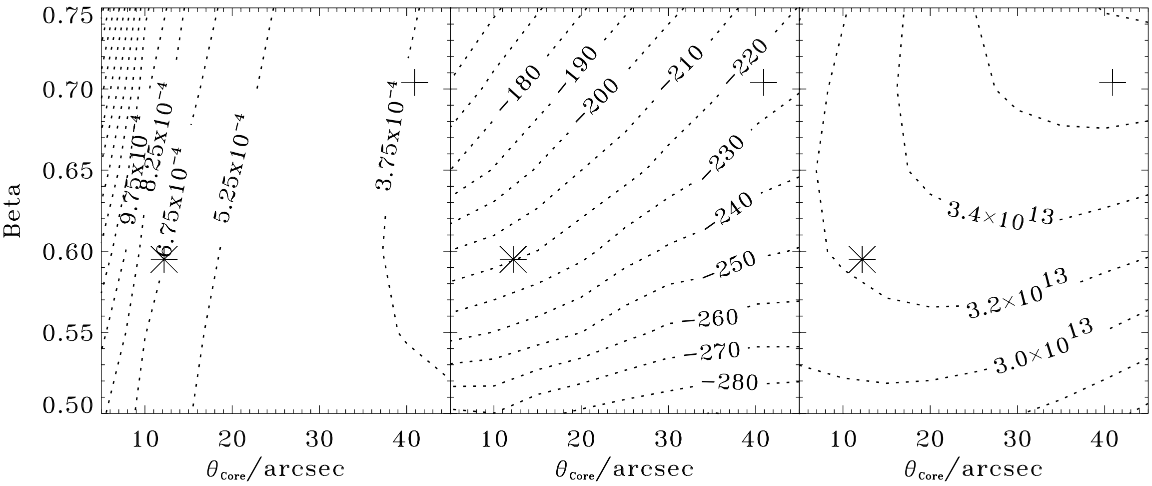

Fig. 6.1.— The best-fit y_0, $S(r_{2500})$, and $M(r_{2500})$ calculated for A1835 using a range of Beta models. The asterisk marks where the location of the gas model given in Reese et al. [88], and the plus sign marks the location of the Beta model given in Majerowicz et al. [65], which fits only the outer region of the cluster. (Left): The central Comptonziation of A1835, the contour levels spaced in 1.5×10^{-4} intervals. (Middle): The integrated SZ flux at 145 GHz, $S(r_{2500})$, from A1835, the contour levels are spaced in 10 mJy intervals. (Right): The gas mass, $M(r_{2500})$, of A1835, the contour levels are spaced in 0.2×10^{13} $M_\odot$ intervals.

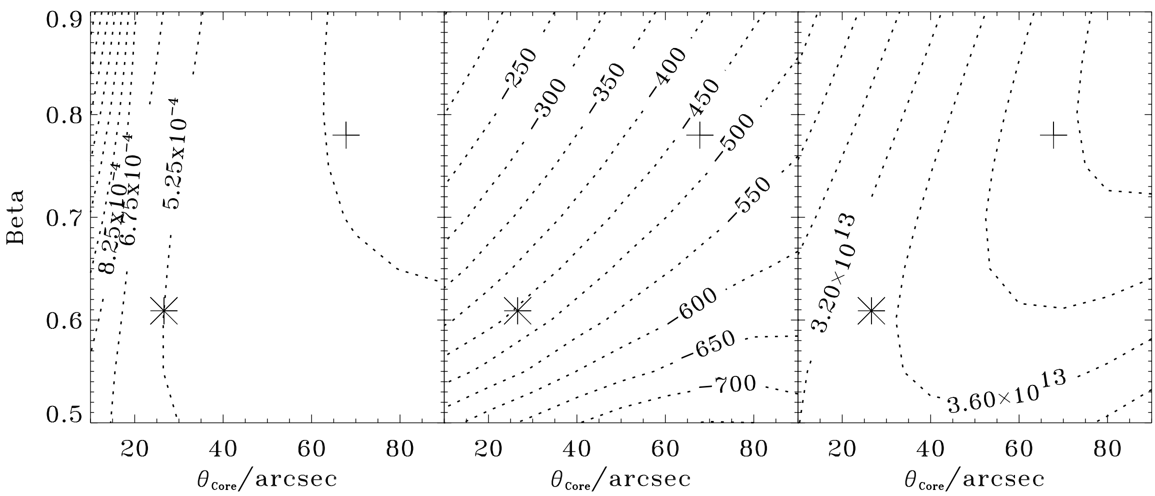

Fig. 6.2.— The best-fit y_0, $S(r_{2500})$, and $M(r_{2500})$ calculated for A1689 using a range of Beta models. The asterisk marks where the location of the gas model given in Reese et al. [88], and the plus sign marks the location of the Beta model given in Holzapfel et al. [52]. (Left): The central Comptonziation of A1689, the contour levels spaced in 1.5×10^{-4} intervals. (Middle): The integrated SZ flux at 145 GHz, $S(r_{2500})$, from A1689, the contour levels are spaced in 50 mJy intervals. (Right): The gas mass, $M(r_{2500})$, of A1689, the contour levels are spaced in 0.4×10^{13} $M_\odot$ intervals.

However, between the two models $S(r_{2500})$ varies by $\lesssim 2\%$.

As we have seen, for both A1835 and A1689 the calculated central Comptonization is much more sensitive to the assumed Beta model than is the integrated SZ flux. The physical reason why this is true is because both clusters are unresolved by SuZIE and therefore the calculated central Comptonization depends entirely on the assumed IC gas model. Conversely, $S(r_{2500})$ is less sensitive to the assumed IC gas model because r_{2500} is well-matched to the SuZIE beam-size, with r_{2500} within a factor of ~ 2 of the SuZIE beam-size for all our clusters. For our two example clusters, A1835 and A1689, $S(r_{2500})$ varies by $\lesssim 3\%$ even when significantly different Beta models derived from X-ray measurements with different spatial resolutions are used. The results for A1835 and A1689 imply that even if the X-ray IC gas model over-fits to the cooling core, this does not have a significant systematic effect on the value of $S(r_{2500})$ derived from the SuZIE measurements. We therefore conclude that the choice of Beta model adds a negligible uncertainty to $S(r_{2500})$ when compared to the statistical uncertainty of our data.

We should note that extending our integrated flux calculations to larger radii potentially increases the systematic error in the integrated SZ flux result. In Figures 6.3 and 6.4 we re-make the plots of central Comptonization, integrated SZ flux and the gas mass, but extend the cut-off radius to r_{500}. We note that extending the cut-off radius does not change the calculated central Comptonization.

For A1835 and A1689 increasing the integrating radius to r_{500} also increases the difference between $S(r_{500})$ derived from their two respective published IC gas models. For A1835 and A1689 the magnitude of $S(r_{500})$ decreases by $\sim 6\%$ and $\sim 16\%$, respectively, when using the broader core radius Beta model, relative to the narrower core radius model, for each cluster. This difference is not surprising considering r_{2500} is already greater than the SuZIE beam-size for most of our clusters, see Table 5.9, with r_{500} generally a factor of $\sim$2 larger than r_{2500} for a typical cluster. Regardless, there seems to be a systematic trend towards over-estimating the integrated SZ decrement out to r_{500} by $\sim$ 5-20% when using the narrower core radius models for cooling flow clusters. This level of uncertainty is approximately equal to the statistical uncertainty of our measurements, and should be considered when extrapolating our integrated SZ

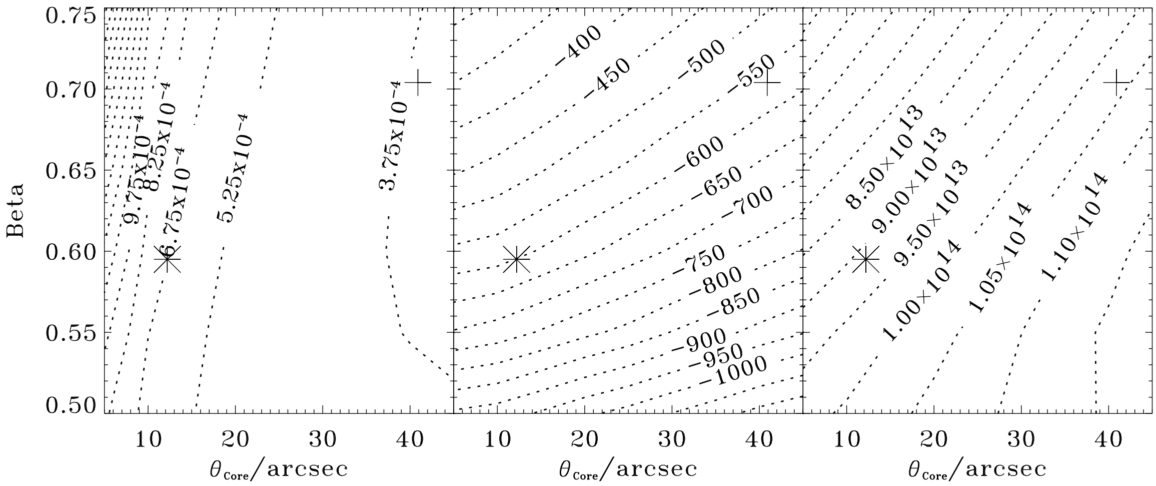

Fig. 6.3.— The best-fit y_0, $S(r_{500})$, and $M(r_{500})$ calculated for A1835 using a range of Beta models. The asterisk marks where the location of the gas model given in Reese et al. [88], and the plus sign marks the location of the Beta model given in Majerowicz et al. [65], which fits only the outer region of the cluster. (Left): The central Comptonziation of A1835, the contour levels spaced in 1.5×10^{-4} intervals. (Middle): The integrated SZ flux at 145 GHz, $S(r_{500})$, from A1835, the contour levels are spaced in 50 mJy intervals. (Right): The gas mass, $M(r_{500})$, of A1835, the contour levels are spaced in 0.5×10^{13} $M_\odot$ intervals.

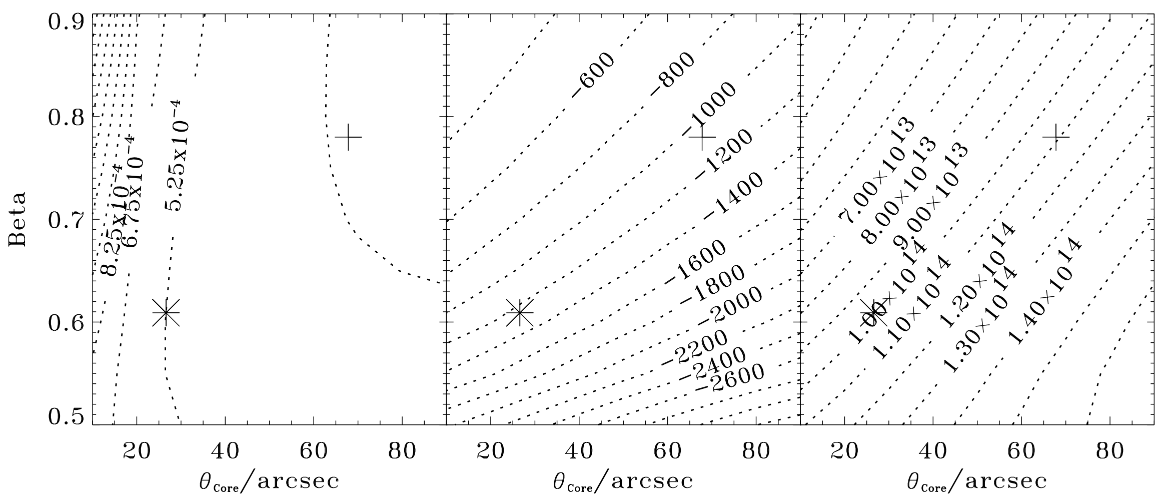

Fig. 6.4.— The best-fit y_0, $S(r_{500})$, and $M(r_{500})$ calculated for A1689 using a range of Beta models. The asterisk marks where the location of the gas model given in Reese et al. [88], and the plus sign marks the location of the Beta model given in Holzapfel et al. [52]. (Left): The central Comptonziation of A1689, the contour levels spaced in 1.5×10^{-4} intervals. (Middle): The integrated SZ flux at 145 GHz, $S(r_{500})$, from A1689, the contour levels are spaced in 200 mJy intervals. (Right): The gas mass, $M(r_{500})$, of A1689, the contour levels are spaced in 1.0×10^{13} $M_\odot$ intervals.

flux measurements to larger cluster radii.

Surprisingly, extending the cut-off radius does not have much of an effect on the level of uncertainty for the calculated gas mass of the clusters. For A1835 and A1689 the magnitude of $M(r_{2500})$ increases by $\sim 11\%$ and $\sim 24\%$, respectively, when using the broader core radius Beta model, relative to the narrower core radius model, for each cluster. However, if we compare $M(r_{500})$ calculated from the same models for A1835 and A1689, $M(r_{500})$ increases by only $\sim 12\%$ and $\sim 11\%$. This seems to indicate that $M(r_{500})$ does not have a significant systematic uncertainty due to the assumed Beta model.

The Electron Temperature

In section 6.2, it was shown that the typical quoted uncertainty on the X-ray derived electron temperatures cause a negligible uncertainty to the SuZIE derived central Comptonization. A previous SuZIE paper by Holzapfel et al. [52] used a more complicated cluster thermal structure, suggested from ASCA observations, to analyze their 145 GHz results and found that the value of the central Comptonization was relatively insensitive to the details of the thermal structure. Therefore in this discussion we restrict ourselves to investigating the effect of a significant systematic uncertainty in the assumed isothermal electron temperature. To some degree a systematic uncertainty in the electron temperature is expected due to any difference between the X-ray derived temperature and the mass weighted temperature, which is relevant for SZ observations. Simulations by Mathiesen & Evrard [69] predict that temperatures derived from spectral fits to X-ray data are $\sim$ 1-3keV less than the mass weighted temperature, with the systematic offset proportional to the temperature of the cluster. In this section we discuss the effect of a systematic uncertainty on the calculated central Comptonization and the integrated SZ flux.

We first consider the effect on the calculated central Comptonization of a significant systematic unceratinty in electron temperature. Mathiesen & Evrard [69] suggests that in the most extreme cases the mass weighted temperature is $\sim$40% higher than the X-ray spectral temperature. We can consider the case of RXJ1347, one of the most significant cluster detections from our 145 GHz data, to examine the effect of this large a temperature uncertainty on the central Comptonization. If we consider the central Comptonization to be a function of the assumed electron temperature, such that $y_0(T_e/\mathrm{keV})$, and we re-calculate the central Comptonization of RXJ1347, as prescribed in section 5.8.1, we find $y_0(9.3/\mathrm{keV}) = 12.31^{+1.89}_{-1.72}$ and $y_0(14.1/\mathrm{keV}) = 12.69^{+1.67}_{-1.58} \times 10^{-4}$. Therefore a $\sim$ 50% change in the assumed electron temperature causes only a $\sim$3% change in the calculated central Comptonization, a change far below our statistical and/or calibration uncertainty. This is what one would naively expect because the calculated central Comptonization depends on the temperature through relativistic corrections to the SZ spectrum, which are still relatively small at 145 GHz for a reasonable range of temperatures. We conclude that any uncertainty in the electron temperature causes a negligible contribution to the uncertainty of the central Comptonization for all the clusters in our sample.

A temperature uncertainty causes an uncertainty in the integrated SZ flux through the dependence of the calculated central Comptonization and r_{2500} on temperature. In the previous paragraph we showed that the calculated central Comptonization is negligibly sensitive to the temperature. According to equation 5.30, the integrated SZ flux depends linearly on the central Comptonization, so therefore a temperature uncertainty would translate negligibly to the uncertainty in the integrated SZ flux. We are then only concerned with a systematic uncertainty in temperature and its effect on r_{2500}. As previously stated, the reason we might expect a systematic bias in the temperature is because of the difference between the mass-weighted temperature and the X-ray spectral temperature. In simulations by Mathiesen & Evrard [69], the relationship between these temperatures is well-fit by a power-law with a measured X-ray spectral temperature of $\sim$14 keV corresponding to a predicted mass-weighted temperature of $\sim$17 keV. A temperature difference this large would significantly change our $S(r_{2500})$ results; however the overall effect would be to bias our $S(r_{2500})$ in a characterizable way which scales with temperature. A bias of this nature may be more appropriately dealt with through simulations, analogous to those of Mathiesen & Evrard [69]. Also when we calculate SZ scaling relations, which include X-ray temperature, in section 8, it would be useful to use the same X-ray temperature that analogous X-ray scaling relations are constructed from for comparison purposes. For these reasons we do not consider the effect of a systematic uncertainty in the electron temperature on $S(r_{2500})$, except to note that a systematic bias could exist in the X-ray determined electron temperatures, and generally should be considered when interpreting our results.

The gas mass depends on the electron temperature through the calculated central electron density and the definition of r_{2500}. These two effects on the calculated gas mass somewhat cancel each other. From SZ measurements, a higher electron temperature implies a lower electron density, and therefore a lower gas mass, but also a larger value of r_Δ, or equivalently a larger integrating area on the sky, and therefore a higher gas mass. To quantitatively examine the effect of electron temperature on gas mass, we again consider the case of RXJ1347 and calculate its gas mass assuming two different temperatures, 9.3 and 14.1 keV. If we consider the gas mass a function of temperature, $M(T_e, r_\Delta)$, we find $M(9.3\mathrm{keV}, r_\Delta) = 5.17 \times 10^{13}$ $\mathrm{M}_\odot$ and $M(14.1\mathrm{keV}, r_\Delta) = 4.48 \times 10^{13}$ $\mathrm{M}_\odot$. This does represent a $\sim 15\%$ change in the calculated gas mass, however the difference is within the 68% confidence region for the $M(r_{2500})$ results quoted in Table 5.10. Extending the cut-off radius to r_{500} produces a similar relative change in the calculated mass.

6.4 The Effects of Astrophysical Confusion

6.4.1 Primary Anisotropies

Measurements of the kinematic SZ effect are ultimately limited by confusion from primary CMB anisotropies which are spectrally identical to the kinematic effect in the non-relativistic limit. LaRoque et al. [63] have estimated the level of CMB contamination in the SuZIE II bands for a conventional $\Omega_m = 0.3$ (ΛCDM) cosmology using the SuZIE II beam size, at $|\delta y_0| < 0.05 \times 10^{-4}$ and $|\delta v_{pec}| < 380$ km s^{-1}. At present this is negligible compared to our statistical uncertainty.

6.4.2 Sub-millimeter Galaxies

Sub-millimeter galaxies are a potential source of confusion, especially in our higher frequency channels. All of our clusters have been observed with SCUBA at 450 and 850 μm and sources detected towards all of them at 850μm [98, 17]. Because of the extended nature of some of these sources, it is difficult to discern which are true point sources and which are, in fact, residual SZ emission [71]. This is especially true when the source is only detected at 850μm. We assume a worst-case – that all of the emission is from point sources – and examine the effects of confusion in MS0451, A1835, and A2261. We select these clusters because the sources in MS0451 and A2261 have SCUBA fluxes typical of all of the clusters in our set, while A1835 has the largest integrated point source flux, as measured by SCUBA, of all our clusters. The SCUBA fluxes in these clusters are also consistent with the expected level of confusion from cluster members and lensed background galaxies in the models of [10]. We consider only sources with declinations that are within $1'$ in declination of our pointing center since these sources will have the greatest effect on our measurements. The point sources that meet this criterion are shown in Table 6.2. To model a source observation, we use SCUBA measurements to set the expected flux at 850μm, and assume a spectral index, α, of 2 or 3 to extrapolate to our frequency bands, where the flux in any band is $S_\nu \propto \nu^\alpha$. In the case of A1835, where 450 μm fluxes have also been measured, the spectral indices of the detected sources range from 1.3–2, with large uncertainties. For this cluster we also examine the effect of an index of 1.7.

Note that because our beam is large we cannot simply mask out the SCUBA sources from our scans without removing an unacceptably large quantity of data. Instead, for each cluster, the sources are convolved with the SuZIE II beam-map to create a model observation at each frequency. This model is then subtracted from each scan of the raw data, and the entire data set is re-analyzed. The results are summarized in Table 6.3. The overall effect of sub-millimeter point sources is to increase the measured flux at each frequency by $10 - 50\%$ of the point source flux at that frequency. The reason that the flux error is less than the true point source flux is that spectrally the point sources are not too different from atmospheric emission, which also rises strongly with frequency, and so the sources are partially removed

Table 6.2. SCUBA sources towards MS0451, A1835 and A2261.

Cluster	Source	Source Coordinates RA[a](J2000)	Dec[a](J2000)	Flux (mJy) 850μm	450μm	Ref.
A2261	SMMJ17223+3207	17 22 20.8	+32 07 04	17.6 ± 3.9	–	1
...	...	...	...	...	...	
A1835	SMMJ14009+0252	14 00 57.7	+02 52 50	14.5 ± 1.7	33 ± 7	2
	SMMJ14011+0252	14 01 05.0	+02 52 25	12.3 ± 1.7	42 ± 7	2
	SMMJ14010+0252	14 01 02.3	+02 52 40	5.4 ± 1.7	20 ± 7	2
...	...	...	...	...	...	
MS0451	SMMJ04542-0301	04 54 12.5	−03 01 04	19.1 ± 4.2	–	1

References. — (1) Chapman et al. [17]; (2) Smail et al. [98]

[a]Units of RA are hours, minutes and seconds and units of declination are degrees, arcminutes and arcseconds

during our atmospheric subtraction procedure. Because the residual point source flux is the same sign at all frequencies, it is spectrally most similar to the kinematic effect. Consequently the effect on the final results is to slightly over-estimate the comptonization, with the peculiar velocity biased to a more negative value by several hundred $\mathrm{km\,s^{-1}}$. While the uncertainty this introduces is currently small compared to the statistical uncertainty of our measurements, it is a systematic that will present problems for future more sensitive measurements and we expect that higher resolution observations than SCUBA will be needed in order to accurately distinguish point sources from SZ emission. In addition the SCUBA maps cover only $2\farcm3$, and so all of the sources that we consider here cause a systematic velocity towards the observer. Because of the differencing and scan strategy that we use, sources that lie outside the SCUBA field of view can cause an apparent peculiar velocity away from the observer which is not quantified in this analysis. We conservatively estimate this contribution to be equal in magnitude but opposite in sign to the effect of sources within the field of view. In reality, the effects will likely cancel to some degree, reducing the overall uncertainty associated with submm sources.

6.5 Unknown Sources of Systematics

Finally, in order to check for other systematics in our data, we calculate the average peculiar velocity of the entire set of SuZIE II clusters. Taking into account the likelihood function of each measurement based on the statistical uncertainties only, we find that the average is -580^{+360}_{-330} km s^{-1}. If our peculiar velocity measurements were unbiased, we would expect this result to be consistent with zero, it is not. Indeed, looking at the cluster peculiar velocities in Table 5.5, there are 5 clusters with $\approx 1\sigma$ detections of a negative peculiar velocity all with $v_p \lesssim -1000$ km s^{-1}. In section 6.4.2 it was shown that typical sub-millimeter point source confusion could bias our peculiar velocities negative by several hundred km s^{-1}. Sub-millimeter point source confusion could be responsible for the small bias towards negative peculiar velocities measured in the SuZIE II clusters. However, if we include previous peculiar velocity measurements made with the SuZIE I receiver of A1689 and A2163 [52],

Table 6.3. MS0451, A2261, and A1835 Sub-mm Galaxy Confusion

Cluster	Spectral Model	Flux/mJys 145GHz	Flux/mJys 221GHz	Flux/mJys 273/355GHz[b]	$y_0 \times 10^4$	v_p (km s^{-1})
MS0451	No Source[a]	$-23.4^{+4.3}_{-4.3}$	$-4.9^{+7.2}_{-7.2}$	$+54.7^{+16.5}_{-16.5}$	$3.17^{+0.86}_{-0.88}$	-300^{+1950}_{-1275}
	$\alpha = 3$	$-24.1^{+4.3}_{-4.3}$	$-6.8^{+7.2}_{-7.2}$	$+51.0^{+16.5}_{-16.5}$	$3.03^{+0.85}_{-0.87}$	0^{+2175}_{-1350}
	$\alpha = 2$	$-25.4^{+4.3}_{-4.3}$	$-8.9^{+7.2}_{-7.2}$	$+48.6^{+16.5}_{-16.5}$	$2.96^{+0.86}_{-0.86}$	$+350^{+2300}_{-1450}$
...	...	...	...	...	...	
A2261	No Source[a]	$-43.0^{+4.6}_{-4.6}$	$+7.9^{+14.1}_{-14.1}$	$+106.9^{+29.5}_{-29.5}$	$7.41^{+1.93}_{-1.97}$	-1575^{+1500}_{-975}
	$\alpha = 3$	$-43.5^{+4.6}_{-4.6}$	$+6.6^{+14.1}_{-14.1}$	$+104.0^{+29.6}_{-29.6}$	$7.25^{+1.94}_{-1.97}$	-1475^{+1575}_{-1000}
	$\alpha = 2$	$-44.3^{+4.6}_{-4.6}$	$+5.7^{+14.2}_{-14.2}$	$+103.3^{+29.6}_{-29.6}$	$7.23^{+1.94}_{-1.97}$	-1400^{+1600}_{-1025}
...	...	...	...	...	...	
A1835	No Source[a]	$-36.3^{+5.9}_{-5.9}$	$+3.6^{+8.8}_{-8.8}$	$+37.6^{+13.1}_{-13.1}$	$7.66^{+1.64}_{-1.64}$	-175^{+1675}_{-1250}
	$\alpha = 3$	$-36.7^{+5.9}_{-5.9}$	$+2.4^{+8.8}_{-8.8}$	$+36.0^{+13.2}_{-13.2}$	$7.52^{+1.62}_{-1.66}$	-50^{+1725}_{-1300}
	$\alpha = 2$	$-37.7^{+5.9}_{-5.9}$	$+1.3^{+9.0}_{-9.0}$	$+35.5^{+13.4}_{-13.4}$	$7.50^{+1.64}_{-1.64}$	$+25^{+1775}_{-1275}$
	$\alpha = 1.7$	$-38.3^{+5.9}_{-5.9}$	$+0.8^{+9.1}_{-9.1}$	$+35.2^{+13.5}_{-13.5}$	$7.50^{+1.64}_{-1.64}$	$+75^{+1775}_{-1300}$

[a]This row assumes that there are no sources in the data

[b]The high frequency channel during the MS0451 and A2261 observations was configured to observe at 355 GHz, but for the A1835 observations was configured to observe at 273 GHz.

see Table 5.5 for a summary of these measurements, the average peculiar velocity becomes -260^{+310}_{-295} km s^{-1}. Because this result is consistent with zero, we conclude there are no significant sources of systematic uncertainty in our peculiar velocity results. Future measurements with higher spatial resolution or more frequency bands should resolve the degree to which sub-millimeter point source confusion is biasing our peculiar velocity results.

6.6 Summary

Table 6.4 summarizes the effect of all of the known sources of uncertainty in our measurement of the peculiar velocity of MS0451. We expect similar uncertainties for the other clusters in our sample. Other than the statistical uncertainty of the measurement itself, the dominant contribution is from CMB fluctuations and point sources. Note that we do not include the calculation of the baseline presented in section 6.3.1 because our measurements show no baseline at the limit set by astrophysical confusion.

Table 6.4. Comptonization and Peculiar Velocity Uncertainties for MS0451 (Nov 2000)

Uncertainty	$y_0 \times 10^4$	v_p (km s^{-1})
Statistical:	$3.17^{+0.86}_{-0.88}$	-300^{+1950}_{-1275}
Systematic:		
Common-Mode Atmospheric Removal	$^{+0.06}_{-0.06}$	$^{+10}_{-10}$
Differential-Mode Atmospheric Removal	$^{+0.01}_{-0.03}$	$^{+75}_{-25}$
Position Offset	$^{+0.14}_{-0.00}$	$^{+0}_{-0}$
Primary Anisotropies	$^{+0.05}_{-0.05}$	$^{+380}_{-380}$
Sub-millimeter Galaxies	$^{+0.21}_{-0.21}$	$^{+650}_{-650}$
Total:[a]	$3.17^{+0.86+0.26}_{-0.88-0.23}$	$-300^{+1950+757}_{-1275-753}$

Note. — [a] The first number is the statistical uncertainty, the second is the systematic uncertainty

Chapter 7

Comparison of SZ Measurements with Previous Results

In total the SuZIE observing program has detected the SZ spectrum of 13 clusters of galaxies and detected an SZ decrement in 15 clusters of galaxies, see Holzapfel et al. [52], Benson et al. [9], and this paper. An important systematic check is to compare our results to SZ measurements using other instruments. The most comprehensive set of SZ measurements published are those by Reese et al. [88] using the Berkeley-Illinois-Maryland Association (BIMA) and Owens-Valley Radio Observatory (OVRO) millimeter wavelength interferometers. A total of 10 clusters overlap between the SuZIE cluster sample and the set published in Reese et al. [88]. In this section we derive a central Comptonization for each of the 10 overlapping clusters published in Reese et al. [88] and compare these values for the calculated central Comptonizations from SuZIE. To simplify the comparison of these clusters we have used the same IC gas model as Reese et al. [88] to analyze our measurements.

7.1 BIMA and OVRO

The BIMA and OVRO arrays are millimeter wavelength interferometers, which have been outfitted with centimeter wavelength receivers to observe the SZ effect. The receivers use High Electron Mobility Transistor (HEMT) amplifiers which are used to observe the SZ effect in a band between 28-30 GHz. At this observing frequency the primary beams for each interferometer are nearly Gaussian with a FWHM of 6.6' for BIMA and 4.2' for OVRO. The angular resolution varies depending on the configuration of the dishes during each particular observation, but is typically $\sim$ 95×95 arcsec for BIMA and $\sim 50 \times 50$ arcsec for OVRO. For an overview of the interferometers and the SZ observations using them see Reese et al. [88].

7.1.1 Fitting a Central Comptonization to the BIMA and OVRO Data

The BIMA and OVRO interferometers observe the SZ effect in a narrow frequency band at $\nu \sim 28.5$ GHz. Because their measurements are effectively at a single frequency they are unable to constrain both a central Comptonization and a peculiar velocity from their data alone. Instead, the SZ results quoted by Reese et al. [88] give the central intensity of each cluster in units of thermodynamic temperature. The measured difference temperature, ΔT, is then a sum of thermal and kinematic components with

$$\Delta T = y_0 T_{\rm CMB} \frac{(e^x-1)^2}{x^4 e^x} \frac{m_e c^2}{kT_e} \left[\Psi(x, T_e) - \frac{v_p}{c} h(x, T_e) \right] \tag{7.1}$$

where $\Psi(x, T_e)$ and $h(x, T_e)$ are fully specified in Benson et al. [9] and include relativistic corrections to their frequency dependence based on the calculations of Rephaeli [91] and Nozawa et al. [78] respectively.

In order to compare the BIMA and OVRO measurements to ours we want to fit a central Comptonization to the temperature decrement given in Reese et al. [88]. The observations described in Reese et al. [88] were taken in two different receiver configurations with central observing frequencies of $\nu = 28.5$ and 30.0 GHz respectively. Reese et al. [88] does not systematically note which sets of data correspond to which observing frequency. Because we are nearly in the Rayleigh-Jeans region of the spectrum, the calculated central Comptonization for a typical cluster varies by $< 1\%$

if we assume a central observing frequency between 28.5 and 30.0 GHz. For simplicity, we therefore assume all observations in Reese et al. [88] were taken at a central observing frequency of $\nu = 28.5$ GHz with a Gaussian envelope 0.5 GHz in width. We can then calculate a central Comptonization derived from the published central decrements in Reese et al. [88] in a way exactly analogous to the method in section 5.8.1, which was used to analyze the SuZIE 145 GHz data. From equation 7.1, we calculate a two-dimensional $\chi^2(v_p, y_0)$ over an appropriate range of parameter space for peculiar velocity and central Comptonization. Under the assumption of Gaussian errors on ΔT, we calculate a likelihood, $L(v_p, y_0) \propto \exp(-\chi^2(v_p, y_0)/2)$. We multiply $L(v_p, y_0)$ by a Gaussian prior on the peculiar velocity, where $L(v_p) \propto \exp(-v_p^2/2\sigma_v^2)$, with $\sigma_v = 0, 500$, and 2000 km s^{-1} as our three cases. We then marginalize the resultant likelihood over peculiar velocity to calculate the best-fit Comptonization and 68% confidence region for the three cases of σ_v and give these results in Table 7.1

In general the main effect of increasing the width of the Gaussian prior on the peculiar velocity is to expand the corresponding confidence region for the central Comptonization. For each cluster the BIMA and OVRO best-fit central Comptonization changes negligibly between the different priors, however the width of the confidence region expands by a factor of $\approx 2-3$ between an exactly zero peculiar velocity and $\sigma_v = 2000\,\mathrm{km\,s^{-1}}$.

7.2 Comparing Results from SuZIE to BIMA/OVRO

We can compare the central Comptonization results calculated from BIMA/OVRO to the central Comptonization calculated from both the SuZIE multi-frequency data and the SuZIE 145 GHZ data. The SuZIE 145 GHz data gives better constraints on the central Comptonization than the multi-frequency results, for reasons discussed in section 5.8.1, however both comparisons are useful because they are sensitive to different systematics. For example, the SuZIE multi-frequency results may be more appropriate if clusters have larger peculiar velocities than expected, conversely the SuZIE 145 GHz data would be more appropriate if sub-millimeter point sources bias the higher frequency channels.

To facilitate comparison to the BIMA/OVRO results, we re-analyze the multi-frequency SuZIE results from section 5.6 using the same method used to analyze the BIMA/OVRO results as described in the previous section. In Table 7.1 we give the best-fit Comptonization and 68% confidence region derived from the multi-frequency SuZIE results assuming three different priors on the peculiar velocity with Gaussian widths of $\sigma_v = 0, 500$, and 2000 km s^{-1}. We note that we are considering a broader range of priors on the peculiar velocity on the SuZIE multi-frequency results versus the SuZIE 145 GHz results. We do this because the multi-frequency results already constrain the peculiar velocity to some degree and therefore should be more appropriate if we are considering a larger range of possible peculiar velocities.

Comparing the results of Table 7.1, the SuZIE derived central Comptonizations are higher than the results from BIMA and OVRO for all the clusters except Cl0016. For the case of $\sigma_v = 500$ km s^{-1}, the clusters A697, A773, RXJ147, A1835, and A2261 all have significantly higher Comptonizations as measured by SuZIE. Even for the case of $\sigma_v = 2000$ km s^{-1}, the clusters A1835 and A2261 are still significantly inconsistent between the two data sets.

If instead we compare the central Comptonizations calculated from the SuZIE 145 GHz data in section 5.8.1 to the BIMA and OVRO results, SuZIE continues to measure a higher central Comptonization for most clusters. Figure 7.1 plots the central Comptonization calculated from the SuZIE 145 GHz data, calculated in section 5.8.1, to the central Comptonization calculated from the BIMA and OVRO measurements, where we have assumed $\sigma_v = 500$ km s^{-1} for both calculations. Again the SuZIE derived central Comptonizations are systematically higher than the OVRO/BIMA results, particularly in cooling flow clusters. On average, the SuZIE calculated central Comptonizations are $\sim 12\%$ higher in the non-cooling flow clusters, and $\sim 60\%$ higher in the cooling flow clusters.

This discrepancy is equivalent to the statement that SuZIE is measuring a systematically higher SZ flux than expected for the spherical isothermal beta model normalized to the central Comptonization given in Reese et al. [88]. This suggests that the SuZIE measurement is either inconsistent with this central Comptonization,

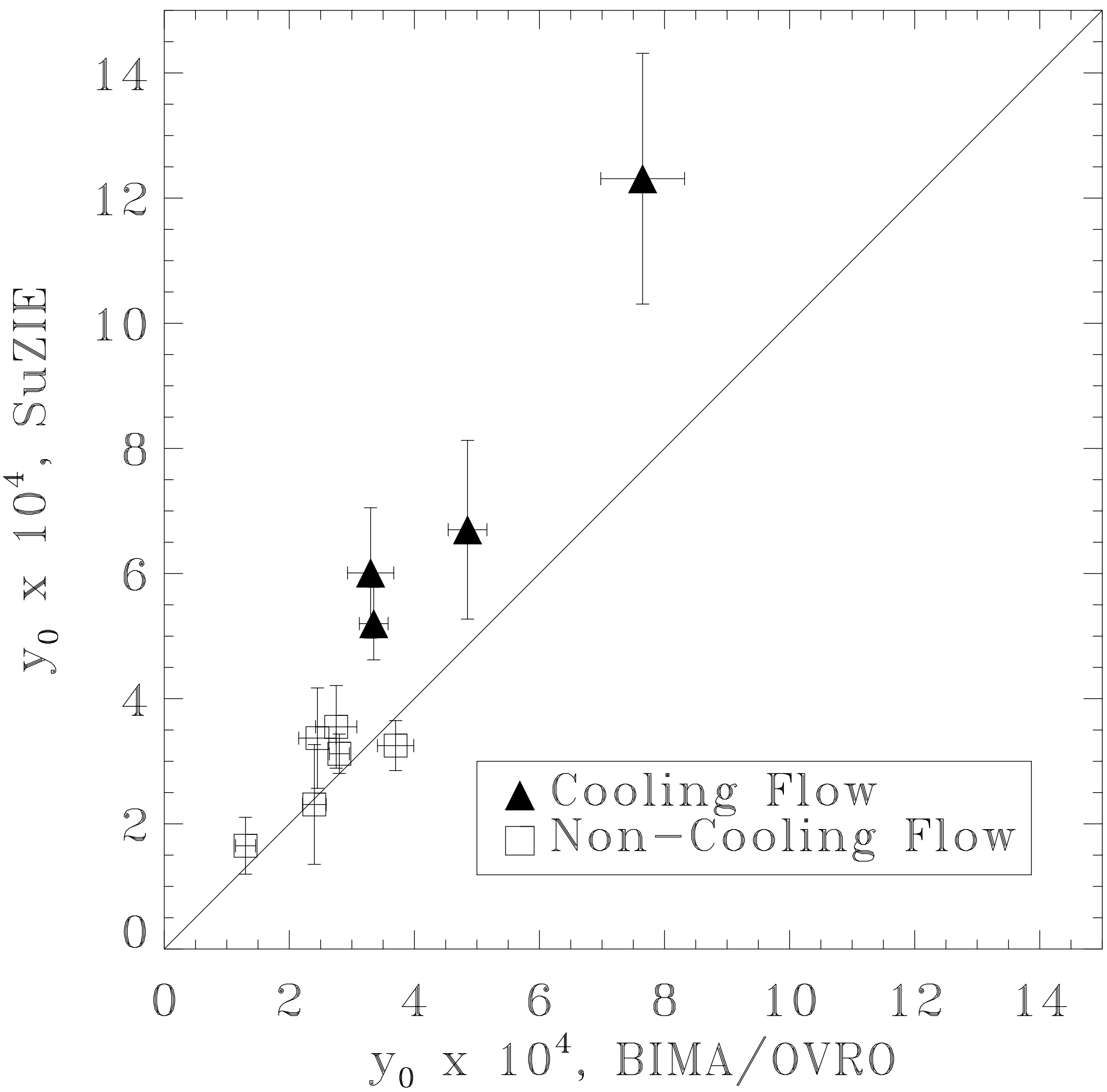

Fig. 7.1.— A plot of the central Comptonization measured by SuZIE versus the central Comptonization measured by the BIMA/OVRO interferometers. The SuZIE central Comptonization calculation is based on the method described in section 5.8.1. Both measurements assume a zero peculiar velocity with a Gaussian prior on the peculiar velocity with a width of 500 km s^{-}1. Clusters with cooling cores are labelled with triangles and non-cooling core clusters are labelled with squares.

and/or the IC gas model. It was shown in section 5.8.1, that the central Comptonization derived by SuZIE is very sensitive to the assumed IC gas model. Given that SuZIE is sensitive to different spatial scales than OVRO or BIMA, it is possible that the SuZIE measurements be consistent with the OVRO and BIMA measurements and still derive a different central Comptonization if the Beta model does not fit the IC gas distribution well. This discrepancy will be investigated further in a future paper.

Table 7.1. Central Comptonization Results with Different Priors on Peculiar Velocity.

σ_v (km s^{-1})	$y_0 \times 10^4$ A697	A773	A520	RXJ1347
		BIMA/OVRO		
0	$2.75^{+0.33}_{-0.32}$	$2.45^{+0.30}_{-0.31}$	$1.30^{+0.16}_{-0.20}$	$7.65^{+0.67}_{-0.67}$
500	$2.75^{+0.36}_{-0.34}$	$2.45^{+0.32}_{-0.34}$	$1.25^{+0.22}_{-0.17}$	$7.65^{+0.77}_{-0.76}$
2000	$2.70^{+0.71}_{-0.55}$	$2.35^{+0.70}_{-0.49}$	$1.20^{+0.45}_{-0.26}$	$7.40^{+2.00}_{-1.41}$
		SuZIE		
0	$3.92^{+0.65}_{-0.64}$	$4.54^{+1.36}_{-1.36}$	$1.84^{+0.59}_{-0.59}$	$11.70^{+1.85}_{-1.85}$
500	$4.04^{+0.77}_{-0.72}$	$4.53^{+1.45}_{-1.40}$	$1.88^{+0.59}_{-0.59}$	$11.47^{+2.12}_{-2.00}$
2000	$4.61^{+1.03}_{-1.00}$	$4.43^{+1.85}_{-1.60}$	$2.01^{+0.68}_{-0.67}$	$10.87^{+2.58}_{-2.45}$

σ_v (km s^{-1})	$y_0 \times 10^4$ MS0451	Cl0016	A1835	A2261
		BIMA/OVRO		
0	$2.80^{+0.16}_{-0.21}$	$2.40^{+0.19}_{-0.21}$	$4.85^{+0.31}_{-0.31}$	$3.30^{+0.37}_{-0.40}$
500	$2.75^{+0.25}_{-0.19}$	$2.40^{+0.24}_{-0.25}$	$4.85^{+0.41}_{-0.40}$	$3.25^{+0.45}_{-0.39}$
2000	$2.70^{+0.62}_{-0.45}$	$2.25^{+0.84}_{-0.48}$	$4.65^{+1.46}_{-0.92}$	$3.15^{+0.98}_{-0.66}$
		SuZIE		
0	$3.30^{+0.30}_{-0.30}$	$1.87^{+0.86}_{-0.85}$	$8.00^{+1.14}_{-1.14}$	$6.24^{+0.85}_{-0.84}$
500	$3.22^{+0.35}_{-0.33}$	$1.88^{+0.91}_{-0.87}$	$7.97^{+1.22}_{-1.19}$	$6.33^{+1.04}_{-0.97}$
2000	$2.97^{+0.45}_{-0.44}$	$2.03^{+1.80}_{-1.13}$	$7.78^{+1.49}_{-1.41}$	$6.99^{+1.77}_{-1.60}$

Chapter 8

Measuring SZ Scaling Relations

Self-similar models of cluster formation, which include only gravity and shock heating, predict scaling relations between the electron temperature, integrated SZ flux, and central Comptonization, [see 59, 77, 24, for example]. In the self-similar model the mass and temperature of a cluster are related by $ME(z) \propto T^{3/2}$, where $E(z)^2 \equiv H(z)^2/H_0^2 = \Omega_M(1+z)^3 + (1 - \Omega_M - \Omega_\Lambda)(1+z)^2 + \Omega_\Lambda$. The factor of $E(z)$ arises from the assumption that the cluster density scales with the critical density of the Universe. Following da Silva et al. [24], the mass-temperature scaling relation can be used to relate the SZ flux, S, to the temperature

$$S d_A(z)^2 E(z) \propto T^{5/2} \tag{8.1}$$

where $d_A(z)$ is the angular diameter distance to the cluster. The factor of $d_A(z)^2$ accounts for the apparent angular size of the cluster, which changes with the cluster's redshift. The scaling of the central Comptonization with the temperature can be derived through its relation to the integrated SZ flux

$$S = \int \Delta I d\Omega \propto y_0 \int d\Omega \propto \frac{y_0}{d_A^2} \int dA \tag{8.2}$$

where dA corresponds to a physical radius such that $\int dA = \pi r^2$, where r is the radius of the cluster. The radius of the cluster can be related to the cluster mass, M, and the critical density of the universe, $\rho_{\rm crit}$, by equation 5.28, such that $r^3 \propto M/\rho_{\rm crit} \propto T^{3/2}/E(z)^3$, where we have used the mass-temperature relation

$$ME(z) \propto T^{3/2} \tag{8.3}$$

Combining this result with the SZ flux-temperature scaling relation, and the definition of the central Comptonization above, we arrive at

$$\frac{y_0}{E(z)} \propto T^{3/2} \tag{8.4}$$

as the expected scaling between the central Comptonization and the temperature of the cluster. The published temperatures that we use are spectral temperatures derived from fits to X-ray spectra. As previously mentioned, simulations by Mathiesen & Evrard [69] predict that temperatures derived from spectral fits to X-ray data would be $\sim$ 1-3keV less than the mass weighted temperature. Mathiesen & Evrard [69] calculated the effect of using the spectral temperature in place of the mass-weighted temperature in the mass-temperature scaling relation and found $ME(z) \propto T^{1.6}$. Because we are using spectral temperatures when calculating our scaling relations, we expect equations 8.1 and 8.4 to be proportionally steepened.

The predicted slopes and offsets of the above scaling relations also change from the presence of other cooling and heating processes. Heat input into the cluster gas, through sources such as radiative cooling or pre-heating, steepens the slope of the mass-temperature, X-ray luminosity-temperature, and SZ flux-temperature scaling relations [104, 24]. The steepening of the X-ray luminosity-temperature and mass-temperature relations have been observed by several authors using X-ray measurements [see 67, 38, for example]. In particular, Finoguenov et al. [38] found that $M \propto T_X^{1.78^{+0.10}_{-0.09}}$ (68%) from X-ray observations of relatively nearby ($z \lesssim 0.1$) clusters, which is significantly steeper than the self-similar predicted slope of 1.5. Little work has been done to measure SZ scaling relations due to the scarcity of SZ measurements. Cooray [20] and McCarthy et al. [74] have compiled SZ measurements from the literature, but concentrated almost entirely on relations using the central decrement, which as we have shown could be susceptible to significant systematic uncertainties.

No measurements exist of an integrated SZ flux-temperature relation. This study is also the first which use results entirely from one instrument to construct SZ scaling relations.

8.1 Definition of the Fit

To fit the following relations we perform a linear least squares regression in log space. Uncertainties for an arbitrary variable X are transformed into log space by the relation $\sigma_{log(X)} = (X^+ - X^-)/(2X) \times \log(e)$ where X^+ and X^- are the positive and negative errors, respectively, to the variable X. We perform a linear least squares regression to the generic relation $\log(Y) = A + B\log(X)$ where we determine the best-fit values of A and B by minimizing our χ^2 statistic which we define as

$$\chi^2 = \sum_{i=1}^{N} \frac{\log(Y_i) - B\log(X_i) - A}{\sigma^2_{\log(Y_i)} + (B\sigma_{\log(X_i)})^2} \tag{8.5}$$

where $\sigma_{\log(X_i)}$ and $\sigma_{\log(Y_i)}$ are the uncertainties to X_i and Y_i, respectively, transformed into log space, as defined above, for the ith cluster. The uncertainties on A and B, σ_A and σ_B, are defined in a standard way using a general definition from a linear least squares fit [see 86, for example].

8.2 $S(r_\Delta)d_A^2E(z)$–T_X

In this section we construct an integrated SZ flux, $S(r_\Delta)$, versus X-ray temperature, T_X, scaling relation, for both Δ=2500 and 500. The values we use for $S(r_{2500})$, $E(z)$, T_X, and d_A are given in Table 5.9. Where relevant, the data in Table 5.9 assumes the cooling flow corrected temperature. According to the method described in section 8.1, we fit a line to $\log[S(r_{2500})d_A(z)^2E(z)]$ versus $\log[T_X]$ whose best-fit relationship is

$$\log\left[\frac{S(r_{2500})d_A^2E(z)}{\mathrm{JyMpc}^2}\right] = (2.76 \pm 0.41) + (2.21 \pm 0.41)\log\left[\frac{T_X}{\mathrm{keV}}\right] \tag{8.6}$$

where the error bars correspond to the 68% confidence region for both the offset and slope. The χ^2 to the fit is 6.52 for 13 degrees of freedom. This low χ^2 implies that we are not seeing any sources of intrinsic scatter in the relation, and are currently limited by measurement uncertainty. Figure 8.1 plots $S(r_{2500})d_A(z)^2E(z)$ versus T_X for the entire 15 cluster sample with the best-fit line from equation 8.6 over-plotted. The best-fit slope is slightly less than the expected self similar slope of 2.5, see equation 8.1, however it is well within the 68% confidence region. X-ray measurements suggest a steeper mass-temperature relation which would also imply a steeper slope approximately between 2.7-2.9 for the integrated SZ flux-temperature relation. Our results suggest a smaller slope, however they lack the sensitivity to say anything significant regarding this difference.

It is also of interest to consider any systematic difference between the cooling flow and non-cooling flow sub-samples. In Table 8.1 we show the results of the fits to equation 8.6 if we consider the cooling flow and non-cooling flow sub-samples separately. The best-fit lines for the two sub-samples are nearly identical, and almost unchanged to the best-fit line for the entire sample. This suggests either that the presence of cooling flows make a negligible correction to the SZ flux-temperature scaling relation, or that the temperature we are using have accurately corrected for the presence of the cooling flows. We can test which is the case by re-calculating the scaling relation using the cooling-flow uncorrected temperatures. We do this by re-calculating $S(r_{2500})$, as prescribed in section 5.8.2, instead assuming the X-ray emission weighted temperatures in Table 5.1, which do not account for the cooling flow. The right panel of Figure 8.1 re-plots $S(r_{2500})d_A(z)^2E(z)$ versus T_X using the re-calculated values of $S(r_{2500})$ with these different temperatures. Comparing the left to the right panel of Figure 8.1, only the points for the cooling flow clusters are changed, with the cooling flow clusters in the right panel having generally lower electron temperatures because they do not account for their cool cooling core in their determination of the electron temperature. In Table 8.1, we give the new best-fit lines for the entire 15 cluster sample, and then the cooling flow and non-cooling flow sub-samples separately. The best-fit line which describes the cooling flow clusters is significantly changed between the cooling flow un-corrected and cooling flow corrected temperatures. This suggests

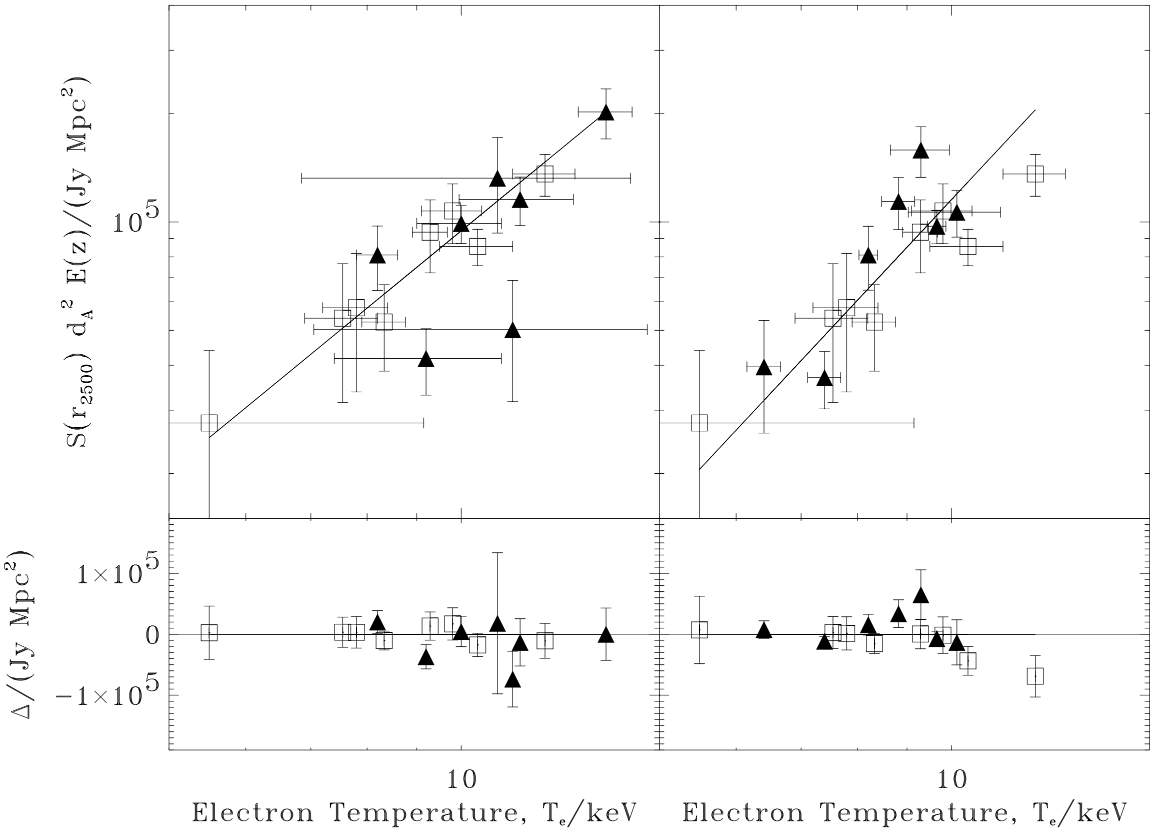

Fig. 8.1.— Left:(Top) A plot of the integrated SZ flux, as measured by SuZIE, versus the electron temperature. The solid line shows a power-law fit to the relation. Cooling flow clusters are plotted as triangles, and non-cooling flow clusters are plotted as squares. (Bottom) A plot of the residuals to the power-law fit. The uncertainty on electron temperature is not plotted, but instead is added in quadrature, according to equation 8.6, with the uncertainty to the flux density to give the uncertainty for the residual data points. Right: The same plot as on the left, except for the cooling flow clusters we use electron temperatures which do not account for the presence of the cooling flow in our calculation of $S(r_{2500})$.

that the presence of the cooling flow needs to accounted for in calculating the electron temperature in order to accurately measure the $S(r_{2500})d_A^2E(z)$–T_X scaling relation.

In Table 8.2 we give the best-fit $S(r_{500})d_A^2E(z)$–T_X relation for the cooling flow and non-cooling flow sub-samples, as well as for the entire cluster sample. The cooling flow and non-cooling flow sub-samples yield nearly identical scaling relations compared to the best-fit relationship for the entire sample. Comparing the $S(r_{500})$ relations to their $S(r_{2500})$ counterparts in Table 8.1, we see remarkable agreement between the slopes. The χ^2 of all three fits do increase, however the χ^2_{red} are still reasonable for all three relations and seem indicative of increased scatter, which we would expect at some level from increasing the integration radius. Overall, there appears to be no systematic bias in the integrated SZ flux relation by extending the integration cut-off radius to r_{500}.

8.2.1 Measuring the Evolution of the $S(r_{2500})d_A^2E(z)$–T_X Relation

The temperature of the intra-cluster gas is expected to scale with $E(z)$ based on the assumption that the density of the gas scales with the mean density of the universe. As was mentioned at the beginning of this section, this effect causes a redshift evolution in the mass-temperature relation such that $ME(z) \propto T^{3/2}$. In fact, a redshift evolution of the mass-temperature relation consistent with this prediction has been measured by Vikhlinin [105] using X-ray observations of clusters. A similar redshift evolution is expected in the SZ flux-temperature relation, such that $Sd_A(z)^2E(z) \propto T^{5/2}$, as a direct consequence of the redshift evolution in the mass-temperature relation. However, other non-gravitational physics could affect this predicted redshift evolution.

Recently da Silva et al. [24] used numerical simulations to study the evolution of the integrated SZ flux versus X-ray temperature relation when including other non-gravitational effects in clusters, such as from radiative cooling or pre-heating of the intra-cluster gas. They parameterized an arbitrary evolution by assuming that the mass-temperature relation scaled like $ME(z)^\gamma \propto T^\alpha$ and then fit for γ using simulated clusters which included either radiative cooling or pre-heating. In their simulations

Table 8.1. Fits to $\log\left[\frac{S(r_{2500})d_A^2E(z)}{\mathrm{JyMpc}^2}\right] = A + B\log\left[\frac{T_X}{\mathrm{keV}}\right]$

Sub-sample	A	B	N	χ^2	χ^2_{red} [a]
Cooling-flow Corrected Temperatures					
All	2.76 ± 0.41	2.21 ± 0.41	15	6.52	0.50
Only NCF	2.84 ± 0.72	2.13 ± 0.71	8	2.08	0.35
Only CF	2.78 ± 0.52	2.25 ± 0.50	7	4.47	0.89
Cooling-flow Un-Corrected Temperatures					
All	2.17 ± 0.52	2.89 ± 0.54	15	16.3	1.25
Only NCF	2.84 ± 0.72	2.13 ± 0.71	8	2.08	0.35
Only CF	1.70 ± 0.63	3.42 ± 0.67	7	9.15	1.83

[a] $\chi^2_{\mathrm{red}} = \chi^2/(N-2)$, where N is the number of clusters in the sub-sample.

Table 8.2. Fits to $\log\left[\frac{S(r_{500})d_A^2E(z)}{\mathrm{JyMpc}^2}\right] = A + B\log\left[\frac{T_X}{\mathrm{keV}}\right]$

Sub-sample	A	B	N	χ^2	χ^2_{red} [a]
All	3.19 ± 0.40	2.25 ± 0.40	15	15.5	1.19
Only NCF	3.23 ± 0.73	2.23 ± 0.72	8	9.07	1.51
Only CF	3.07 ± 0.53	2.34 ± 0.51	7	5.99	1.20

[a] $\chi^2_{\mathrm{red}} = \chi^2/(N-2)$, where N is the number of clusters in the sub-sample.

which included radiative cooling they calculated $\gamma = 1.49$ and in their simulations which included pre-heating instead they calculated $\gamma = 1.22$. To fit our data we adopt a similar approach to da Silva et al. [24] and fit the relation

$$\log\left[\frac{S(r_{2500})d_A^2E(z)^\gamma}{\mathrm{JyMpc}^2}\right] = A + B\log\left[\frac{T_X}{\mathrm{keV}}\right] \tag{8.7}$$

while allowing γ to be a free-parameter, where we have assumed the cooling-flow corrected electron temperature, for the cooling flow clusters, in our calculation of $S(r_{2500})$ and T_X. We calculate the χ^2 of the fit to equation 8.7 for a range of γ, letting the offset and slope, A and B, go to their best-fit values for each value of γ. We then calculate our best-fit value of γ and its associated confidence regions using a maximum likelihood estimator, where $L(\gamma) \propto \exp(-\chi^2(\gamma)/2)$. Doing this we calculate $\gamma = 1.16^{+0.84+1.28}_{-0.71-1.14}$, where the uncertainties correspond to the 68% confidence region followed by the 90% confidence region. Our results do not have sufficient sensitivity to significantly favor either of the models of da Silva et al. [24]. However, we can rule out at $\sim$ 90% confidence zero evolution to the integrated SZ flux-temperature relation; this is the first constraint of any kind on the redshift evolution of this relation. Furthermore, the redshift evolution we observe is consistent with standard theories of cluster formation ($\gamma = 1$), and offer indirect confirmation of the redshift evolution of the mass-temperature relation measured by Vikhlinin [105].

8.3 $y_0/E(z)$–T_X

In this section we construct a central Comptonization, y_0, versus X-ray temperature, T_X, scaling relation. We showed in section 6.3.4 that the central Comptonization had a significant systematic uncertainty due to the modelling of the IC gas distribution. Therefore we would expect this systematic uncertainty to make any scaling relation involving the central Comptonization suspect at best. However, it may be interesting to see how this systematic uncertainty manifests itself in a $y_0/E(z)$–T_X scaling relation.

To construct a $y_0/E(z)$–T_X scaling relation we use the central Comptonizations calculated in section 5.8.1 and the X-ray temperatures, T_X, given in Table 5.9. Where relevant, the data in Table 5.9 assumes the cooling flow corrected temperature. We fit a line to $\log(y_0/E(z))$ versus $\log(T_X/\mathrm{keV})$, according to the method described in section 8.1, whose best-fit relationship is

$$\log\left[\frac{y_0}{E(z)}\right] = (-2.35 \pm 0.57) + (2.90 \pm 0.57)\log\left[\frac{T_X}{\mathrm{keV}}\right] \tag{8.8}$$

where the error bars correspond to the 68% confidence region for both the offset and slope. The χ^2 to the fit is 38.0 for 13 degrees of freedom, with the χ^2 dominated by the contribution from A1835. Figure 8.2 plots $y_0/E(z)$ versus T_X for the entire 15 cluster sample with the best-fit line from equation 8.8 over-plotted. To check the effect of A1835 on the overall fit, we refit equation 8.8 excluding A1835, with these results given in Table 8.3. Excluding A1835 negligibly changes the best-fit values for the slope and offset while reducing the χ^2 to 15.0 for 12 degrees of freedom. This seems to indicate our fit of the y_0–T_X scaling relation is reasonable, however the best-fit slope in equation 8.8 is inconsistent with the self-similar prediction of 1.5.

If we consider the cooling flow and non-cooling flow clusters separately there is a significant systematic difference between them. In Table 8.3 we show the results of the fits to equation 8.8 if we consider the cooling flow and non-cooling flow sub-samples separately. The best-fit line to the cooling flow clusters actually favors a negative slope but is clearly poorly constrained. If we exclude A1835 from the cooling flow sample, and refit the remaining clusters, we calculate a best-fit line which is consistent with the non-cooling flow sub-sample, however the constraints on the slope are very poor. The best-fit line to the non-cooling flow sub-sample has a slope marginally consistent with the self-similar prediction. From Figure 8.2 it is clear that the cooling flow sub-sample is not well fit by a line. This is not surprising considering that in section 5.8.1 we showed that the central Comptonization has a large systematic dependence on the assumed spatial gas distribution for cooling flow clusters. The non-cooling flow sub-sample visibly gives a better fit to a line than the cooling flow sub-sample, however it is difficult to ascertain the degree of systematic uncertainty in this relation.

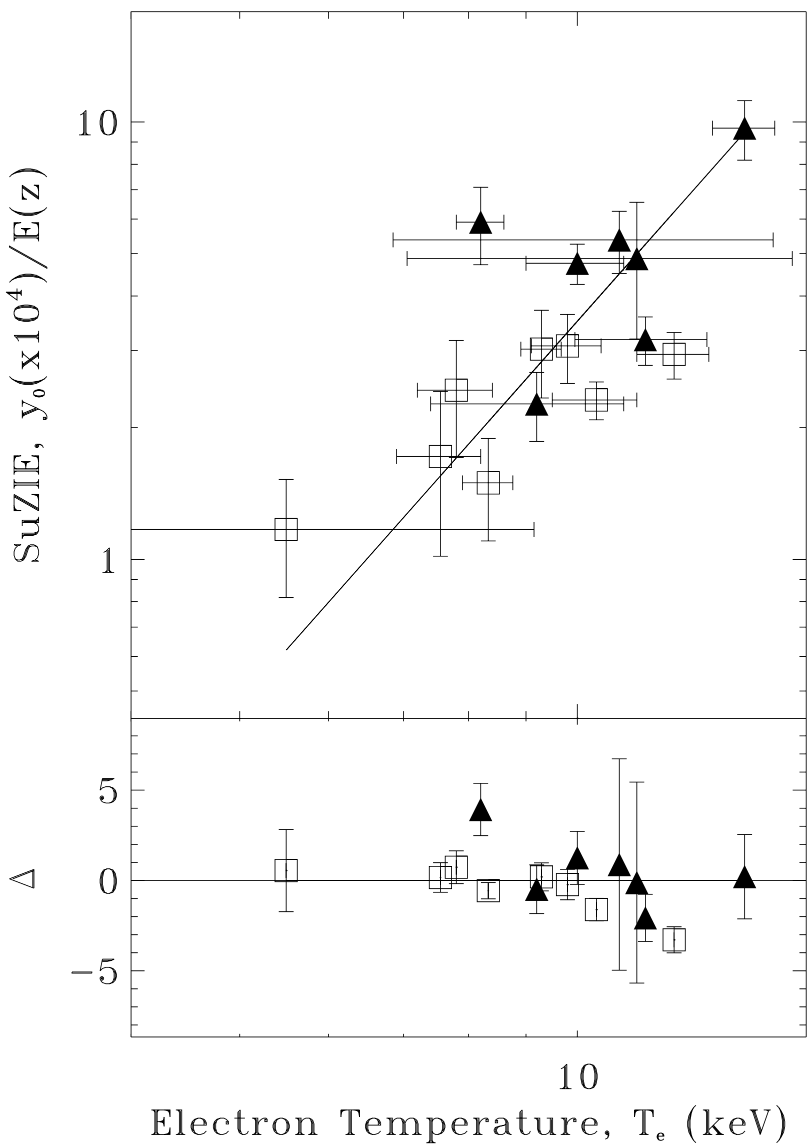

Fig. 8.2.— (Top) A plot of the central Comptonization, as measured by SuZIE, versus the electron temperature. The solid line shows a power-law fit to the relation. Cooling flow clusters are plotted as triangles, and non-cooling flow clusters are plotted as squares. (Bottom) A plot of the residuals to the power-law fit. The uncertainty on electron temperature is not plotted, but instead is added in quadrature with the uncertainty to the flux density to give the uncertainty for the residual data points.

8.4 $M(r_\Delta)E(z)$–T_X

In this section we construct a gas mass, $M(r_\Delta)$, versus X-ray temperature, T_X, scaling relation, for both Δ=2500 and 500. In general, we believe our $M(r_{2500})$ results to be less model-dependent, because r_{2500} is better matched to our beam size, however the results of section 6.3.4 seem to indicate that $M(r_{500})$ is fairly insensitive to the assumed IC gas model. At the very least, calculating the scaling relations for both values of Δ should be a useful systematic check.

The values we use for $M(r_{2500})$, $E(z)$, T_X, and d_A are given in Tables 5.10 and 5.9. Where relevant, the data in Table 5.9 assumes the cooling flow corrected temperature. According to the method described in section 8.1, we fit a line to $\log[M(r_{2500})E(z)]$ versus $\log[T_X]$ whose best-fit relationship is

$$\log\left[\frac{M(r_{2500})E(z)}{10^{13}\mathrm{M}_\odot}\right] = (-0.81 \pm 0.34) + (1.35 \pm 0.34)\log\left[\frac{T_X}{\mathrm{keV}}\right] \tag{8.9}$$

where the error bars correspond to the 68% confidence region for both the offset and slope. The χ^2 to the fit is 6.89 for 13 degrees of freedom. This low χ^2 implies that we are not seeing any sources of intrinsic scatter in the relation, and are currently limited by measurement uncertainty. Figure 8.3 plots $M(r_{2500})E(z)$ versus T_X for the entire 15 cluster sample with the best-fit line from equation 8.9 over-plotted.

In Table 8.4 we give the fits to equation 8.9 for the cooling flow and non-cooling flow sub-samples, as well as for the entire cluster sample. There is good agreement between the best-fit lines describing the two sub-samples and the best-fit line of the entire cluster sample. The best-fit slope of our entire sample is slightly less than the expected self similar slope of 1.5, see equation 8.3, however it is well within the 68% confidence region. X-ray measurements have in general measured a steeper mass-temperature relation than the self-similar prediction, $M \propto T_X^{1.74\pm0.13}$ Voevodkin et al. [106], for example, which is indicative of some form of non-gravitational heat input. This steeper slope is in agreement with the total mass-temperature scaling relation measured by Finoguenov et al. [38], $M_{\mathrm{total}} \propto T_X^{1.78^{+0.10}_{-0.09}}$. However, when only systems with $T_X > 3$ keV are considered it was found that $M_{\mathrm{total}} \propto T_X^{1.48^{+0.10}_{-0.12}}$ [38], which is

Table 8.3. Fits to $\log\left[\frac{y_0}{E(z)}\right] = A + B\log\left[\frac{T_X}{\mathrm{keV}}\right]$

Sub-sample	A	B	N	χ^2	χ^2_{red} [a]
All	-2.35 ± 0.57	2.90 ± 0.57	15	38.0	2.93
All(-A1835)	-2.45 ± 0.51	2.94 ± 0.50	14	15.0	1.25
Only NCF	-0.34 ± 0.49	0.77 ± 0.48	8	7.1	1.18
Only CF	3.55 ± 9.64	-2.88 ± 2.79	7	55.5	11.1
Only CF(-A1835)	-1.11 ± 12.8	1.52 ± 1.79	6	32.4	8.1

[a] $\chi^2_{\mathrm{red}} = \chi^2/(N-2)$, where N is the number of clusters in the sub-sample.

Table 8.4. Fits to $\log\left[\frac{M(r_{2500})E(z)}{10^{13}\mathrm{M}_\odot}\right] = A + B\log\left[\frac{T_X}{\mathrm{keV}}\right]$

Sub-sample	A	B	N	χ^2	χ^2_{red} [a]
All	-0.81 ± 0.34	1.35 ± 0.34	15	6.89	0.53
Only NCF	-0.59 ± 0.56	1.12 ± 0.54	8	0.73	0.12
Only CF	-0.88 ± 0.43	1.43 ± 0.41	7	5.69	1.14

[a] $\chi^2_{\mathrm{red}} = \chi^2/(N-2)$, where N is the number of clusters in the sub-sample.

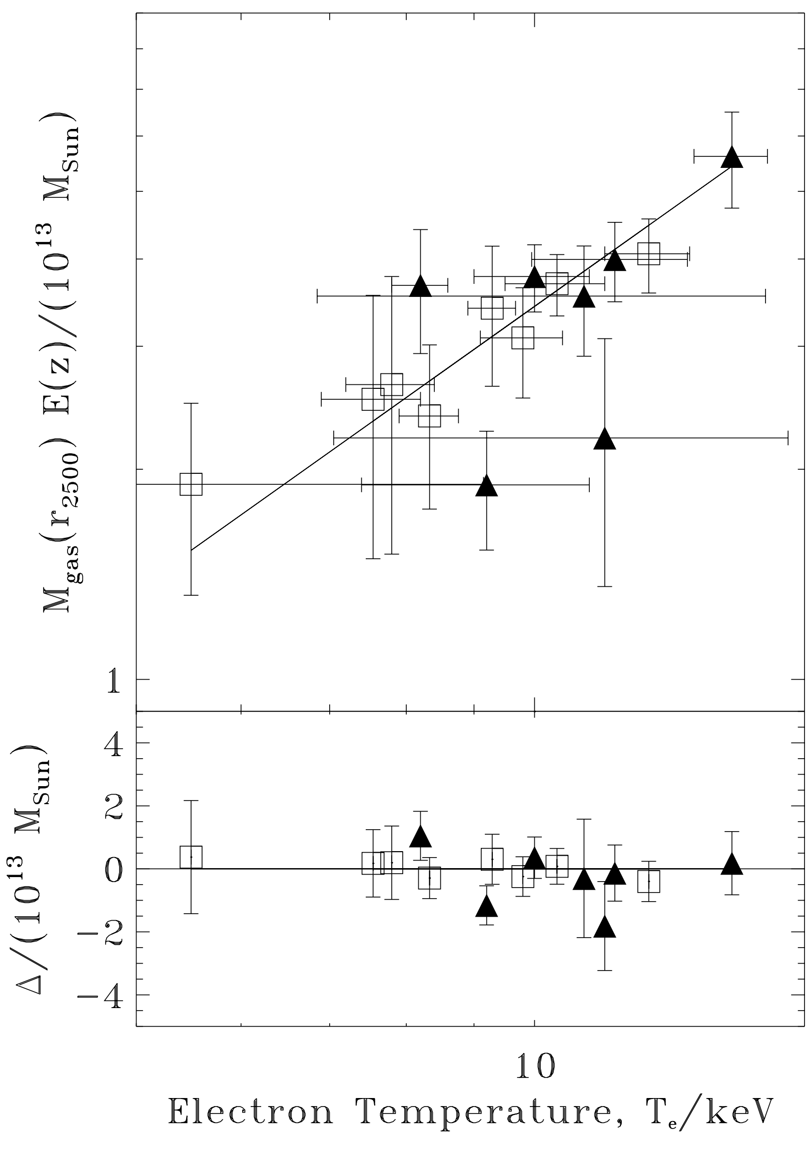

Fig. 8.3.— (Top) A plot of the gas mass, $M(r_{2500})$, versus the electron temperature. The solid line shows a power-law fit to the relation. Cooling flow clusters are plotted as triangles, and non-cooling flow clusters are plotted as squares. (Bottom) A plot of the residuals to the power-law fit. The uncertainty on electron temperature is not plotted, but instead is added in quadrature, according to equation 5.32, with the uncertainty to the gas mass to give the uncertainty for the residual data points.

more consistent with our results.

We also construct a mass-temperature relation using the values of $M(r_{500})$ given in Table 5.10. In Table 8.5 we give the best-fit relationships for our entire cluster sample, and the cooling flow and non-cooling flow sub-samples. Figure 8.4 plots $M(r_{500})E(z)$ versus T_X for the entire 15 cluster sample with the best-fit line of the entire sample, given in Table 8.5, over-plotted. In Figure 8.4 we also over-plot the gas mass versus temperature relation measured by Voevodkin et al. [106] from X-ray observations of local ($z \lesssim 0.1$) clusters. The best-fit relationship given by Voevodkin et al. [106] is

$$\log\left[\frac{M(r_{500})}{10^{13}\mathrm{M}_\odot}\right] = -0.70 + (1.74 \pm 0.13)\log\left[\frac{T_X}{\mathrm{keV}}\right] \tag{8.10}$$

where they have assumed $E(z) \sim 1$ for all their clusters, a reasonable assumption in the local Universe. While the relationship of Voevodkin et al. [106] has a significantly steeper slope than we find for our entire sample, the best-fit lines appear to reasonably agree in Figure 8.4. Somewhat more troubling is that in Table 8.5 the best-fit relationship of the cooling flow and non-cooling flow sub-samples are not consistent. The best-fit line describing the non-cooling flow sub-sample has a very flat slope, and is significantly inconsistent with the slope of the cooling flow sub-sample and the self-similar prediction.

Modelling of the intra-cluster gas is one obvious systematic which might be responsible for the above inconsistency in the $M(r_{500})$–T_X relation. While we might expect a systematic uncertainty from the spatial modelling of the IC gas to effect the $S(r_{500})$–T_X and $M(r_{500})$–T_X scaling relations somewhat equally, the integrated SZ flux should be much less sensitive to a systematic uncertainty in the electron temperature than the gas mass. Indeed, in section 8.2 we showed that extending the integration cut-off radius to r_{500} had no significant effect on the calculated integrated SZ flux scaling relations. This seems to indicate that the inconsistency observed in the $M(r_{500})$–T_X scaling relations most likely is due to a systematic uncertainty in the electron temperature. Little is known about the thermal structure in clusters past r_{2500}, however at some point towards larger radii we would expect the electron temperature to decrease. However, any explanation involving the outer regions of clusters should equally effect our cooling flow sub-sample. Possibly of note, is that our non-cooling flow clusters tend to use ASCA temperature measurements more so than our cooling flow clusters. If these measurements tended to over-estimate the electron temperature it would bias our M-T relation in the observed way, because an over-estimate of the temperature also biases our mass measurements lower. Of our cooling flow clusters, only A2204, A2261, and Zw3146 use ASCA determined temperatures. Suspiciously, A2204 and Zw3146 are the clusters in Figure 8.4 which lie significantly below the best-fit $M(r_{500})$–T_X relation. Unfortunately, a definitive explanation for the discrepancy in the $M(r_{500})$–T_X relation would most-likely require a joint analysis with X-ray observations, which is beyond the scope of this thesis. Regardless, it seems likely that a systematic uncertainty in the electron temperature is at least partially responsible for the observed inconsistency in the $M(r_{500})$–T_X relation for the cooling flow and non-cooling flow sub-samples.

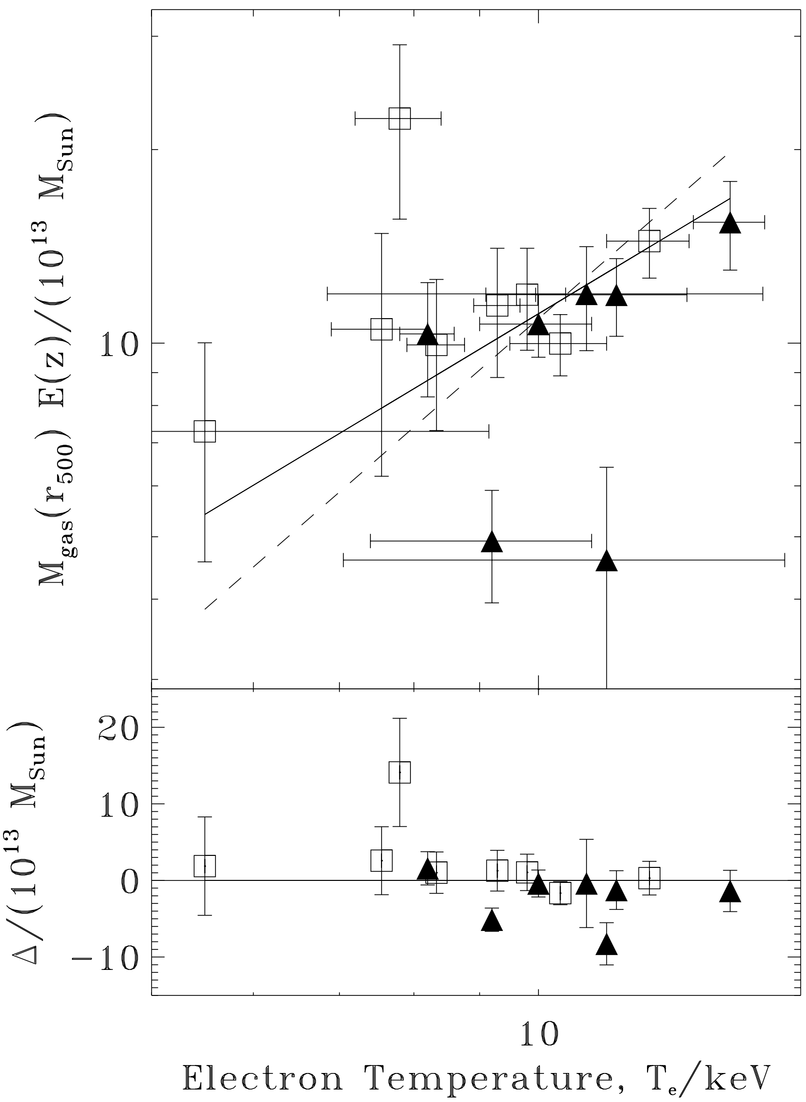

Fig. 8.4.— (Top) A plot of the gas mass, $M(r_{500})$, versus the electron temperature. The solid line shows a power-law fit to the relation. Cooling flow clusters are plotted as triangles, and non-cooling flow clusters are plotted as squares. The dashed line shows the scaling relation given in Voevodkin et al. [106] determined from X-ray observations. (Bottom) A plot of the residuals to the power-law fit. The uncertainty on electron temperature is not plotted, but instead is added in quadrature, according to equation 5.32, with the uncertainty to the gas mass to give the uncertainty for the residual data points.

Table 8.5. Fits to $\log\left[\frac{M(r_{500})E(z)}{10^{13}\mathrm{M}_\odot}\right] = A + B\log\left[\frac{T_X}{\mathrm{keV}}\right]$

Sub-sample	A	B	N	χ^2	χ^2_{red} [a]
		Cooling-flow Corrected Temperatures			
All	-0.16 ± 0.30	1.20 ± 0.30	15	21.6	1.67
Only NCF	0.52 ± 0.43	0.55 ± 0.42	8	9.60	1.60
Only CF	-0.54 ± 0.43	1.54 ± 0.41	7	7.38	1.48

[a] $\chi^2_{\mathrm{red}} = \chi^2/(N-2)$, where N is the number of clusters in the sub-sample.

Chapter 9

Checking for Convergence of the Local Dipole Flow

Table 9.1 summarizes the current sample of SuZIE II measurements of peculiar velocities and includes two previous measurements made with SuZIE I of A2163 and A1689 [52]. Note that in each case we have assumed the statistical uncertainty associated with each measurement, then added in quadrature an extra uncertainty of $\pm 750\,\mathrm{km\,s^{-1}}$ to account for the effects of astrophysical confusion from the CMB and submm point sources, based on the estimates derived in section 6.4. These confusion estimates are larger than presented in Holzapfel et al. [52], mainly because of the more recent data on submm sources. Consequently we use values for the peculiar velocities of A2163 and A1689 that have uncertainties that are somewhat higher than those previously published.

The locations of the clusters on the sky are shown in Figure 9.1. The figure also shows the precision on the radial component of each cluster peculiar velocity, plotted against the redshift of the cluster. The cross-hatched region shows the region of redshift space that has been probed by existing optical surveys (see below). We now use this sample of cluster peculiar velocities to set limits to the dipole flow at these redshifts. The clusters in the SuZIE II sample all lie at distances $\gtrsim 430h^{-1}$ Mpc, where the flow is expected to be $\lesssim 50$ km s^{-1} (see below). Of this sample, we have taken the 10 that lie in the range $z = 0.15$–0.29 and used them to set limits on the

Table 9.1. The SuZIE sample of peculiar velocity measurements

	Redshift	Peculiar Velocity (km s^{-1})[a]	Galactic Coordinates l (deg.)	b (deg.)	Distance[b] (h^{-1} Mpc)
A2204	0.15	-1100^{+1100}_{-775}	21.09	33.25	430
A1689	0.18	$+170^{+805}_{-600}$	313.39	61.10	520
A2163	0.20	$+490^{+1310}_{-790}$	6.75	30.52	570
A520	0.20	-1700^{+1450}_{-1375}	195.80	-24.28	570
A773	0.22	-1175^{+2875}_{-1625}	166.11	43.39	630
A2261	0.22	-1575^{+1500}_{-975}	55.61	31.86	630
A2390	0.23	-175^{+1050}_{-900}	73.93	-27.83	650
A1835	0.25	-175^{+1675}_{-1275}	340.38	60.59	710
A697	0.28	-1625^{+1075}_{-825}	186.39	37.25	785
ZW3146	0.29	-400^{+3700}_{-1925}	239.39	47.96	810

[a]Statistical uncertainties only. An additional systematic uncertainty of $\pm 750\,\mathrm{km\,s^{-1}}$ is assumed for the bulk flow analysis.

[b]For a $\Omega_m = 0.3$, $\Omega_\Lambda = 0.7$ cosmology

dipole flow of structure at this redshift. This calculation gives a useful indication of the abilities of SZ measurements to probe large-scales motions and is also the first time that such a measurement has been made using SZ results.

Flows that are coherent over large regions of space probe the longest wavelength modes of the gravitational potential and provide a test of matter formation and evolution in the linear region. The average bulk velocity, V_B, of a region of radius, R, is predicted to be:

$$\left\langle V_B^2(R) \right\rangle = \frac{H_0^2 \Omega_m^{1.2}}{2\pi^2} \int_0^\infty P(k) \tilde{W}^2(kR) dk \tag{9.1}$$

[see 100, for example], where Ω_m is the present-day matter density, H_0 is the Hubble constant, $P(k)$ is the matter power spectrum and $\tilde{W}(kR)$ is the Fourier transform of the window function of the cluster sample. The shape of the window functions depends on details of the cluster sample such as whether all of the sphere is sampled, or whether the clusters lie in a redshift shell [109]. In all models the flow is expected to converge as a function of increasing R and at $z \geq 0.15$ it should be less than $50\,\mathrm{km\,s^{-1}}$. Of course, equation (9.1) is strictly valid only in the local universe. At higher redshifts, the rate of growth of fluctuations must be accounted for, causing the expected bulk flow to decrease even more quickly.

All measurements of bulk flows to date have used peculiar velocities of galaxies, determined by measuring the galaxy redshift and comparing it to the distance determined using a distance indicator based on galaxy luminosities, rotational velocities, or Type Ia supernovae. These methods have yielded bulk flows consistent with theory out to a distance of $60h^{-1}$ Mpc [see 21, for reviews of the experimental situation]. At larger distances, the situation is less clear. Some null measurements do seem to confirm that the flow converges [19, 25], but there are a number of significantly larger flow measurements that have not yet been refuted and that are quite discrepant with one another in direction [109, 56, 64]. The directions of these flows are shown in Table 9.2.

We define a bulk flow as $\mathbf{V}_\mathrm{B} = (V_B, l_B, b_B)$ where V_B is the velocity of the bulk flow, l_B is the galactic longitude and b_B is the galactic latitude of the flow direction.

We can then calculate the likelihood of these parameters as:

$$L(\mathbf{V}_{\mathrm{B}}) = \prod_i L_i(\mathbf{V}_{\mathrm{B}}.\hat{r}_i) \tag{9.2}$$

where $\mathbf{V}_{\mathrm{B}}.\hat{r}$ is the component of the bulk flow in the direction of the ith cluster, and the likelihood of the flow, given the data, L_i, is determined from the SuZIE II data. In order to account for the effects of astrophysical confusion, we convolve the likelihood function for the peculiar velocity of each cluster with a gaussian probability with $\sigma = \pm 750\,\mathrm{km\,s^{-1}}$ before calculating the bulk-flow likelihood. As expected, we do not detect any bulk flow in our data. Figure 9.2 shows the 95% confidence limit to V_{B} as a function of location on the sky.

Because our clusters sparsely sample the peculiar velocity field, our upper limits are tighter in some directions than in others. For example, we have also used our data to set limits on bulk flows in the direction of the CMB dipole which is taken to have coordinates $(l, b) = (276° \pm 3°, 33° \pm 3°)$ [61]. We find that at 95% confidence the flow in this direction is $\leq 1260\,\mathrm{km\,s^{-1}}$. The limits towards other directions for which optical measurements have yielded a flow detection are shown in Table 9.2.

Table 9.2. Limits to bulk flows in specific directions.

	Direction (Gal.)		Velocity (km s^{-1})		
Flow name	l (deg.)	b (deg.)	Best Fit	95% conf. limit	Ref.
CMB Dipole	276	+33	-100 ± 620	1260	1
ACIF	343	+52	-180 ± 520	1080	2
LP10K	272	+10	$+140 \pm 820$	1620	3
SMAC	260	+1	280 ± 880	1680	4

References. — (1) Kogut et al. [61], (2) Lauer & Postman [64], (3) Willick [109], (4) Hudson et al. [56]

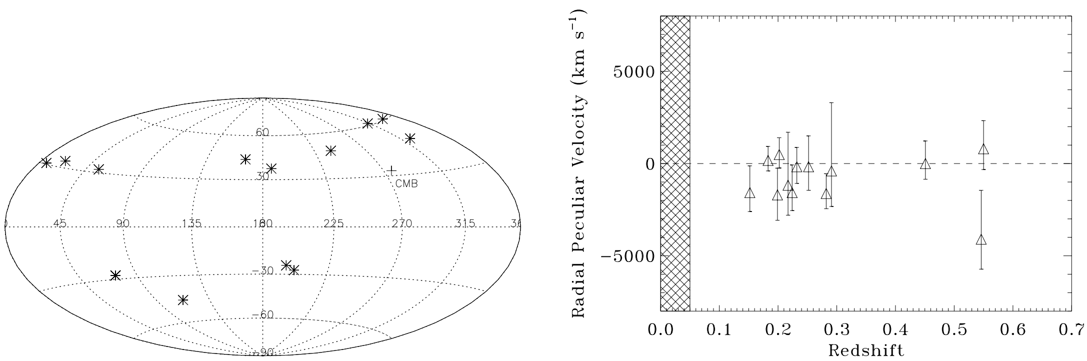

Fig. 9.1.— Left: the stars denote the location, in galactic coordinates, of the clusters observed by SuZIE. The direction of the CMB dipole is also shown. Right: the measurements of the clusters plotted against redshift. The cross-hatched region shows the range that has been probed using optical measurements of peculiar velocities.

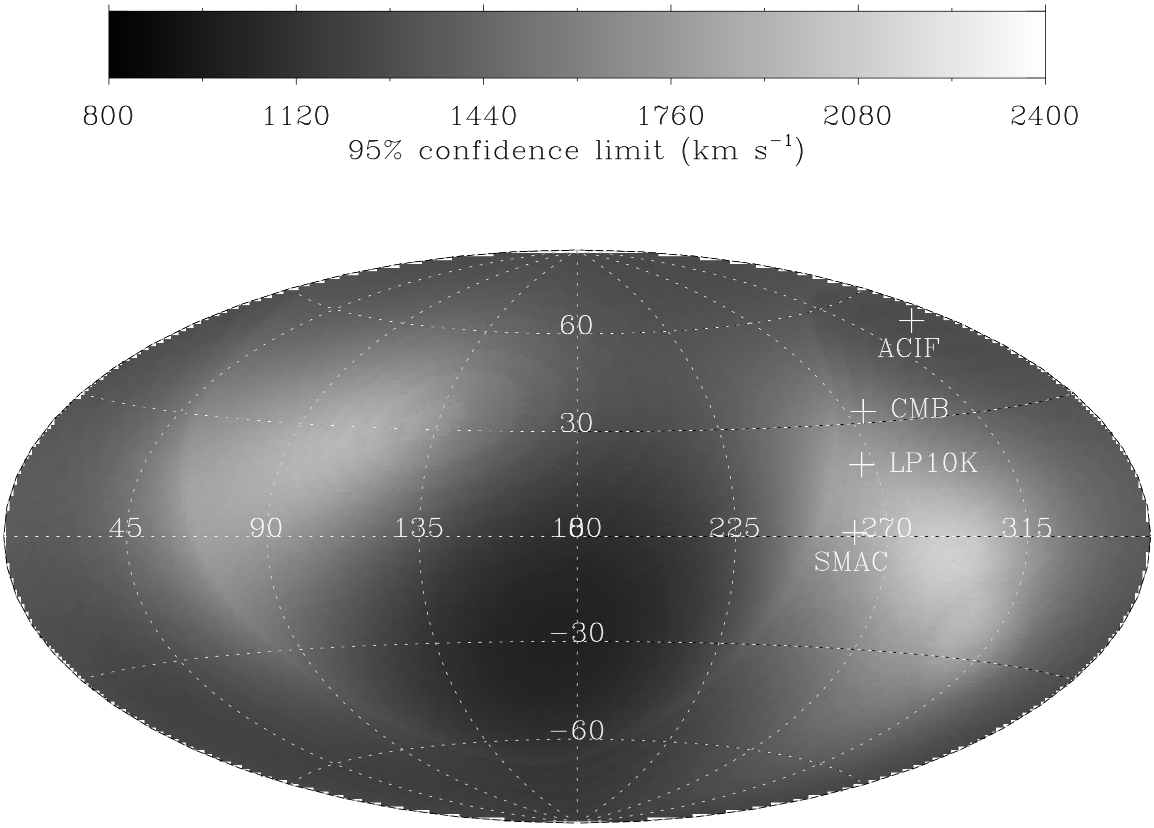

Fig. 9.2.— All-sky map showing the upper limit to dipole flow (95% confidence) as a function of location on the sky. The locations of the flows listed in Table 9.2 are also shown.

Chapter 10

Conclusions

10.1 Summary

We have used millimetric measurements of the SZ effect to set limits to the peculiar velocities of eleven galaxy clusters. By making measurements at three widely separated frequencies we have been able to separate the thermal and kinematic SZ spectra. Moreover, because our measurements in these bands are simultaneous, we have been able to discriminate and remove fluctuations in atmospheric emission which dominate the noise at these wavelengths. These observations have allowed us to make the first SZ-determined limits on bulk flows. In certain directions the limits are approaching the level of sensitivity achieved with optical surveys at much lower redshifts. Because our sky coverage is not uniform, our sensitivity to bulk flows varies greatly over the sky.

The precision with which SuZIE II can measure peculiar velocities is limited not only by the small number of detectors, but also by atmospheric and instrumental noise, and astrophysical confusion from submillimeter galaxies. In the last few years the potential of SZ astronomy has been realized and new telescopes equipped with bolometer arrays that will have hundreds to thousands of pixels are planned [13, 99]. Our measurements demonstrate the feasibility of using the SZ effect to measure cluster peculiar velocities, but highlight some issues that need further investigation:

1. The atmosphere will continue to be an issue for ground-based measurements.

We have demonstrated that wide, simultaneous spectral coverage can significantly diminish, but not completely remove, this source of noise.

2. Confusion from submillimeter point sources can lead to a systematic peculiar velocity measurement. Further work is needed to determine the best strategy for identifying and removing this contaminant, especially for experiments that will map a large area of sky with lower angular resolution than SuZIE II, such as the High Frequency Instrument (HFI) that will operate at frequencies of 100–850 GHz as part of the Planck satellite [62]. Although high-resolution measurements of clusters at millimeter wavelengths will be possible with future instruments such as ALMA, it may not be feasible to use this method to subtract astrophysical contamination from a sample of the size needed (of order 1000+ velocities) to effectively probe large-scale structure with SZ-determined peculiar velocities. Instruments such as SuZIE II will be invaluable for investigating removal techniques based on spectral rather than spatial information, especially if more frequency bands are incorporated into the instrument.

We have combined the SuZIE II measurements with previous cluster observations with SuZIE I to construct a sample of 15 clusters of galaxies for which we have measured the SZ thermal effect towards each cluster. For this set of clusters we use the 145 GHz frequency band to calculate a central Comptonization, y_0, an integrated SZ flux, $S(r_\Delta)$, and a gas mass, $M(r_\Delta)$.

We find that the calculated central Comptonization is much more sensitive to the assumed spatial model for the intra-cluster gas than either the calculated integrated SZ flux or gas mass. The calculated central decrement depends significantly on the assumed spatial distribution of the intra-cluster (IC) gas. For the case of A1835 the calculated central Comptonization can vary by a factor of two depending on which of two different published IC gas models is assumed. This result is not surprising considering the fact that SuZIE II does not significantly resolve any of the observed clusters. This effect causes the calculated central Comptonization to have a particularly large systematic uncertainty in cooling flow clusters because of their large cooling core which makes the standard Beta model an inadequate fit to the spatial distribution of the gas. However, our measurements of the integrated SZ flux, $S(r_\Delta)$, and gas mass, $M(r_\Delta)$, depend much less sensitively on the assumed spatial distribution of the IC gas. This is especially true for Δ=2500 because r_{2500} is well-matched to our beam-size for most of the observed clusters.

Ten of the clusters in our sample overlap with published measurements from the BIMA and OVRO interferometers. For these clusters, we compare the calculated central Comptonization from BIMA and OVRO to those from SuZIE and find that the SuZIE calculated central Comptonizations are generally higher, significantly so in the cooling flow clusters. If we compare the SuZIE 145 GHz results to the BIMA and OVRO results, SuZIE measures a central Comptonization $\sim 12\%$ higher in the non-cooling flow clusters, and $\sim 60\%$ higher in the cooling flow clusters. We attribute this difference to the large systematic uncertainty in the calculated central Comptonization from the assumed intra-cluster gas model which, as expected, is more pronounced in our cooling flow sub-sample.

We use the central Comptonization and integrated SZ flux results from the SuZIE 145 GHz data to construct SZ scaling relations with the X-ray temperature, T_X. We construct a y_0–T_X scaling relation and find a slope significantly different than that expected for self-similar clusters. However, we believe that this result is questionable because of the large systematic uncertainty in the central Comptonization. This conclusion is supported by the significantly discrepant scaling relations derived for the cooling flow and non-cooling flow sub-samples. We also construct a $M(r_{2500})$–T_X scaling relation and find a slope consistent with the expectation for self-similar clusters. Extending our gas mass calculations to r_{500}, we calculate the $M(r_{500})$–T_X scaling relation and find a significant disagreement between the slopes of the cooling flow and non-cooling flow sub-samples. This disagreement was not present in the $M(r_{2500})$–T_X scaling relation. We believe it to be in part due to our assumption of an isothermal IC gas which may be less accurate at larger radii. For the $S(r_{2500})$–T_X scaling relation we find a slope which is consistent with the expectation for self-similar clusters. In constructing this relation, we find that using X-ray temperatures which do not account for the presence of the cooling flow significantly biases the best-fit relation. We detect a redshift evolution of the $S(r_{2500})$–T_X scaling relation consistent with standard cluster formation theory for which the density of the cluster scales with the critical density of the universe. If we assume that the X-ray temperature is a good indicator of the mass of the cluster, as suggested from X-ray measurements, our results imply that the integrated SZ flux will be a good indicator of the cluster mass as well, a promising result for future SZ cluster surveys.

10.2 Future Directions: SuZIE III

Observations with SuZIE II are limited by the raw sensitivity of the instrument, see Figure 3.10. However, there are several ways to improve the sensitivity of the current instrument:

1. Increased optical efficiency: The photometers in SuZIE II have proven very convenient in separating light of different frequencies, however they suffer from very poor optical efficiency. The current optical efficiency of the 145 GHz band in SuZIE II is $\sim 13\%$ while the previous version of the SuZIE instrument, SuZIE I, had an optical efficiency of $\sim 34\%$ [53]. By redesigning the focal plane to instead consist of a sequence of mirrors and lenses, we would expect to improve the optical efficiency at least to the levels of SuZIE I. Similar, but more recent, bolometer based receivers have achieved $\sim 40\%$ optical efficiency [93].

2. Increased bandwidth: The current SuZIE II frequency bands do not make very efficient use of the atmospheric windows on Mauna Kea, see Figure 3.5. Advances in filter technology allow wider frequency bands. The 145 and 221 GHz bands could be increased by a factor of two times the current SuZIE II band-width.

3. An additional frequency channel: Also obvious in Figure 3.5 is a significant gap in our frequency coverage between $\sim$ 250–300 GHz. Redesigning the focal plane to include a fourth frequency band at $\sim$280 GHz would help us fill in our frequency coverage.

4. Placement of all pixels on source: The current SuZIE II design allows only two of the four photometers to scan directly over the cluster center, with the other two observing $\sim$140 arcsec off-source. By simply placing the detectors in the off-source row in the on-source row, we are effectively doubling the number of detectors on-source.

The next generation upgrade, SuZIE III, is currently being built at Stanford University based on the above changes. The initial upgrade will use the existing spider-web bolometers in SuZIE II, however plans exist to eventually upgrade to large format bolometer arrays. Even with the current redesign, SuZIE III should represent a significant improvement in sensitivity over SuZIE II, see Table 10.1. For example, in our 145 GHz band we expect a factor of ~ 6 improvement in the noise equivalent flux density (NEFD) per pixel over SuZIE II.

Table 10.1. Sensitivity per Pixel of SuZIE III

Channel [GHz]	θ_{res} [arcmin]	NEP$_\gamma$ [10^{-17} W/$\sqrt{Hz}$]	NEP$_{\mathrm{bolo}}$ [10^{-17} W/$\sqrt{Hz}$]	NEFD [mJy/$\sqrt{Hz}$]
SuZIE III				
145	1.0	21.6	6.8	17
221	1.0	49.3	8.9	28
280	1.0	63.6	12.5	35
355	1.0	324.4	33.5	223
SuZIE II				
145	1.54	5.8	6.8	98
221	1.40	16.8	8.9	94
280	···	···	···	···
355	1.60	248.3	33.5	577

Appendix A

Creating an Atmospheric Template

SuZIE makes simultaneous multi-frequency observations of a source. Besides the obvious advantage of instantaneously measuring the spectrum of the SZ source, this method permits atmospheric noise removal through spectral discrimination of the atmospheric signal. We realize this by creating an atmospheric template with no residual SZ signal for each row of photometers by forming a linear combination of the three differential frequency channels in that row on a scan by scan basis. We define this atmospheric template, $A_j(\theta)$, as:

$$A_j(\theta) = \alpha D_{1j}(\theta) + \gamma D_{2j}(\theta) + D_{3j}(\theta) \tag{A.1}$$

where the coefficients α and γ, are chosen to minimize the residual SZ signal in $A_j(\theta)$. If we define $F_k^{SZ}(\theta)$ as the SZ signal in channel $D_k(\theta)$ this implies that the residual SZ signal in our atmospheric template, which we define as $Z_k^{SZ}(\theta)$, is then

$$Z_k^{SZ}(\theta) = \alpha F_1^{SZ}(\theta) + \gamma F_2^{SZ}(\theta) + F_3^{SZ}(\theta) \tag{A.2}$$

where the SZ flux in each channel includes contributions for both the thermal and kinematic effects, such that, $F_k^{SZ}(\theta) = F_k^{SZ,T}(\theta) + F_k^{SZ,K}(\theta)$. The thermal SZ flux in each channel, using the notation of §5.2, is more precisely:

$$F_k^{SZ,T}(\theta) = y_0 \times T_k(T_e) \times m_k(\theta) \tag{A.3}$$

with y_0 being the central comptonization of the cluster, $T_k(T_e)$ being defined in equation (5.4), and $m_k(\theta)$ defined in equation (5.3). Similarly, the kinematic SZ flux in each channel is

$$F_k^{SZ,K}(\theta) = y_0 v_p \times K_k(T_e) \times m_k(\theta) \tag{A.4}$$

with v_p being the peculiar velocity of the cluster, and $K_k(T_e)$ defined in equation (5.5).

Using this notation we rewrite our expression for the residual SZ signal in the atmospheric template as

$$Z_k^{SZ}(\theta) = Z_k^T(\theta) + Z_k^K(\theta) \tag{A.5}$$

with:

$$Z_k^T(\theta) = y_0 \left[\alpha T_1(T_e) m_1(\theta) + \gamma T_2(T_e) m_2(\theta) + T_3(T_e) m_3(\theta)\right] \tag{A.6}$$

$$Z_k^K(\theta) = -y_0 v_p \left[\alpha K_1(T_e) m_1(\theta) + \gamma K_2(T_e) m_2(\theta) + K_3(T_e) m_3(\theta)\right] \tag{A.7}$$

Solving for $Z_k^{SZ}(\theta) = 0$ requires a position-dependent solution for α and γ because $m_k(\theta)$ is not constant between frequency bands. For simplicity, we use the peak values of $m_k(\theta)$ to calculate α and γ for $Z_k^{SZ} = 0$. The error introduced from this assumption is discussed in Section 6.3.2. As an aside, this template should also be free of primary CMB anisotropy, on spatial scales similar to our clusters, because the kinematic SZ effect is spectrally indistinguishable from a primary CMB anisotropy.

REFERENCES

[1]Allen, S.W., & Fabian, A.C., 1998, MNRAS, 297, L57

[2]Allen, S.W., 2000, MNRAS, 315, 269

[3]Allen, S.W., Ettori, S., & Fabian, A.C. 2001, MNRAS, 324, 877

[4]Alpher, R.A., Behter, H., & Gamow, G. 1948, *Rev. Mod. Phys.*, 73, 803

[5]Archibald, E. N., Jenness, T., Holland, W. S., Coulson, I. M., Jessop, N. E., Stevens, J. A., Robson, E. I., Tilanus, R. P. J., Duncan, W. D., Lightfoot, J. F. 2002, MNRAS, 336, 1

[6]Battistelli, E.S., De Petris, M., Lamagna, L., Melchiorri, F., Palladino, E., Savini, G., Cooray, A., Melchiorri, A., Rephaeli, Y., & Shimon, M. 2002, ApJ, 580, L101

[7]Bennett, C.L., Banday, A., Gorski, K.M., Hinshaw, G., Jackson, P., Keegstra, P., Kogut, A., Smoot, G.F., Wilkinson, D.T., Wright, E.L. 1996, ApJ, 464, L1

[8]Bennett, C.L., et al. 2003, ApJS, 148, 1

[9]Benson, B.A., Church, S.E., Ade, P.A.R., Bock, J.J., Ganga, K.M., Hinderks, J.R., Mauskopf, P.D., Philhour, B., Runyan, M.C., & Thompson, K.L. 2003, ApJ, 592, 674

[10]Blain, A. W., 1998, MNRAS, 297, 502

[11]Branchini, E., Zehavi, I., Plionis, M., & Dekel, A. 2000, MNRAS, 313, 491

[12]Bridle, S. L., Zehavi, I., Dekel, A., Lahav, O., Hobson, M. P., & Lasenby, A. N. 2001, MNRAS, 321, 333

[13]Carlstrom, J. E., Holder, G.P., & Reese, E.D. 2002, ARA&A, 40 in press

[14]Cavaliere, A. & Fusco-Femiano, R. 1976, A&A, 49, 137

[15]Cavaliere, A. & Fusco-Femiano, R. 1978, A&A, 70, 677

[16]Challinor, A., & Lasenby, A., 1998, ApJ, 499, 1

[17]Chapman, S.C., Scott, D., Borys, C., & Fahlman, G.G., 2002, MNRAS, 330, 92

[18]Church, S.E., & Benson, B.A., in prep

[19]Colless, M., Saglia, R. P., Burstein, D., Davies, R. L., McMahan, R. K., & Wegner, G. 2001, MNRAS, 321, 277

[20]Cooray, A. 1999, MNRAS, 307, 841

[21]Courteau, S. & Dekel, A. 2001, ASP Conf. Ser. 245: Astrophysical Ages and Times Scales, 584

[22]Courteau, S., Willick, J. A., Strauss, M. A., Schlegel, D., & Postman, M. 2000, ASP Conf. Ser. 201: Cosmic Flows Workshop, 17

[23]Crill, B.P. 2001, PhD Thesis, California Institute of Technology

[24]da Silva, A.C., Kay, S.T., Liddle, A.R., & Thomas, P.A., 2003, astro-ph/0308074

[25]Dale, D. A. & Giovanelli, R. 2000, ASP Conf. Ser. 201: Cosmic Flows Workshop, 25

[26]David, L. P., Slyz, A., Jones, C., Forman, W., & Vrtilek, S. D. 1993, ApJ, 412, 479

[27]De Petris, M., D Alba, L., Lamagna, L., Melchiorri, F., Orlando, A., Palladino, E., Rephaeli, Y., Colafrancesco, S., Kreysa, E., Signore, M. 2002, ApJ, 574, L119

[28]Dicke, R.H., Peebles, P.J.E., Roll, P.G., & Wilkinson, D.T. 1965, ApJ, 142, 414

[29]Dolgov, A. D., Hansen, S. H., Pastor, S., & Semikoz, D. V. 2001, ApJ, 554, 74

[30]Donahue, M., 1996, ApJ, 468, 79

[31]Doré, O., Knox, L., Peel, A. 2003, ApJ, 585, L81

[32]Dupke, R. A. & Bergman, J. N. 2002, ApJ, 575, 634

[33]Ebeling, H., Voges, W., Bohringer, H., Edge, A. C., Huchra, J. P., & Briel, U. G. 1996a, MNRAS, 281, 799

[34]Ebeling, H., Voges, W., Bohringer, H., Edge, A. C., Huchra, J. P., & Briel, U. G. 1996b, MNRAS, 283, 1103

[35]Ebeling, H., Edge, A. C., Bohringer, H., Allen, S. W., Crawford, C. S., Fabian, A. C., Voges, W., & Huchra, J. P. 1998, MNRAS, 301, 881

[36]Ettori, S., & Fabian, A.C., MNRAS, 305, 834

[37]Evrard, A.E., Metzler, C.A., & Navarro, J.F. 1996, ApJ, 469, 494

[38]Finoguenov, A., Reiprich, T.H., & Bohringer, H. 2001, A&A, 368, 749

[39]Fixsen, D.J., Cheng, E.S., Gales, J.M., Mather, J.C., Shafer, R.A., Wright, E.L. 1996, ApJ, 473, 576

[40]Gamow, G. 1946, *Phys. Rev.*, 70, 527

[41]Ganga, K. M., Ratra, B., Church, S. E., Sugiyama, N., Ade, P. A. R., Holzapfel, W. L., Mauskopf, P. D., Wilbanks, T. M., and Lange, A. E. 1997, ApJ, 484, 517

[42]Gioia, I. M., Maccacaro, T., Schild, R. E., Wolter, A., Stocke, J. T., Morris, S. L., & Henry, J. P. 1990, ApJS, 72, 567

[43]Gioia, I. M. & Luppino, G. A. 1994, ApJS, 94, 583

[44]Goldin, A.B., Kowitt, M.S., Cheng, E.S., Cottingham, D.A., Fixsen, D.J., Inman, C.A., Meyer, S.S., Puchalla, J.L., Ruhl, J.E., and Silverberg, R.F. 1997, ApJ, 488, L161

[45]Gramann, M., Bahcall, N. A., Cen, R., & Gott, J. R. 1995, ApJ, 441, 449

[46]Grego , L., Carlstrom , J. E., Reese, E. D., Holder , G. P., Holzapfel, W. L., Joy, M. K., Mohr, J. J., & Patel, S. 2001, ApJ, 552, 2

[47]Griffin, M.J., & Orton, G.S. 1993, Icarus, 105, 537

[48]Haiman, Z., Mohr, J.J., & Holder, G.P., 2001, ApJ, 553, 545

[49]Hansen, S. H., Pastor, S. & Semikoz, D. V. 2002, ApJ, 573, L69

[50]Holder, G.P., Haiman, Z., & Mohr, J.J., 2001, ApJ, L111

[51]Holzapfel, W.L., Arnaud, M., Ade, P.A.R., Church, S.E., Fischer, M.L., Mauskopf, P.D., Rephaeli, Y., Wilbanks, T.M., and Lange, A.E. 1997a, ApJ, 480, 449

[52]Holzapfel, W.L., Ade, P.A.R., Church, S.E., Mauskopf, P.D., Rephaeli, Y., Wilbanks, T.M., and Lange, A.E. 1997b, ApJ, 481, 35

[53]Holzapfel, W.L., 1996, PhD Thesis, UC-Berkeley.

[54]Hubble, E. 1929, PNAS, 15, 168H

[55]Hughes, J.P., & Birkinshaw, M., 1998, ApJ, 501, 1

[56]Hudson, M. J., Smith, R. J., Lucey, J. R., Schlegel, D. J., & Davies, R. L. 1999, ApJ, 512, L79

[57]Itoh, N., Kohyama, Y., & Nozawa, S., 1998, ApJ, 502, 7

[58]Jones, M. E., Edge, A C., Grainge, K., Grainger, W. F., Kneissl, R., Pooley, G. G., Saunders, R., Miyoshi, S. J., Tsuruta, T., Yamashita, K., Tawara, Y., Furuzawa, A., Harada, A., Hatsukade, I. 2001, MNRAS, submitted, (astro-ph/0103046)

[59]Kaiser, N., 1986, MNRAS, 222, 323

[60]Kompaneets, A.S., 1957, Soviet Physics JETP Lett, 4, 730

[61]Kogut, A., et al. 1993, ApJ, 419, 1

[62]Lamarre, J. M. et al. 2000, Astrophysical Letters Communications, 37, 161

[63]LaRoque, S.L., Carlstrom, J.E., Reese, E.D., Holder, G.P., Holzapfel, W.L., Joy, M., and Grego, L. 2002, ApJ, submitted (astro-ph/0204134)

[64]Lauer, T. R. & Postman, M. 1994, ApJ, 425, 418

[65]Majerowicz, S., Neumann, D.M., & Reiprich, T.H. 2002, A&A, 394, 77

[66]Markevitch, M., Mushotzky, R., Inoue, H., Yamashita, K., Furuzawa, A.,& Tawara, Y. 1996, ApJ, 456, 437

[67]Markevitch, M. 1998, ApJ, 504, 27

[68]Markevitch, M., Gonzalez, A. H., Clowe., D., Vikhlinin, A., David, L., Forman, W., Jones, C., Murray, S., & Tucker, W. 2003, ApJ, submitted, astroph/0309303

[69]Mathiesen, B.F. & Evrard, A.E. 2001, ApJ, 546, 100

[70]Mather, J.C., *Applied Optics*, Vol. 23, 3181

[71]Mauskopf, P.D., Ade, P.A.R., Allen, S.W., Church, S.E., Edge, A.C., Ganga, K.M., Holzapfel, W.L., Lange, A.E., Rownd, B.K., Philhour, B.J., and Runyan, M.C. 2000, ApJ, 538, 505

[72]Mauskopf, P.D., Bock, J.J., Del Castillo, H., Holzapfel, W.L., & Lange, A.E., 1997, *Applied Optics*, Vol. 36, No. 4, 765

[73]Mauskopf, P.D., 1997, PhD Thesis, UC-Berkeley

[74]McCarthy, I. G., Holder, G. P., Babul, A., & Balogh, M. L., 2003, ApJ, 591, 526

[75]Mohr, J.J., Reese, E.D., Ellingson, E., Lewis, A.D., & Evrard, A.D. 2000, ApJ, 544, 109

[76]Myers S. T., Baker, J. E., Readhead, A. C. S., Leitch E. M., Herbig, T. 1997, ApJ, 485, 1

[77]Navarro, J.F., Frenk, C.S., & White, S.D.M., 1995, MNRAS, 274, 720

[78]Nozawa, S., Itoh, N., & Kohyama, Y., 1998, ApJ, 508, 17

[79]Courteau, S., Willick, J. A., Strauss, M. A., Schlegel, D., & Postman, M. 2000, ASP Conf. Ser. 201: Cosmic Flows Workshop, 17

[80]Peel, A., & Knox, L. 2002, preprint, (astroph/0205438)

[81]Penzias, A.A., & Wilson, R.W. 1965, ApJ, 142, 419

[82]Peterson, J.R., Paerels, F.B.S., Kaastra, J.S., Arnaud, M., Reiprich, T.H., Fabian, A.C., Mushotzky, R.F., Jernigan, J.G., & Sakelliou, I., A&A 365, L104

[83]Pointecouteau, E., Giard, M., & Barret, D. 1998, A&A, 336, 44

[84]Pointecouteau, E., Giard, M., Benoit, A., Désert, F.X., Aghanim, N., Coron, N., Lamarre, J. M., & Delabrouille, J. 1999, ApJ, 519, L115

[85]Pointecouteau, E., Giard, M., Benoit, A., Désert, F.X., Bernard, J.P., Coron, N., & Lamarre, J. M. 2001, ApJ, 552, 42

[86]Press, W.H., Teukolsky, S.A., Vetterling, W.T., & Flannery, B.P., 1992, Numerical Recipes in C (New York: Cambridge Univ. Press)

[87]Reese, E.D., Mohr, J.J., Carlstrom, J.E., Joy, M., Grego, L., Holder, G.P., Holzapfel, W.L., Hughes, J.P., Patel, S.K., & Donahue, M., 2000, ApJ, 533, 38

[88]Reese, E. D., Carlstrom, J. E., Joy, M., Mohr, J. J., Grego, L., & Holzapfel, W. L. 2002, ApJ, 581, 53

[89]Reese, E. D., 2003, private communication

[90]Rephaeli Y. 1980, ApJ, 241, 858

[91]Rephaeli, Y. 1995, ApJ, 445, 33

[92]Richards, P.L. 1994, *Journal of Applied Physics*, 76, 1

[93]Runyan, M.C. 2002, PhD Thesis, California Institute of Technology

[94]Schindler, S., Hattori, M., Neumann, D.M., & Boehringer, H., 1997, A&A, 299, L9

[95]Schulz, A.E., & White, M., 2003, ApJ, 586, 723S

[96]Sheth, R.K, & Diaferio, A. 2001, MNRAS, 322, 901

[97]Shimon, M. & Rephaeli, Y. 2002, ApJ, 575, 12

[98]Smail, I., Ivision, R.J., Blain, A.W., & Kneib, J.P., 2002, MNRAS, 331, 495

[99]Staggs, S., & Church, S. 2001, Proc. of the APS/DPF/DPB Summer Study on the Future of Particle Physics (Snowmass 2001) ed. N. Graf, (astro-ph/0111576)

[100]Strauss, M.A., & Willick, J.A., 1995, Physics Reports, 261, 271

[101]Suhhonenko, I., & Gramann, M. 2003, MNRAS, 339, 271

[102]Sunyaev, R.A., & Zel'dovich, Ya. B. 1972, Comments Astrophys. Space Phys., 4, 173

[103]Sunyeav, R.A., & Zel'dovich, Ya. B. 1980, MNRAS, 190, 413

[104]Verde, L., Haiman, Z., & Spergel, D.N. 2002, ApJ, 581, 5

[105]Vikhlinin, A., VanSpeybroeck, L., Markevitch, M., Forman, W.R., & Grego, L. 2002, ApJ, 578, L107

[106]Voevodkin, A.A., Vikhlinin, A.A., & Pavlinsky, M.N., *Astronomy Letters*, 28, 366

[107]Wagoner, R.V., Fowler, W.A., & Hoyle, F. 1967, ApJ, 148, 2

[108]Wang, L., & Steinhardt, P.J. 1998, ApJ, 508, 483

[109]Willick, J. A. 1999, ApJ, 522, 647